Modeling the Release of River Ice Jams and their Impact on River Bed Scouring

by

Michail Manolidis

A dissertation submitted in partial fulfillment
of the requirements for the degree of
Doctor of Philosophy
(Mechanical Engineering)
in The University of Michigan
2013

Doctoral Committee:

Professor Nikolaos Katopodes, Co-Chair
Professor William Schultz, Co-Chair
Assistant Professor Krzysztof Fidkowski
Professor Nickolas Vlahopoulos
Associate Professor Nikos Chronis

TABLE OF CONTENTS

LIST OF FIGURES

Figure

ABSTRACT

Modeling the Release of River Ice Jams and their Impact on River Bed Scouring

by

Michail Manolidis

Co-Chairs: Nikolaos Katopodes and William Schultz

The release of ice jams in rivers is a violent event accompanied by high flow velocities and elevated water levels. It can cause loss of or damage to property, disruption of water ways, and even loss of human life. Furthermore, increased water flow during the release of an ice jam can cause river bed scouring, changes in bed morphology and an increase in river depth. In the case of the Huron Erie Corridor, ice jam releases in the St. Clair River may have a much more severe impact; the St. Clair River drains Lakes Huron and Michigan, so changes in the conveyance of the river affects water levels in those two lakes. Measurements show that the depth of the St. Clair River increased during the 1980s and 90s, and this increase in depth may have been responsible for an increase in river conveyance and a drop in the water levels of Lakes Huron and Michigan. Such an increase in the depth of the St. Clair River may have been caused by the release of ice jams. Considering the strategic importance of Lakes Huron and Michigan, as one of the greatest freshwater reservoirs on Earth, as well as their economic significance in commerce, tourism and commercial fishing, much attention is needed on factors that may affect the integrity of these valuable

assets. Until now it has not been shown that the release of an ice jam can cause scouring in the St. Clair River.

In this work a movable bed model is developed and coupled to a hydrodynamic model. The hydrodynamic model is a fully 3D non-hydrostatic Reynolds-averaged Navier-Stokes equation solver, that employs the finite volume method. The movable bed model employs geometric modeling of the river bed, whose proper morphology is not given by the hydrodynamic model, as the latter employs stair-stepping to model the bed morphology. The geometric model is combined with a methodology to calculate the bedload fluxes when scouring occurs. A Shields criterion is employed to determine whether sediment is mobilized or not. Once the fluxes are found the Exner (bed evolution) equation is solved numerically using the finite volume approach in order to update the bed elevation. A sandslide simulation algorithm is also developed as part of the movable bed model. The model developed allows for variation in the river bed roughness, and information on the sediment grain size distribution obtained from field observations is used.

The other part of the work involves modeling an initially still ice jam that is released. The shape and size of the ice jam is adjusted to match morphologic characteristics as well as flow conditions during the massive 1984 ice jam. Boundary conditions are also set to match those of the 1984 ice jam event. Flow simulations were run for normal flow (open water) conditions as well as for when an ice jam is present. It is found that under normal flow conditions there are three regions in the St. Clair River where stresses on the bed are elevated. From simulations with an ice jam present, it is found that during and following the release, the stresses in those three locations rise above critical values and scouring occurs. When the jam is still, however, it is found that the stresses on the bed under the jam are for the most part lower than under normal flow conditions, and, as such, scouring cannot happen under the jam when it is immobile. The movable bed model is employed in the ice

jam release simulations, and significant changes in depth in three regions of the river are produced. Based on the simulation results, the model predicts that in the event of an ice jam like the one in 1984 significant scouring will occur at certain locations of the St. Clair River. Finally, a scenario was tested where the water level difference between Lakes Huron and St. Clair is even greater than during the 1984 ice jam. The resulting scouring in that case is even more pronounced.

CHAPTER I

Introduction

The Great Lakes account for 20% of the Earth's surface freshwater supply, and for 90% of North America's surface freshwater supply. These figures indicate the importance of these lakes as a freshwater reservoir that is readily available. Furthermore, the Great Lakes have great importance as an ecosystem. With respect to human activities, they are a source of food (fish), they encompass commercial routes for industry, they offer tourist attractions, and entire communities and recreational facilities are built around the Great Lakes.

A general map of the Great Lakes System can be seen in Figure 1.1.

Between 1963 and 2006, there has been a lake-to-lake head fall between Lakes Michigan-Huron and Lake Erie of approximately 23 cm, as can be seen in Figure 1.2.

A drop of the water level in the Great Lakes, in addition to translating to a loss of colossal amounts of freshwater, can affect and change the shoreline and the communities that have been built around the Lakes. It may affect the entire ecosystem, and can also cause disruptions to human activities, such as creating impediments for the passing of ships.

A comprehensive report to the joint commission between the US and Canada [1] was prepared in 2009, consisting of a number of discrete studies, that addressed the key scientific issues related to the head fall between the two lakes.

Figure 1.1: Map of the Great Lakes System [1]

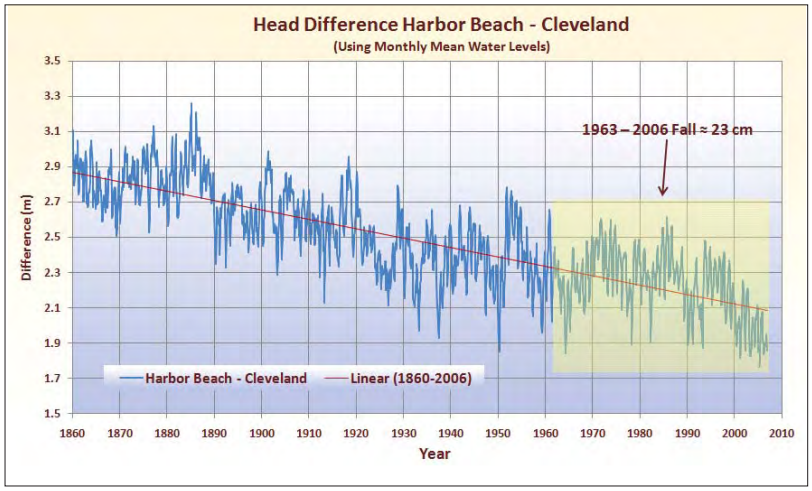

Figure 1.2: The Head Difference (Lake-to-Lake Fall) between Lake Michigan-Huron and Lake Erie [1]

The studies, included in the report, examined a) the change in conveyance of the St. Clair River, due to bed erosion, b) effects of Glacial Isostastic Adjustment (GIA), and c) hydroclimatic factors. The studies showed that, of the three different mechanisms, hydroclimatic factors have played a dominant role, and, in particular,

there seems to be a decrease in Net Total Supplies (NTS) to Lakes Michigan and Huron, that affects the water level of those lakes. Net Total Supplies is the inflow of water in the two lakes from tributaries, melting ice, precipitation, as well as runoff water. GIA has had the least effect on the head fall. Of particular interest in this study is the effect of change in river conveyance due to bed erosion. Change in conveyance of the St. Clair River has had a significant effect, especially between 1985 and 1989. In fact, the change in conveyance during that period alone accounts for an 8 to 10 cm drop in head difference, and this change has been of an episodic nature. It is worth noting that a 10 cm water level drop in Lakes Michigan-Huron accounts for the loss of approximately 1.2 billion cubic meters of water. This compares to the annual total water consumption for New York City and its surroundings (1.7 billion m^3), or to the annual household water consumption of Greece.

There are three mechanisms that could have caused a change in conveyance in St. Clair River. The first, which is the topic of this thesis, is scouring caused by an ice jam. There is speculation, however, that dredging and mining could have had an impact [1]. The last dredging project in St. Clair River took place in 1962 and water levels in Lakes Huron-Michigan have been dropping ever since. There are two mechanisms by which dredging and mining could affect river conveyance. By removing material the river might get deeper at certain locations. The second mechanism involves exposing sediment of a different composition, effectively changing the bed roughness. Sensitivity analysis has shown that the flow rate through St. Clair River is very sensitive to changes in bed roughness and the change in resistance to flow that it brings about [79]. Unfortunately, there is a lack of adequate information on the bathymetry of St. Clair River before the last dredging project, as well as on the bed sediment composition at the time. Furthermore, studies indicate that the increase in river conveyance happened sometime in the mid 1980's.

Another mechanism by which scouring can occur is by the stresses induced on the

bed by propellers of ships [1]. It has been calculated that the stresses can reach levels capable of moving gravel 60 mm in diameter, a size that is at the uppermost levels of the median grain size distribution in St. Clair River. Again, it is very difficult to impossible to assess the effect that the passage of ships may have had on bed morphology over time, since information is lacking.

Bathymetric studies indicate that the bed of the St. Clair River was higher in 1971 than it was in 2007, along the river's entire length. More recent measurements show that there has been no bed erosion since 2000. There are questions about the accuracy of the bathymetric data that date back to the 1970s and 80s. What is, however, certain, is that the river's conveyance increased during the 1980s; with respect to this, four hydrodynamic models were used for the joint commission report, and all indicated an increase in conveyance. Namely, models that were used were the HEC-RAS, the RMA-2, the HydroSed2D, and the TELEMAC-2D. These models will be described in subsequent chapters. All the models indicated that there was an increase in the St. Clair River conveyance in the mid 80s period. From the HydroSed2D model, it was estimated that, under normal flow conditions, the stresses at the bottom of the St. Clair River would not suffice to induce any bed erosion, considering the bed composition (grain size). However, it is speculated that during episodic events as in ice jam releases, high flow velocities may induce bed scour. In fact, successive seasonal ice jam releases may have had a cumulative effect in terms of lowering the bottom of the St. Clair River.

The release of a river ice jam is, in general, a violent event, followed by high flow velocities and increased water levels. It poses a threat to human life, property, as well as the ecosystem. There are numerous historical accounts of such violent events. We note the 1984 record jam in the St. Clair River [2], that lasted 24 days and whose release may have had an effect on river bed erosion and conveyance.

The primary goal of this thesis is to elucidate **whether the presence and re-**

lease of an ice jam, like the one in 1984, can lead to bed scouring in the St. Clair River. The methodology/model that is used is applicable to any river system, in terms of reproducing the dynamics and results of an ice jam release.

1.0.1 On Ice Jam Formations

Ice formation and breakup in rivers has been an active area of research for many decades, up to this day. The breakup of ice jams is of particular interest and importance, since the ensuing surges or flood waves can be destructive to life and property, and can alter hydrological systems and water reservoirs in adverse ways.

Ice formation in river channels occurs in seasonally cold regions. These regions are characterized by average daily temperatures of below 0 degrees Celsius for at least a month during winter. Ettema and Kempera [4] studied and described the processes that lead to ice formation. There are four types of ice that form in a river when temperatures are sufficiently low. The most visible type is border ice that forms at the banks. The second type, frazil, comprises of millimeter-sized ice disks that grow while suspended in turbulent supercooled water. The third type is anchor ice, that is attached to the river bed. Anchor ice forms as supercooled and less buoyant water is drawn to the bottom by turbulent mixing. Thus, anchor ice is formed in situ on the river bed. Released anchor ice and frazil accrue on the surface, due to the higher buoyancy of ice, and form drifting slush. This slush, exposed to frigid air, freezes into ice masses, also known as pancake ice, which is the fourth type of ice. Figure 1.3 illustrates the process of ice formation.

Ice floes are the product of slush that freezes or may be the product of ice cover fragmentation during the warmer season. When ice floes encounter an ice cover, their passage is blocked and they accumulate to form a jam. Other factors which may lead to the congestion and arrest of ice floes are natural constriction in the channel, constrictions due to ice at the banks, as well as strong winds blowing upstream.

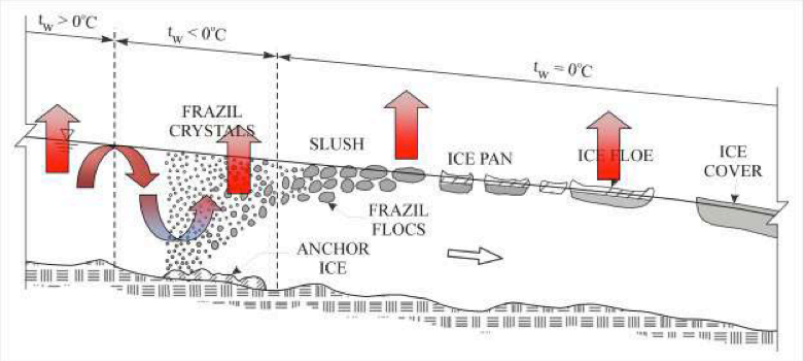

Figure 1.3: Illustration of ice formation [4]

Jams occur, either during the cold season from complete freeze-up of the river surface (freeze-up jams), or during the warm season, as floating ice bodies accrue and form a jam (break-up jams). Breakup jams are generally more severe, because they occur during periods of higher flows, during the melting of ice and increased precipitation. Typically, the level of the water upstream is higher than the level downstream. Our focus will be on breakup jams, since they lead to extreme phenomena, which will be the area of concentration in this thesis.

Concerning the morphology/type of ice jams, the key factor is whether the ice bodies submerge under when they encounter the ice cover. If they do not, the jam will be a surface jam. Flow separation, however, under the ice body, generates a downward force on the floating body, as can be seen in Figure 1.4. If the ice floe submerges, three scenarios are possible:

After the ice bodies submerge, they deposit under the ice cover, until the flow through the constriction is high enough that no more masses are deposited in the constriction. Such a jam is called a thickened jam. Submerged ice bodies are carried a distance under the ice cover and are eventually deposited at different locations where the flow rate is low enough. Continuous deposition in a location causes so called hanging dams. Finally, if the floes are large enough, they lodge between the bed and the cover and form grounded jams. Jams that form by the submergence of

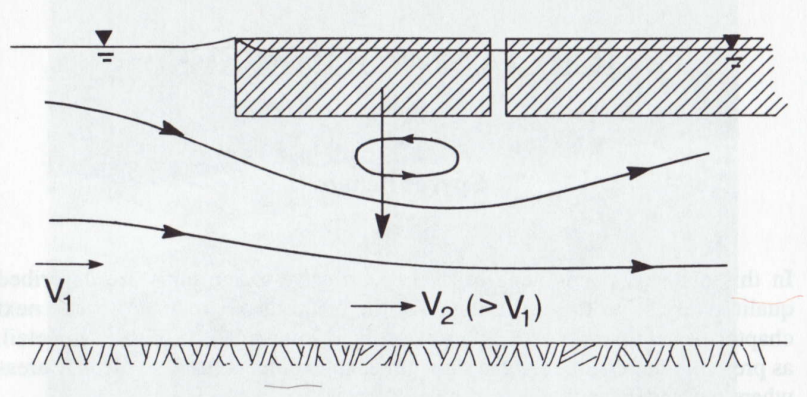

Figure 1.4: Flow separation under the head of the jam causes incoming ice floes to submerge [3]

ice floes under an ice cover form especially during freeze-up, but there are cases where their formation takes place during the warmer seasons, as a result of breakup.

The 1984 ice jam in the St. Clair River was a break-up jam. It took place during the warmer month of April and the ice that made up the jam originated from ice bodies that had broken off from an ice sheet in Lake Huron near the entrance of the river. The ice bodies were carried downstream until a cold spell fused them into a jam, initially near Algonac and gradually expanding upstream as more ice bodies got trapped. In its final days the ice jam almost reached the town of St. Clair upstream. Judging from the dramatic effect that the jam had on reducing the river flow rate, it is most probable that the 1984 ice jam was a thickened jam.

Morphologically, a thickened jam is characterized by a thinner head upstream, which progresses gradually, and a thicker toe downstream, as can be seen in Figure 1.5. In the region of the toe, flow is constricted more than elsewhere and is characterized by higher velocities. This can lead to scouring of the river bed under the toe. As the head progresses upstream, the water level and storage increases, and so does the upstream-downstream difference in water levels.

It is worth mentioning here that there is a relationship between river slope and thalweg sinuosity (sinuosity of the river) [7]. Because ice jams deepen and slow

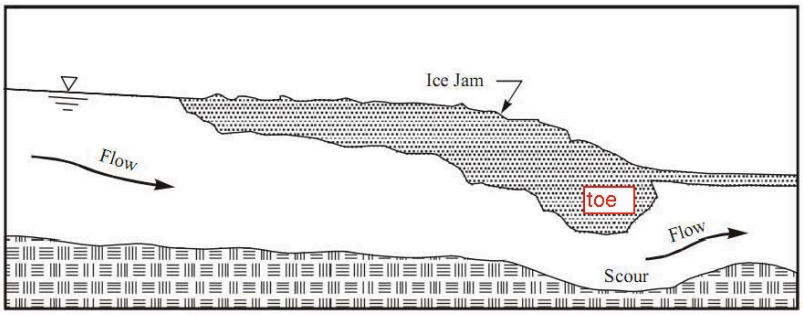

Figure 1.5: Thickened jam [4]

down the flow upstream, the river responds as if the slope were smaller, and channel alignment may be affected. Furthermore, due to changes in the channel cross section, flow may be ducted through subchannels formed under a non-uniform jam, and this may lead to channel avulsion and thalweg shifts. Finally, if water levels rise enough, overbank flow may create new channels and old channels may be eventually cutoff, as can be seen with the river in Figure 1.6.

Figure 1.6: Overbank flow in a river [4]

Ice jams are held in place by an intact downstream ice cover. Release occurs when this cover weakens and breaks. The weakening of the ice cover is the result of both thermal and mechanical processes. If warmer water flows under the ice jam it can make it thinner and weaken it. The other mechanism by which the ice cover weakens and breaks is mechanical. Ice blocks can be entrained in turbulent flow deep under the jam, and once after the jam will accelerate upwards until they hit the ice cover. The impact may cause the cover to break. Another mechanism by which the cover may fail is by increased flow conditions, due to melting ice and/or precipitation, which pushes the jam downstream, and its toe upwards under the cover, which may cause the cover to fail. Once the cover starts failing two things might happen. The moving jam may create a front of breaking ice cover, or the cover may crack in its center and along its length. In either case, a strong surge follows, not unlike the breaking of a dam. The surge is characterized by high flow velocities and rising water levels that can be felt a long distance downstream.

1.1 Contributions

To approach the problem of determining whether an ice jam could lead to scouring of the river bed in St. Clair River there are three distinct parts that have to be put together into one composite model. A hydrodynamic model is first employed. The model is a 3D non-hydrostatic RANS equations solver and is the first fully 3D non-hydrostatic model to be employed in St. Clair River. It is also the first non-hydrostatic model to be used to simulate the release of an ice jam. The non-hydrostatic aspect is important because the release of an ice jam entails high fluid accelerations, during which the hydrostatic assumption breaks down. The release of an ice jam is modeled by modifying the hydrodynamic model. The 3D aspect is important in its own right; complex flow patterns like flows in the transverse direction in river bends cannot be captured by two-dimensional models based on the shallow

water equations.

A bedload transport model capable of simulating bed scouring is developed in this work and is coupled to the hydrodynamic model. The model uses two original methodologies that are developed for modeling the bed geometry of the river, either of which gives promising results. It is also capable of using two different methodologies for calculating the motion of sediment along the bed.

The third part needed to simulated the release of an ice jam and any ensuing bed scouring in St. Clair River is constructing the geometric domain on a computational level. Bathymetric data obtained from the Great Lakes division of the National Oceanic and Atmospheric Administration are used to construct a grid of the river. Information on the sediment grain size distribution along the river was obtained from the same source and is used both in the hydrodynamic and the bedload transport models.

Simulations are run for flow in the St. Clair River under normal flow conditions, during an ice jam like the one in 1984 while it is not moving and also during and following the release of the ice jam. The results show that there are three regions in the river that experience elevated bed stresses under normal flow conditions, which have not appeared in any of the models that have been implemented before. During and after the release of the jam the stresses in those regions increase to above-critical values and scouring takes place. While much of the scouring occurs during the initial surge following the release, scouring continues thereafter because high flow velocities persist, fueled by the increased water level difference between Lakes Huron and St. Clair. The increased water level difference is the result of diminished supply to Lake St. Clair because of the flow constriction that the ice jam causes. A test case scenario is simulated in which the water level difference between the two lakes is even greater, which could happen in the case of a jam like the one in 1984, but which stays in place for a longer period of time before it is released. The results of the simulation

indicate considerably more pronounced scouring in that case. Finally, it is found that scouring will not happen under a jam that is not moving, because the stresses under the jam are in fact lower than those under normal flow conditions.

CHAPTER II

An Overview of Past Work

2.1 Previous Studies of Ice Jams and their Release

2.1.1 A Study of Scouring Under a Stationary Jam

Mercer and Cooper [13] first studied scouring under an ice jam in 1977. Figure 2.1 shows the schematic of the jam model.

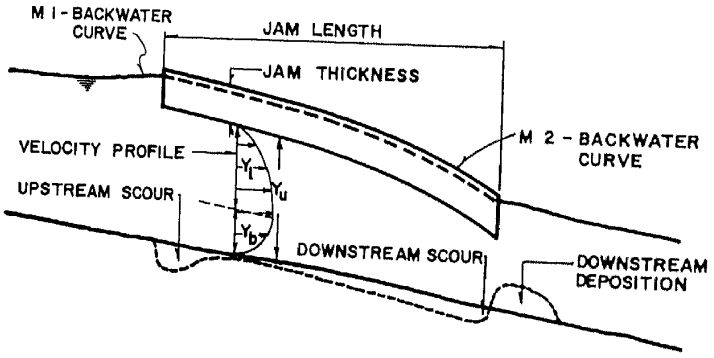

Figure 2.1: Schematic of model [13]

In steady open channel flow the mean flow velocity is given by the Chezy formula:

$$V = C\sqrt{yS}\ , \tag{2.1}$$

where V is the mean velocity, y is the depth (hydraulic radius in 1D flow) and S

is the slope of the bed. C is the Chezy coefficient with units $m^{\frac{1}{2}}/s$. The following formula relates the Chezy coefficient with Manning's roughness coefficient, n [11]:

$$C = \frac{1.486}{n} y^{\frac{1}{6}} \ , \tag{2.2}$$

where n is the Manning coefficient with units $s/m^{\frac{1}{3}}$. The shear stress, τ_o, on the boundary is given by:

$$\tau_o = \rho g y S \ , \tag{2.3}$$

where ρ is the fluid density. For ice covered water and referring to figure 2.1, the depth of flow was divided into two components, y_i for the upper, ice, part and y_b for the bottom, bed, part, with respective friction coefficients, n_i and n_b. The following formula deduced by Michel [15] was used for deriving Manning's n_u that includes friction with the bed and the underside of the jam:

$$n_u^{1.5} = n_i^{1.5} + n_b^{1.5} \ , \tag{2.4}$$

from which the depths y_i and y_b were calculated as:

$$\frac{y_i}{y_u} = (\frac{n_i}{n_u})^{1.5} \tag{2.5}$$

and

$$\frac{y_b}{y_u} = (\frac{n_b}{n_u})^{1.5} \ . \tag{2.6}$$

Having calculated the depths y_i and y_b and using formula (2.3), it was possible to find the flow-induced stress on the bed and on the ice. The authors used a criterion that determined whether the jam thickened or lengthened (depending on whether the incoming ice floes submerged), which was simply the Froude number. It was considered appropriate to use Fr = 0.08 as a critical value, higher values of which lead to thickening of the jam. The Shields criterion was used to determine ice deposition under the jam, for ice floes carried by the flow under the jam, given by:

$$\frac{\tau_i}{(\rho - \rho_i)gk_i} = 0.046 \ , \tag{2.7}$$

where τ_i is the shear on the ice, ρ_i is the ice density and k_i is the dimension of the ice blocks. If the value of 0.046 was exceeded, then the submerged ice floes would not be deposited under the jam but would be carried further downstream. The mean critical velocity associated with the critical shear stress was given by:

$$V_c = 0.046 g^{\frac{1}{2}} y_i^{\frac{1}{6}} k_i^{\frac{1}{3}} \ . \tag{2.8}$$

The authors presented a criterion that determined whether the jam would fail or not. Based on the conditions upstream, the stability of the jam depended on the value of a parameter X, given by:

$$X = \frac{BV_u^2}{gC^2y_u^2} \ , \tag{2.9}$$

where B is the river width, V_u is the upstream velocity, y_u is the upstream depth and C is the Chezy coefficient. The maximum value of X, for which the jam was stable, was set to 0.0028, as given by Pariset [14]. For scour analysis, the continuity equation for sediment transport is:

$$\frac{\partial q_s}{\partial x} + \frac{\partial(\frac{q_s}{V_s})}{\partial t} + \frac{\partial z_b}{\partial t} = 0 \ , \tag{2.10}$$

where q_s is the volumetric rate of sediment discharge per unit width, V_s is the velocity of sediment movement, z_b is the bed elevation, x is the distance along the river and t is time. The first term in equation (2.10) can be large and is the rate of change of sediment transport along the channel. The second term is, generally, small and is the rate of change with time in the amount of sediment carried with the flow. The third term is the time rate of scour/deposition. The authors used the Colby relationship [16] for fine sand beds, that relates the rate of sediment discharge with the average flow velocity:

$$q_s = A(V - V_c)^B \ , \tag{2.11}$$

where q_s is the sediment volumetric flow rate per unit width, A is a coefficient and B is an exponent. V_c is a critical velocity above which there is sediment movement. In their numerical analysis the authors simulated the evolution of an ice jam and the scouring/deposition underneath. The initial conditions set were those of a jam of

arbitrary length but stable thickness, placed in a river of constant slope. The upper surface of the ice was set in such a way as to obtain a surface profile consistent with the backwater relationship. The model advanced in time with a time step equal to a few hours, adjusting the bed and water surface profiles, the ice jam length and thickness. The process was repeated until it was determined that either the jam had failed, or there was no more thickening taking place and scouring had ceased. Figure 2.2 qualitatively shows the evolution of the jam.

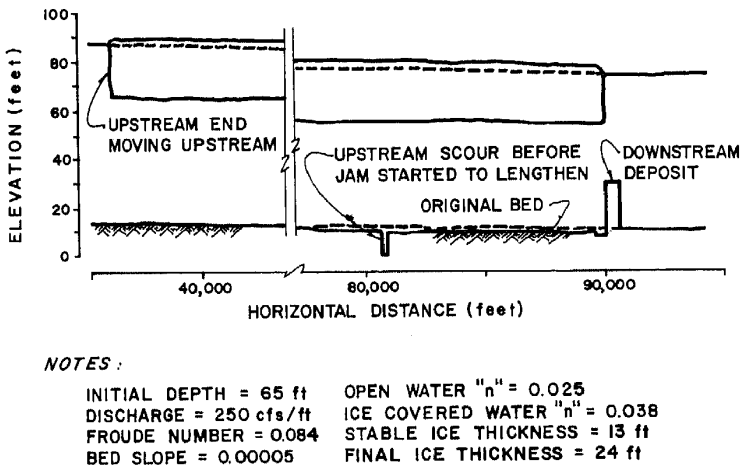

Figure 2.2: Evolution of a jam and river bed scour [13]

The model showed (at least for the case of a stable jam) that maximum scouring would occur at the entrance of the thickening part of the jam, where velocities become high, and that there is deposition at the exit region, downstream, where the flow slows down. Scouring ceased once thickening stopped and a maximum depth was attained. By running many simulations, the authors performed a sensitivity analysis. The Froude number played a critical role, since it determined whether the jam thickened leading to further scouring, or not. The rate of ice delivery was not a significant factor and only affected the duration for thickening and maximum scouring to occur. Factors affecting the strength of the jam were important, since, the longer a jam remained stable, the more scouring could occur. Namely, the angle of internal friction which

determined the internal strength of the jam, was a very important parameter and could only vary within narrow limits. The authors did not study the effects of ice block dimensions.

As will be seen in the work presented in this thesis the premise that scouring could happen under a stationary jam in St. Clair River is invalidated, and it will be shown that stresses on the bed under the jam are in fact lower than those under normal flow conditions. This is an important finding, since it is still speculated that scouring in St. Clair River could have happened while the jam was stationary. A clear weakness of the model by Mercer et al [13] was the use of open channel flow theory that assumes hydrostatic pressure distribution. The assumption does not hold for flow under jams, since the constriction to flow is accompanied by non-negligible flow accelerations. Furthermore, for the case of St. Clair River, the stage elevation upstream did not increase indefinitely, something that would eventually force high flow velocities under the jam and potential scouring, but instead was limited by the stage elevation of Lake Huron as an upper limit.

2.1.2 Studies on Ice Jam Release

Henderson and Geraud [8] carried out one of the first theoretical studies in the breakup of ice jams and surge formation. Their work was based on the dam break problem and used the 1D shallow water equations. Friction with the bed and bed slope were not taken into account in the study, and it was assumed that the water depth was small compared to a typical wavelength.

Figure 2.3 shows the initial steady-state in the location of the jam, as well as the variables involved. Continuity was expressed as:

$$\frac{\partial q}{\partial x} + \frac{\partial y}{\partial t} = 0 \ , \tag{2.12}$$

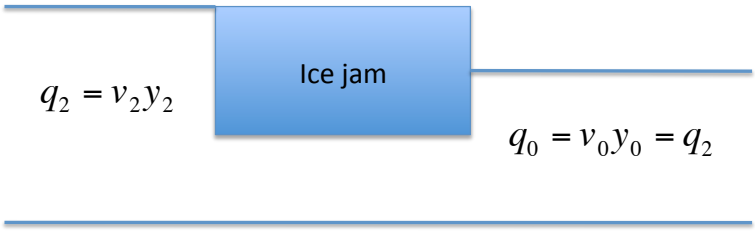

Figure 2.3: Original steady-state in location of the jam

where q is the volumetric flow rate. Conservation of momentum yielded:

$$g\frac{\partial y}{\partial x} + v\frac{\partial v}{\partial x} + \frac{\partial v}{\partial t} = 0 \ , \tag{2.13}$$

where, to avoid any confusion, v is the horizontal velocity. y is the flow depth and g is the acceleration of gravity. Combining equations (2.12) and (2.13) gave:

$$\frac{\partial v}{\partial t} = g(Fr^2 - 1)\frac{\partial y}{\partial x} + \frac{u}{y}\frac{\partial y}{\partial t} \ , \tag{2.14}$$

where Fr is the Froude number. In the first few seconds after the break, velocities increased substantially without notable increase in free surface height. Taking the second time derivative in equation (2.12) and expanding the partial derivatives gave:

$$\frac{\partial^2 y}{\partial t^2} = g(1 - Fr^2)\left(\frac{\partial y}{\partial x}\right)^2 + y\frac{\partial^2 y}{\partial x^2} \tag{2.15}$$

and assuming constant slope for the free surface gave:

$$\frac{\partial^2 y}{\partial x^2} = 0 \ . \tag{2.16}$$

The term $\frac{\partial y}{\partial x}$ is very small, so it was concluded that $\frac{\partial y}{\partial t}$ was actually very small initially. This analysis implied that flow velocities got high very quickly with no initial notable changes in free surface height.

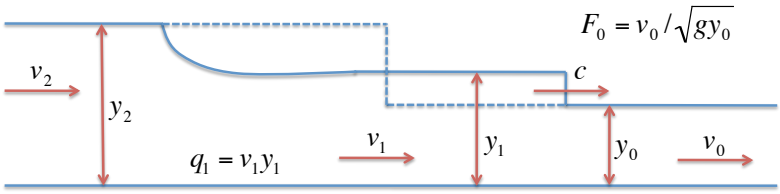

Figure 2.4: Dam break situation

The dam break situation is depicted in Figure 2.4, where relevant parameters are annotated. Following Henderson's analysis [8] gave:

$$v_2 + 2\sqrt{gy_2} = v_1 + 2\sqrt{gy_1} \ , \tag{2.17}$$

where v_2 and y_2 are the upstream flow velocity and depth, respectively, and v_1 and y_1 are the surge wave flow velocity and depth, respectively. Continuity and conservation of momentum yielded:

$$c(y_1 - y_0) = v_1 y_1 - v_0 y_0 \tag{2.18}$$

and

$$\frac{(c - v_0)^2}{gy_0} = \frac{1}{2}\frac{y_1}{y_0}\left(\frac{y_1}{y_0} + 1\right) \ , \tag{2.19}$$

where c is the surge wave velocity, v_o and y_o are the original downstream flow velocity and depth, respectively. With the three equations, 2.17, 2.18 and 2.19, the

three parameters of the surge wave, the flow velocity, v_1, the flow depth, y_1 and the surge wave speed, c, could be determined. The analysis showed that the surge wave height, $y_1 - y_0$, was never greater than half of the original drop ,$\frac{1}{2}(y_2 - y_0)$, across the jam. The analysis then set an upper limit in the increase in stage elevation during a dam break.

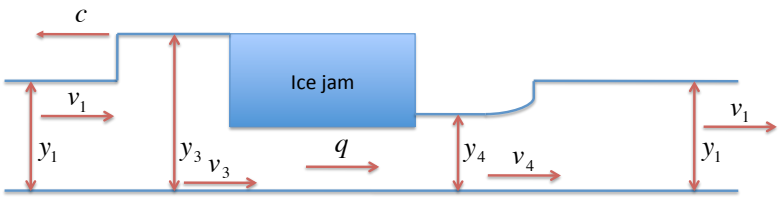

Figure 2.5: Dam break situation with a reformed ice jam

Figure 2.5 shows the scenario where the dam reforms further downstream, with relevant parameters. This was plausible, since the ice blocks from the break of the initial jam can get congested further downstream. Continuity and conservation of momentum yielded respectively:

$$c(y_3 - y_1) = v_1 y_1 - q \tag{2.20}$$

and

$$(c + v_1)^2 = \frac{1}{2}\frac{y_3}{y_1}\left(\frac{y_3}{y_1} + 1\right) \ , \tag{2.21}$$

where, referring to figure 2.5, q is the volumetric flow rate under the jam, c is the upstream-traveling wave velocity and v_1 and y_1 are the upstream flow velocity and depth, respectively, and y_3 and v_3 are the new flow depth and velocity above the new jam. The negative wave downstream of the jam was described by:

$$v_4 - 2\sqrt{gy_4} = v_1 - 2\sqrt{gy_1} \ , \tag{2.22}$$

where v_4 and y_4 is the new flow velocity and depth below the jam. Applying continuity and conservation of momentum between sections 4 and 1 (figure 2.5) and using the relationship between sections 3 and 1:

$$v_3 + 2\sqrt{gy_3} = v_1 + 2\sqrt{gy_1} \ , \tag{2.23}$$

allows to solve for the unknowns c, q, y_3 and y_4. It turned out that in the particular case, the rise in water level $y_3 - y_0$ could have been as much as six times the original height difference $y_2 - y_0$. The important point was that failure of the second jam downstream could produce a more powerful surge than in the release of the original jam.

The authors compared theory to field observations, namely those of the 1979 spring break-up on the Athabasca River at Fort McMurray, Alberta [12]. A surge 3.6 meters in height arrived after 45 minutes, traveling from 11km upstream, the location of the jam. The theory predicted a surge height of 4.16 meters. However, their prediction of a surge speed of 11m/s was off, since the observed real speed was closer to 4 m/s. It should be noted that the authors did not include the effects of frictional resistance in their study.

In 1982, Beltaos and Krishnappan [9] conducted a more detailed analytical and numerical study of ice jam release surges. They compared their results with accounts of a 1979 jam release in the Athabasca River at Fort McMurray [12]. Their approach was to study the unsteady one-dimensional ice and water flow. Figure 2.6 depicts the situation of ice moving over water during a jam release.

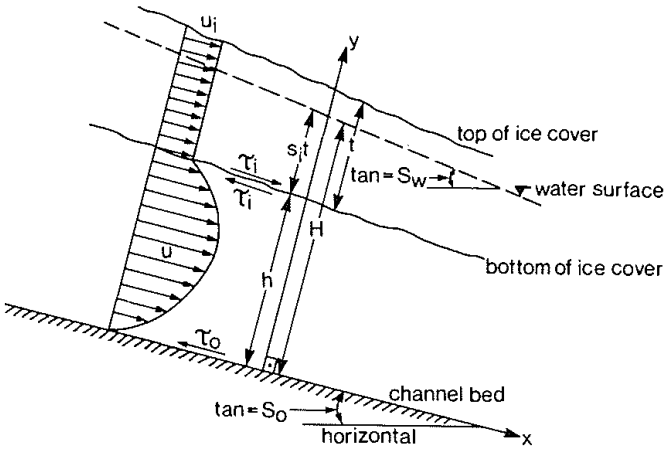

Figure 2.6: Definitions sketch [9]

Assuming a constant porosity of ice, e, continuity applied to the ice yielded:

$$(1-e)\frac{\partial T}{\partial t} + \frac{\partial q_i}{\partial x} = 0 \ , \tag{2.24}$$

where T is the ice cover thickness, x is the longitudinal distance and q_i is ice discharge per unit width, given by:

$$q_i = (1-e)u_i T \ , \tag{2.25}$$

where u_i is the ice velocity.

(2.24) was substituted into (2.25) giving:

$$\frac{\partial T}{\partial t} + \frac{\partial u_i T}{\partial x} = 0 \ . \tag{2.26}$$

Continuity for water yielded:

$$\frac{\partial h}{\partial t} + es_i \frac{\partial T}{\partial t} + \frac{\partial q_w}{\partial x} = 0 \ , \tag{2.27}$$

where h is the height of the water column, s_i is the specific gravity of ice and q_w is the water discharge per unit width, given by:

$$q_w = q' + eu_i s_i T \ . \tag{2.28}$$

The second term on the right in equation (2.28) accounted for the water entrained in the ice and the first term, q', is the discharge from under the ice, given by:

$$q' = \int_0^h u \, \mathrm{d}y = Vh \ , \tag{2.29}$$

where V is the average flow velocity under the ice.

Combining equations (2.27), (2.28) and (2.29), gave (2.30):

$$\frac{\partial h}{\partial t} + \frac{\partial q'}{\partial x} = 0 \ , \tag{2.30}$$

which was a continuity equation for the region under the ice. Multiplying equation (2.24) by the density of the ice, ρ_i, multiplying (2.27) by the density of water, ρ_w, and adding the results, yielded an overall mass flux equation:

$$\rho_w \frac{\partial H}{\partial t} + \frac{\partial \rho_w q}{\partial x} = 0 \ , \tag{2.31}$$

where H is the overall water depth, including the water below the ice and the submerged portion of the ice, given by:

$$H = h + s_i T \ , \tag{2.32}$$

and $\rho_w q$ is the total mass flux given by:

$$\rho_w q = \rho_i q_i + \rho_w q_w \ . \tag{2.33}$$

Equation (2.31) is the continuity equation for water flow of depth H and discharge rate q. Conservation of momentum for the water layer gave:

$$\rho_w \left(\frac{\partial u}{\partial t} + u\frac{\partial u}{\partial x} + v\frac{\partial u}{\partial y} \right) = \rho_w g S_0 - \frac{\partial P}{\partial x} + \frac{\partial \tau}{\partial y} \ , \tag{2.34}$$

where u and v are velocity components in the x and y directions respectively, g is the acceleration of gravity and S_0 is the channel bed slope. The pressure, P, was assumed hydrostatic, and τ is the x-direction shear stress. It should be noted that the authors did not start with the shallow water equations in their formulation, but proceeded to depth-average later in the course of their analysis, following the hydrostatic pressure assumption. Continuity in differential form gave:

$$\frac{\partial u}{\partial x} + \frac{\partial v}{\partial y} = 0 \ . \tag{2.35}$$

Multiplying (2.35) by u and adding to (2.34), and then integrating from $y = 0$ to

$y = h$, gave:

$$\rho_w \left(\frac{\partial}{\partial t} \int_0^h u \, \mathrm{d}y + (u)_h \frac{\partial h}{\partial t} + \frac{\partial}{\partial x} \int_0^h u^2 \, \mathrm{d}y (u)_h^2 \frac{dh}{dt} + (u)_h (v)_h \right) = \rho_w g S_o h - \frac{\partial}{\partial x} \int_0^h P \, \mathrm{d}y + (P)_h \frac{\partial h}{\partial x} - (\tau_i + \tau_o) \quad , \tag{2.36}$$

where τ_o is the bed shear stress and τ_i is the shear stress on the underside of the ice cover. It should be noted that $(u)_h = u_i$ and $P = \rho_w g(H - y)$. To determine $(v)_h$ (2.35) was integrated from $y = 0$ to $y = h$ to yield:

$$(v)_h = u_i \frac{\partial h}{\partial x} + \frac{\partial}{\partial x} \int_0^h u \, \mathrm{d}y \ . \tag{2.37}$$

Using (2.29), (2.30), (2.32), (2.34), and (2.37), (2.36) was simplified to:

$$\rho_w \left(\frac{\partial q'}{\partial t} + \frac{\partial m'}{\partial x} \right) = \rho_w g h S_w - (\tau_i + \tau_o) \ , \tag{2.38}$$

where S_w is the slope of the water surface and:

$$m' = \int_0^h u^2 \, \mathrm{d}y \ . \tag{2.39}$$

Considering an elementary ice mass, dm_i, of length dx, then:

$$(dm_i)a_i = g(dm_i)S_w + \tau_i dx \ , \tag{2.40}$$

where a_i is the acceleration of the elementary ice mass, given by:

$$a_i = \frac{du_i}{dt} = \frac{\partial u_i}{\partial t} + u_i \frac{\partial u_i}{\partial x} \ . \tag{2.41}$$

Also:

$$dm_i = \rho_i(1-e)Tdx + \rho_w e S_i T dx = \rho_w S_i T dx \ . \tag{2.42}$$

Substituting Equations (2.41) and (2.42) into (2.40), gave:

$$\rho_w S_i T \left(\frac{\partial u_i}{\partial t} + u_i \frac{\partial u_i}{\partial x} \right) = \rho_w g S_i T S_w + \tau_i \ , \tag{2.43}$$

where S_i is the slope of the ice. Using equations (2.38) and (2.30), and making the approximation $m' \approx V^2 h$, yielded:

$$\rho_w h \left(\frac{\partial V}{\partial t} + V \frac{\partial V}{\partial x} \right) = \rho_w g h S_w - (\tau_i + \tau_0) \ . \tag{2.44}$$

Assuming that the ice quickly accelerated to the flow speed, that is, $u_i \approx V$, and adding (2.43) and (2.44), gave:

$$\rho_w H \left(\frac{\partial V}{\partial t} + V \frac{\partial V}{\partial x} \right) = \rho_w g H S_w - \tau_0 \ , \tag{2.45}$$

which was the same as the conservation of momentum equation for open channel flow of depth H and average velocity V. Furthermore, since q in (2.33) becomes VH, then:

$$\frac{\partial H}{\partial t} + \frac{\partial (VH)}{\partial x} = 0 \ . \tag{2.46}$$

The authors then concluded that for flow containing an ice cover at fully developed speed, the overall equations governing the motion of water and ice were identical to those for water flow of depth H and average flow velocity V. Given proper boundary and initial conditions, these equations could be solved numerically. The authors estimated that it would take a few minutes for the ice cover speed, u_i, to become 95% of the average flow velocity V. The authors applied their model to the Athabasca River event in 1979 [12]. The initial conditions were determined by Doyle and Andress [12] through observations. To solve the equations numerically, the stress on the bed,τ_0, had to be estimated. This was done by taking:

$$\frac{V}{V*} = \frac{C}{\sqrt{g}} \ , \tag{2.47}$$

where $V*$ is the shear velocity, defined as:

$$V*^2 = \frac{\tau_0}{\rho} \ , \tag{2.48}$$

and C is the Chezy resistance coefficient that can be calculated using one of several empirical formulas [11]. The authors determined through trial and error that the best agreement with experimental data was obtained by taking $\frac{V}{V*} = 9$, the ratio varying from 5 for a stationary ice sheet of 1m thickness, to 16 for open water flow. Figure 2.7 shows the computed peak surge in the Athabasca river and Figure 2.8 shows the computed velocity-time variation several kilometers downstream of the location of the ice jam release, at Mac-Ewan bridge. At $T = 35min$, the surface velocity at that location was computed to be $2.2m/s$. Observers estimated the velocity at that time and location to be between 2 and $3m/s$. The agreement was good.

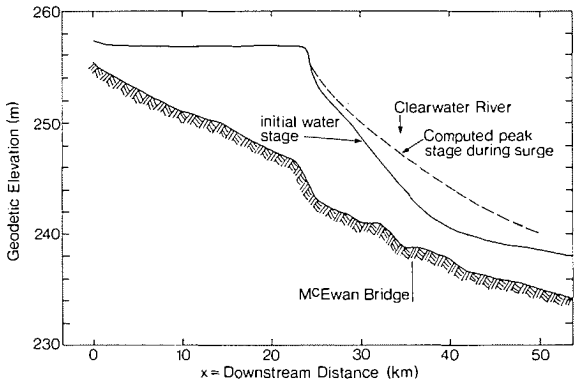

Figure 2.7: Computed downstream variation of peak surge stage [9]

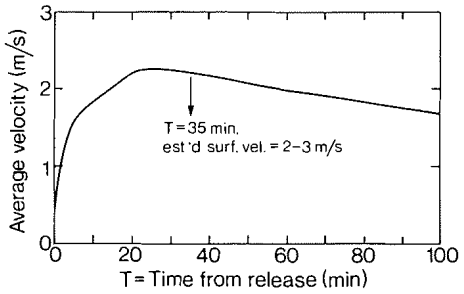

Figure 2.8: Computed velocity - time variation at MacEwan Bridge [9]

The ice jam in the case study was more than 10km long. The authors conducted computational studies for longer jams and estimated equal peak velocities but longer durations of high surface velocities.

Joliffe and Gerard [10] conducted experiments in order to study the effect of the presence of ice on the surge wave characteristics. They also conducted a numerical study of the dam break problem, but accounted for frictional resistance and channel slope, which had not been accounted for by Henderson et al [8] in their study. The experimental setup is shown in Figure 2.9. Artificial ice was used upstream of a sluice gate, in the form of polyethylene pellets. The ice thickness was varied and the ice length was kept inversely proportional to it. The upstream depth was 300mm and the downstream depth was 100mm. The jam release was simulated by the rapid removal of the sluice gate.

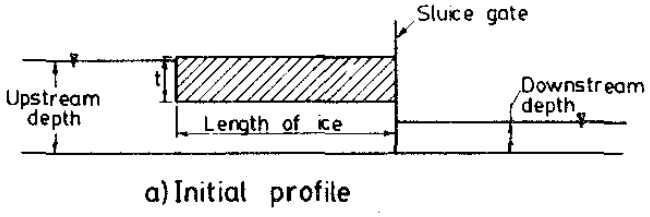

Figure 2.9: Experimental setup [10]

The authors did not find a clear trend in the variation of flow depth with ice depth. They concluded that since there was no clear trend in the experimental results, the presence of ice had little effect on the characteristics of the surge front, the shallow water equations could be used to describe the problem mathematically. Continuity and conservation of momentum (St. Venant Equations) yielded, respectively:

$$\frac{\partial A}{\partial x} + \frac{\partial Q}{\partial x} = 0 \tag{2.49}$$

and

$$\frac{\partial Q}{\partial t} + \frac{\partial}{\partial x}\left(\frac{Q^2}{A}\right) + gA\frac{\partial y}{\partial x} = gA\left(S_0 - S_f\right) \ . \tag{2.50}$$

A is the flow cross-sectional area, g is the acceleration of gravity, Q is volume flow rate, S_0 is the channel slope, S_f is the frictional slope, t stands for time and y is flow depth. By numerically solving equations (2.49) and (2.50) , the authors showed that, according to their model, the surge wave should diminish in amplitude over distance and time, as shown in figure 2.10, the decrease being the direct result of friction. As such, surge wave velocities should be smaller than those computed in simple dam break theory by Henderson et al [8] where friction and slope were neglected.

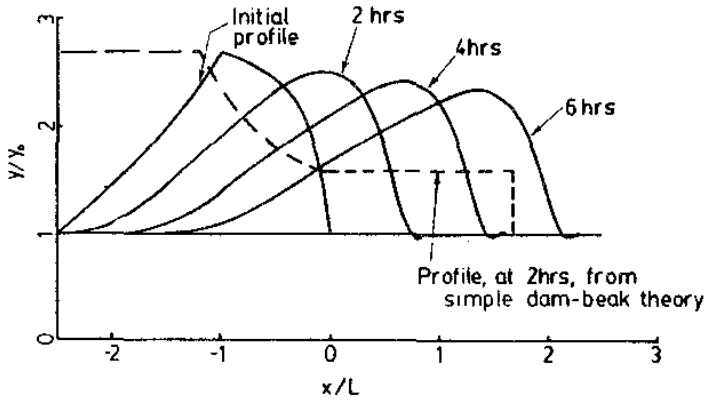

Figure 2.10: Variation of profile with time and distance [10]

Overall, while the argument that friction to flow will cause the surge wave to diminish in amplitude is plausible and consistent with observations, it is not clear how accurately the authors captured the presence of ice in their experiments. The inertia of the pellets compared to that of water is one consideration. Furthermore, the pellets did not provide significant resistance to flow from friction with the walls of the channel, as would happen with an ice jam breaking. Finally, it is not clear how much an ice jam during its release behaves like a collection of pellets with little friction between them, like a single mass, or like a collection of bodies with viscous-plastic

interactions between them.

Wong, Beltaos and Krishnappan [17] performed a series of experiments simulating surges created by ice jam releases. They compared their results with previous work done by Henderson et al [8] and Belaos et al [9], that has already been discussed. Their setup is depicted in Figure 2.11.

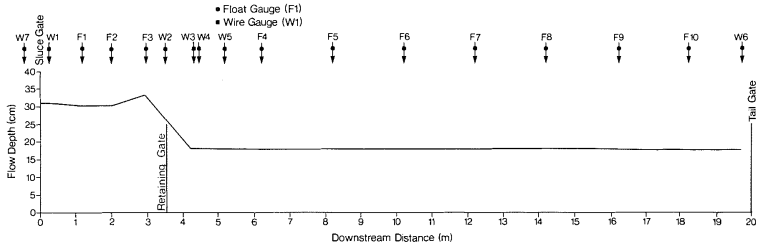

Figure 2.11: Schematic of experimental setup [17]

The jams were formed by feeding polyethylene blocks at the upstream end of a flume and obstructing their passage with a retaining gate. The gate was removed abruptly, to simulate the release. The resulting surges were recorded at various locations downstream, by monitoring the water depth and time of arrival of the surge at different locations. Altogether five runs were made and a summary of the hydraulic data is given in Figure 2.12, where a comparison of surge wave speeds was made with the results of the models by Beltaos and Krishnappan [9] and Henderson and Cooper [8].

There was some agreement between experimentally and mathematically derived surge wave speeds, as can be seen in the figure. Figure 2.13 shows experimentally produced surge profiles and their evolution with time at different locations, and compares them with results from the work of the aforementioned authors.

In comparing the experimental results with those of the model by Beltaos and Krishnappan [9], the authors assumed the initial free surface profile shown in figure 2.11 in the model, and the experimental boundary conditions upstream and downstream were the same as in the model. A step profile was assumed to compare the model of

	Time of arrival (s) of jam front at:	
	Location F5 (4.65 m from retaining gate)	Location F10 (14.65 m from retaining gate)
Run No. 1		
Observed	7 (0.66 m/s)*	46 (0.32 m/s)*
Predicted (Beltaos and Krishnappan)	9	53
Predicted (Henderson and Gerard)	8	24
Run No. 3		
Observed	11 (0.42 m/s)*	55 (0.27 m/s)*
Predicted (Beltaos and Krishnappan)	14	79
Predicted (Henderson and Gerard)	11	36
Run No. 5		
Observed	12 (0.39 m/s)*	65 (0.23 m/s)*
Predicted (Beltaos and Krishnappan)	16	72
Predicted (Henderson and Gerard)	18	56

*Value in parentheses is average speed of travel of the jam front.

Figure 2.12: Observed and predicted times of arrival of surge front [17]

Henderson with results. Figure 2.13 reveals good agreement between the experiments and the model by Beltaos and Krishnappan [9]. The irregularities in the waveforms were due to problems with the measuring apparatus. Reflected waves were also accurately reproduced. The experiments predicted a slow-down of the surge front, as was numerically derived from the work by Joliffe et al [10]. The authors concluded that, in agreement with the conclusion by Joliffe and Gerard [10], the presence of ice had little effect on the characteristics of surges. Furthermore, the results added validity

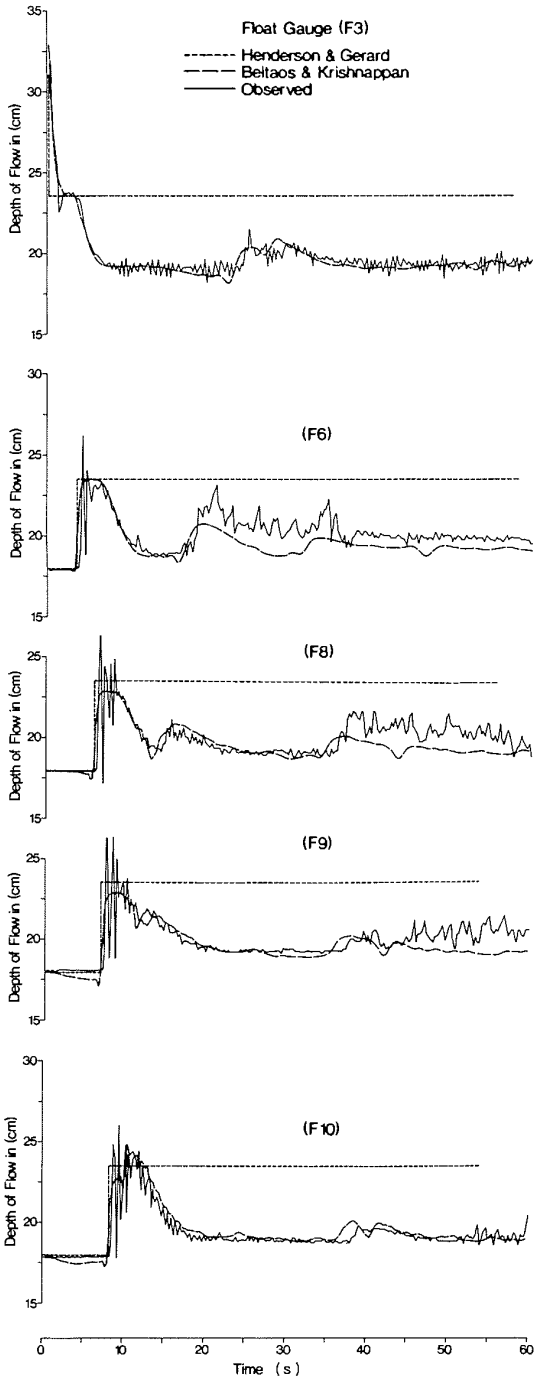

Figure 2.13: Comparison of surge profiles [17]

to the model developed by Beltaos and Krishnappan [9].

In 1997 Hicks, McKay and Shabayek [18] performed a numerical simulation of the documented 1991 ice jam release which occurred on the Saint John River, New

Brunswick [19]. The surge propagation analysis used a one-dimensional finite element model based on the St. Venant equations, called the cdg model and developed by Hicks and Steffler [20]. The model employs a Galerkin scheme to solve the one-dimensional unsteady open channel flow equations, that were modified for a channel of variable width. The topography of the river was recreated using available survey data, supplemented with topographic map data and approximated as a channel of rectangular cross-section and a variable width. The authors also accounted for lateral inflow from tributaries to the river. The equations on which the model was based were the St. Venant equations. For continuity the equation used was:

$$\frac{\partial A}{\partial t} + \frac{\partial Q}{\partial x} = q \tag{2.51}$$

and for momentum:

$$\frac{\partial Q}{\partial t} + \frac{\partial(\frac{Q^2)}{A})}{\partial x} + gA\frac{\partial H}{\partial x} + gAS_f = 0 \ , \tag{2.52}$$

where A is the flow cross sectional area, Q is the volume flow rate, H is the flow depth, S_f is the friction slope and g is the acceleration of gravity. The boundary conditions that the authors used in their model were a) the known inflow at the upstream end and b) an assumed constant stage downstream, based on observations. The final form of the free surface profile before the jam release can be seen in figure 2.14.

In the simulation the presence of ice was not explicitly taken into account. Figure 2.15 compares results with observations for the water levels at a specific location. The computed peak water surface elevation was off by a factor of two, higher than the observed value. The authors believed that the discrepancy could be due to not accounting for the presence of ice.

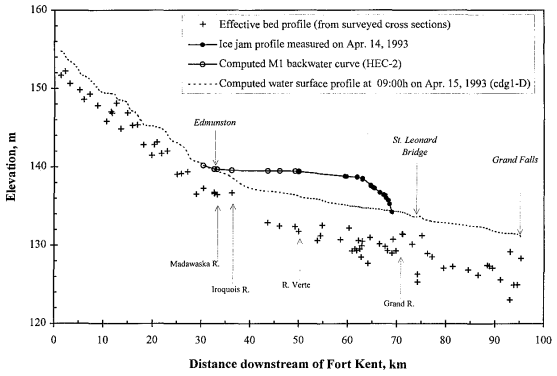

Figure 2.14: Bed profile and water levels used for the ice jam surge release simulation [18]

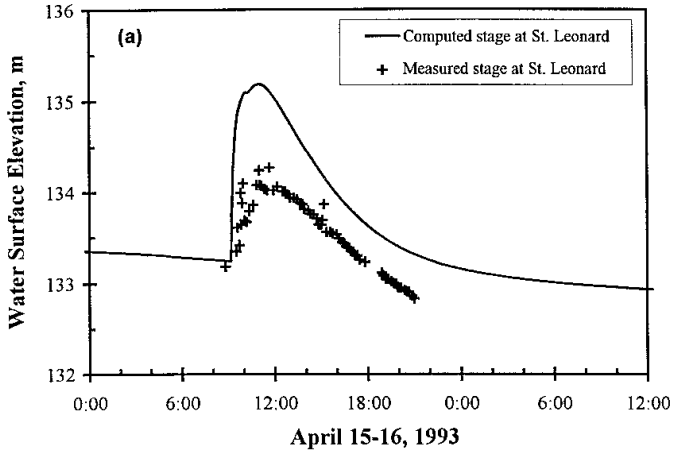

Figure 2.15: Water level comparison at a specific location [18]

Figure 2.16 presents the computed discharges at various locations. The computed results for surge wave speeds and rates of discharge compared favorably with observations, and added credibility to the model.

Finally, Figure 2.17 shows computed discharges along the river for various times. Ice jam release phenomena are associated with high flow velocities.

It is important to note that in the work of this thesis, as will be described below, the presence of ice was not taken explicitly into account. While the presence of ice bodies in the flow may affect the characteristics of the surge wave following the release of a jam, what is of interest and importance is the rise in flow velocities following the release. The work by Hicks et al [18] justifies the approach, since her results were in

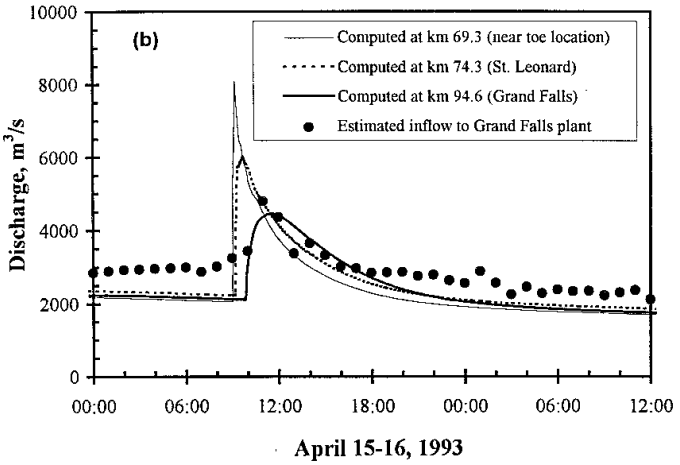

Figure 2.16: Water discharge for various locations [18]

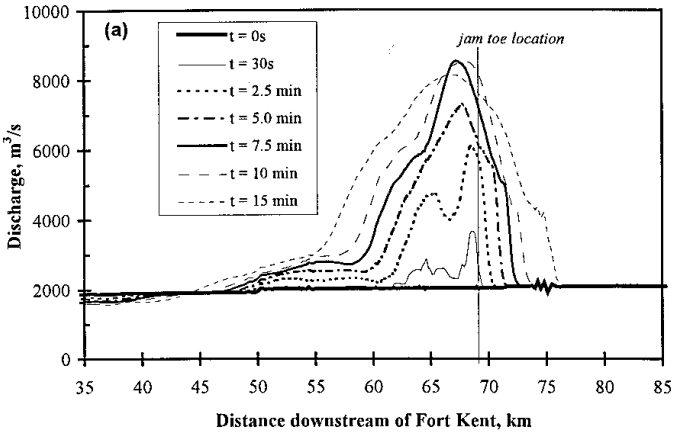

Figure 2.17: Water discharge for different times [18]

good agreement with observations in terms of discharge and flow velocity elevations. This agreement was apparent even in earlier work by Henderson et al [8]. It seems that the presence of ice affects more the changes in water surface elevation than it does the changes in flow discharge during the release of an ice jam.

In terms of the effects that the presence of ice might have on the characteristics of the surge wave following a jam release, in 2003, Jasek [36] presented a detailed study of ice jam release processes, based on field observations. He concluded that, in contrast to the conclusions of previous experimental studies by Joliffe and Gerard [10] and Wong et al. [17], the presence of ice has a significant effect on the character-

istics of a jam release surge, and should be taken into account in subsequent studies. Field observations showed that in an unimpeded ice run, the surge included ice for considerable distances downstream, which affects the nature of the surge.

In 2003, Hicks and Blackburn [33] revisited the case of the 1991 ice jam release event in the Saint John River [19], which had been studied by Hicks et al in 1997 [18]. Their main goal was to study the effects of a more realistic geometry in their model, as opposed to the original work [18], which had assumed a rectangular channel. Their model was based on the modified St Venant equations; The momentum equation used was:

$$\frac{\partial Q}{\partial t} + \frac{\partial(\frac{\beta Q^2}{A})}{\partial x} + gA\frac{\partial H}{\partial x} - gAS_f = 0 \ , \tag{2.53}$$

where the term β is the momentum flux correction coefficient, that accounts for non-rectangular variation in channel geometry. Q is the volumetric flow rate, A is the variable cross-sectional area, g is the acceleration of gravity and H is the water level height. S_f is the friction slope. To solve the equations, the finite element model was used, one that had been used in the previous study by Hicks [18]. In addition to studying the effect of variable channel geometry, the authors made a first attempt to account for the presence of ice by simulating a more gradual release. The boundary conditions were the river inflow, as well as the inflow from the tributaries, and the water level downstream. The domain was divided into two sections with respect to the Manning coefficient, n, assigning a different value in each domain. Also, while the 1997 study [18] modeled the jam based on information 24h old, the authors updated the jam thickness, based on the discharge right before release, which had decreased.

Three runs were made. The first run neglected the effects of ice and did not implement a gradual release. Figure 2.18 compares results with respect to water

levels at a specific location downstream.

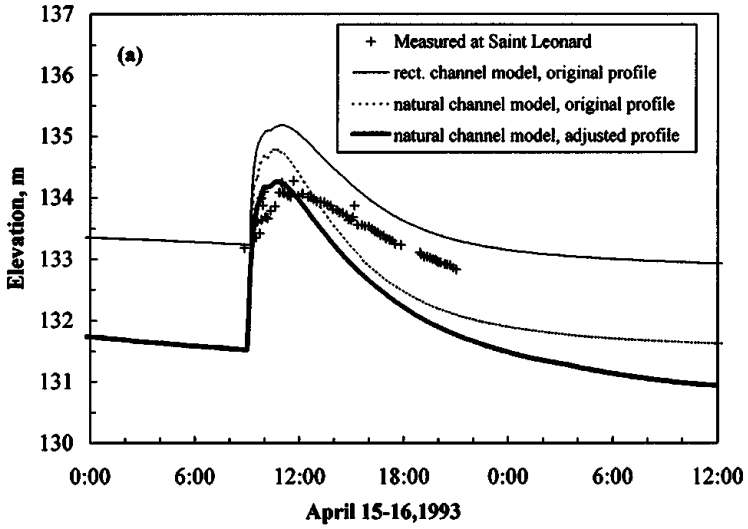

Figure 2.18: Comparison of measured and computed stage [33]

Figure 2.19 shows the comparison with respect to discharge.

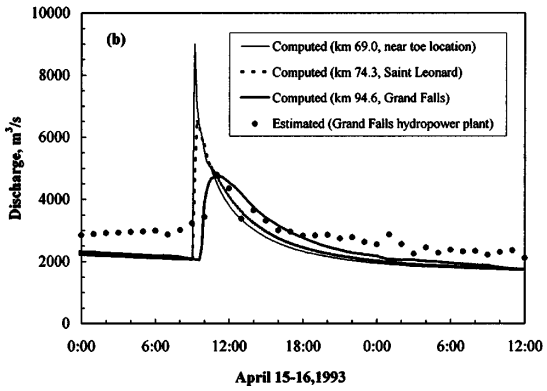

Figure 2.19: Comparison of measured and computed water discharge for different times [33]

The conclusion was that, with respect to water surface level, the natural geometry and updated jam profile fit the measured data well. There was, however, a discrepancy concerning the recession portion of the computed stage hydrograph, in that it was much lower than the measured one. It should be noted that the model accurately predicted the time of arrival of the surge front. With respect to discharge, there

was a discrepancy between computed and measured values before the surge, with the computed values being quite lower. Run 2 provided a sensitivity analysis with respect to channel roughness, by increasing Manning's n. The results showed that the computed peak water level was higher than in run 1. Increasing the roughness did not affect the speed of propagation of the surge. In terms of the effect that Manning's n had on peak water levels, the results were in disagreement with those from the numerical study by Joliffe et al [10], who had concluded that the presence of friction lead to a gradual decrease in peak water levels with distance and time. Run 3 included the effect of the presence of ice, by doubling the wetted perimeter and increasing Manning's n in the location of the jam. After 15min, the resistance effect was removed. The results, with respect to water levels and discharges downstream of the toe, were identical to those of run 1, where presence of ice had been neglected. However, there were significant differences (50%) in discharge levels between the two runs in the region of the jam itself, as can be seen in Figures 2.20 and 2.21.

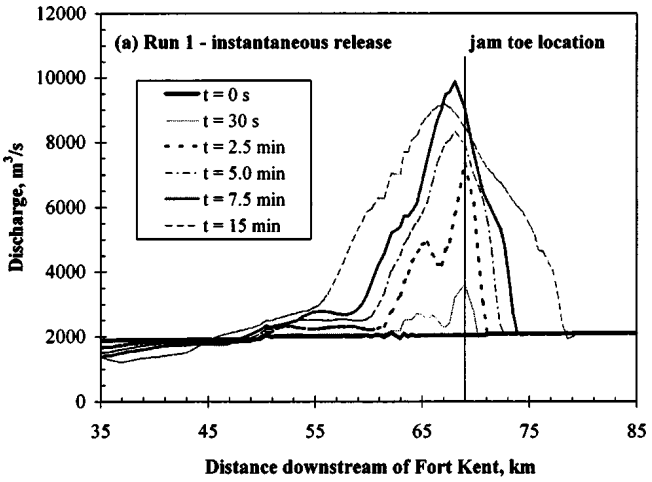

Figure 2.20: Computed discharge in the jam region for run 1 [33]

Overall, this study was inconclusive in terms of the contribution of an accurate geometry, because the model was unable to reproduce the shape of the recession portion of the observed stage hydrograph. Furthermore, it was also inconclusive with respect

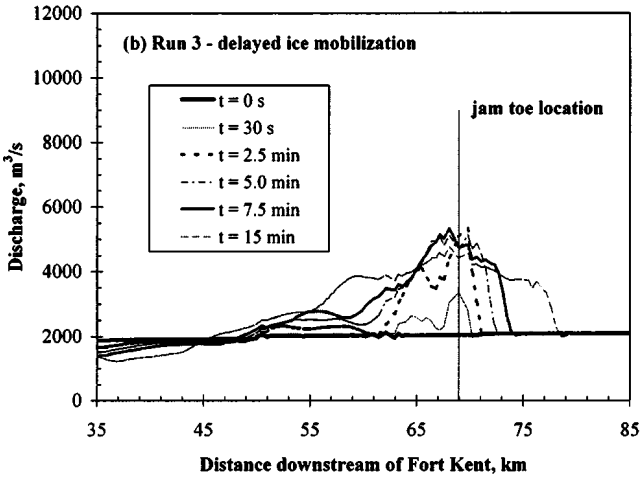

Figure 2.21: Computed discharge in the jam region for run 3 [33]

to discharge evolution, since the authors were not able to capture the measured discharge value before the jam release. In the work of this thesis, the hydrodynamic model allowed for adjustments in discharge levels presence of a stationary ice jam. The adjustments were possible by adjusting the geometry of the stationary ice jam, to match reduced discharge levels presence of the jam, which were known from observations.

In 2004, Liu and Shen [34] presented their work on ice jam release surges by incorporating the presence of ice as a separate continuum in their model. They compared their results with those of the work by Hicks et al [33] and showed that the presence of ice significantly affected the characteristics of the surge. The model that was used was a 2D coupled flow and ice dynamic model (DynaRICE), that had been previously developed by the authors [35]. The model was based on the depth integrated momentum equations. The hydrodynamic component of the model used a finite element scheme, capable of handling high velocity and transitional flows. The surface ice was treated as a continuum and internal resistance was taken into account, formulated with a viscous-plastic constitutive law. The momentum equation in Lagrangian form for the ice layer was:

$$M\frac{DV}{Dt} = R + F_a + F_w + G \ , \tag{2.54}$$

where all quantities are vector quantities. M is the ice mass per unit area, V is the ice velocity, R is the internal ice resistance, F_a is the wind drag, F_w is the water drag, and G is the gravitational force. Ice mass conservation was:

$$\frac{DM}{Dt} + M\nabla \cdot V = 0 \ . \tag{2.55}$$

The continuity equation for water flow was:

$$\frac{\partial H}{\partial t} + \bigtriangledown \bullet (q_1 + q_i + q_s) = \frac{\partial}{\partial t}(Nt_i') \ , \tag{2.56}$$

where H is the total water depth, q_1 is the unit width discharge of water under the ice, q_i is the water flow due to water entrained in the moving ice, and q_s is the apparent seepage velocity in the ice layer, produced by the hydraulic gradient. t_i' is the submerged ice thickness and N is the ice concentration in the form of volume of ice per unit volume. The momentum equations were derived as follows:

$$\frac{\partial q_{1x}}{\partial t} + \frac{\partial}{\partial y}(\frac{q_{1y}^2}{H'}) + \frac{\partial}{\partial y}(\frac{q_{1x}q_{1y}}{H'}) = -gH'\frac{\partial \eta}{\partial x} + \frac{1}{\rho}(\tau_{bx} - \tau_{sx}) + \frac{1}{\rho}\frac{\partial T_{xx}}{\partial x} + \frac{1}{\rho}\frac{\partial T_{xy}}{\partial y} \tag{2.57}$$

and

$$\frac{\partial q_{1y}}{\partial t} + \frac{\partial}{\partial x}(\frac{q_{1x}^2}{H'}) + \frac{\partial}{\partial x}(\frac{q_{1x}q_{1y}}{H'}) = -gH'\frac{\partial \eta}{\partial y} + \frac{1}{\rho}(\tau_{by} - \tau_{sy}) + \frac{1}{\rho}\frac{\partial T_{yy}}{\partial y} + \frac{1}{\rho}\frac{\partial T_{yx}}{\partial x} \ , \quad (2.58)$$

where q_{1x} and q_{1y} are x and y components of the water mass flow rate per unit width, H' is the depth of water beneath the ice layer, g is the acceleration of gravity and ρ is water density. η is the depth of water above a reference level. τ_{bx} and τ_{by} are bottom x and y shear stress components and τ_{sx} and τ_{sy} are x and y components of the shear stress on the ice. Also:

$$T_{jk} = \epsilon_{jk}^{w}(\frac{\partial q_{1j}}{\partial x_k} + \frac{\partial q_{1k}}{\partial x_j}) \ , \quad (2.59)$$

where ϵ_{jk}^{w} is the eddy viscosity. When applying the model, the authors used a rectangular channel, with a similar slope and length to that of the Saint John River, that had been studied by Hicks et al. [18], [33]. A constant Manning's coefficient was used. Figure 2.22 shows the initial state of the jam, just before release. There was a spike in the flow velocity at the jam toe that was consistent with the work, much earlier, by Mercer and Cooper [13] who had studied scouring in that location because of elevated flow velocities and stresses on the bed. The spike is due to the fact that flow is constricted to a much smaller cross-sectional area under the jam and is forced to move at higher average velocities. However, both the work by Mercer and Cooper [13] and by Liu and Shen [34] was based on models that did not account for non-hydrostatic effects. Figure 2.23 shows the simulated evolution of the jam, once it was released. While the jam was mobile, the flow velocity was high at the moving toe region.

Figure 2.24 shows the increase in stage elevation at various locations downstream, and at different times,

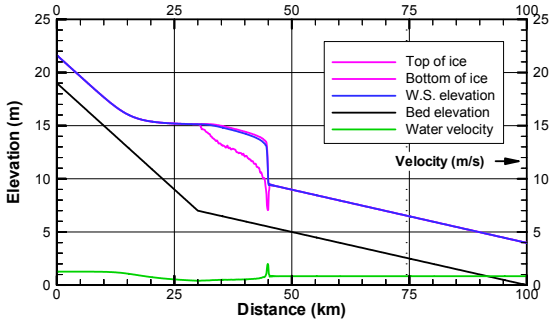

Figure 2.22: Initial state of the jam [34]

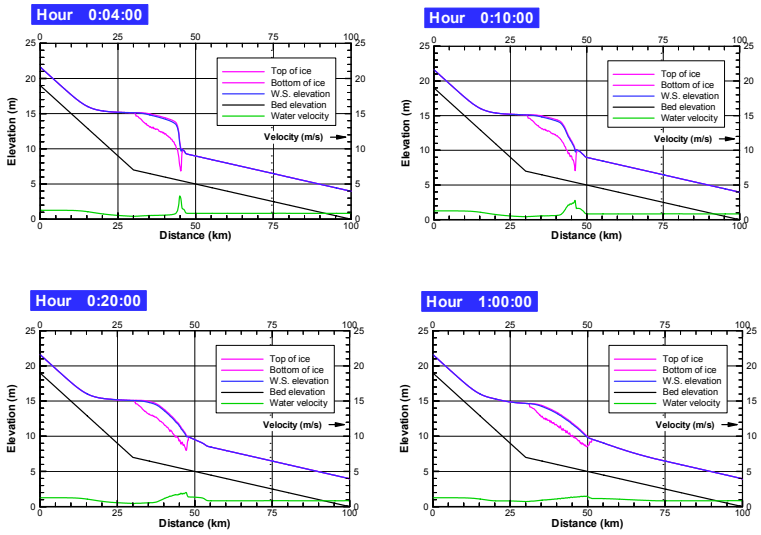

Figure 2.23: Evolution of the jam [34]

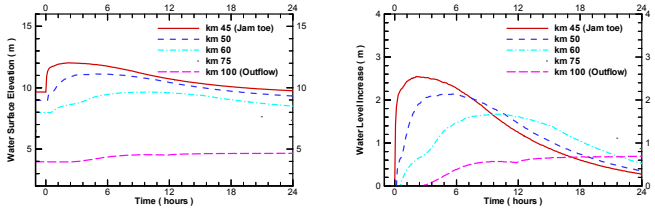

Figure 2.24: Changes in stage elevation downstream [34]

while figure 2.25 shows the changes in discharge at different locations (and times) downstream.

The authors ran a simulation neglecting the presence of ice, and the comparison of their results with and without accounting for the presence of ice is shown in

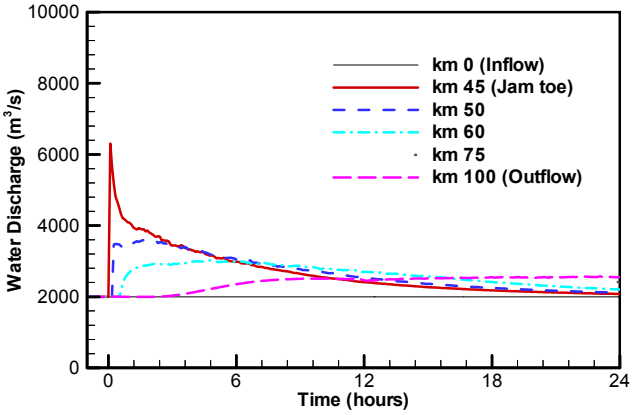

Figure 2.25: Change in discharge downstream [34]

figures 2.26 and 2.27.

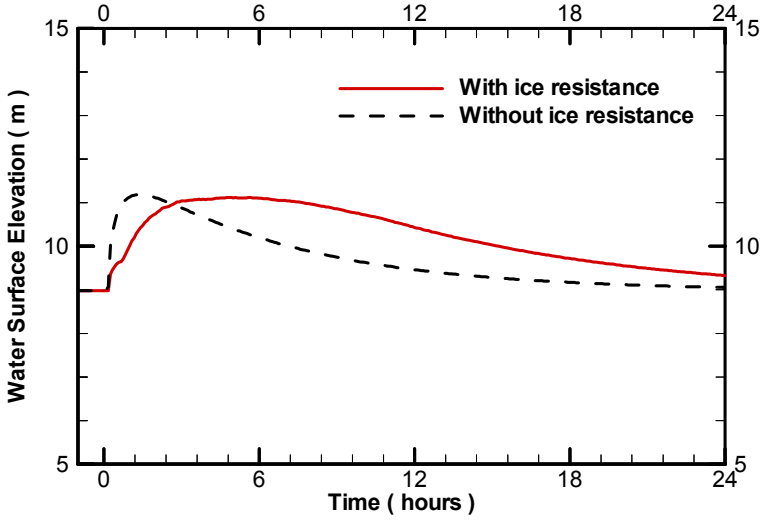

Figure 2.26: Comparison of stage elevation with and without the presence of ice [34]

The results showed that there was a significant effect of the presence of ice; while the peak water surface elevation in the comparison was the same, the increase was more gradual presence of ice and persisted longer. With respect to discharge, the presence of ice had an initial dampening effect on the peak, but higher flows persisted longer. The presence of ice delayed the release process. In their study, accurate river geometry was not considered and a constant Manning's coefficient, n, was used, since

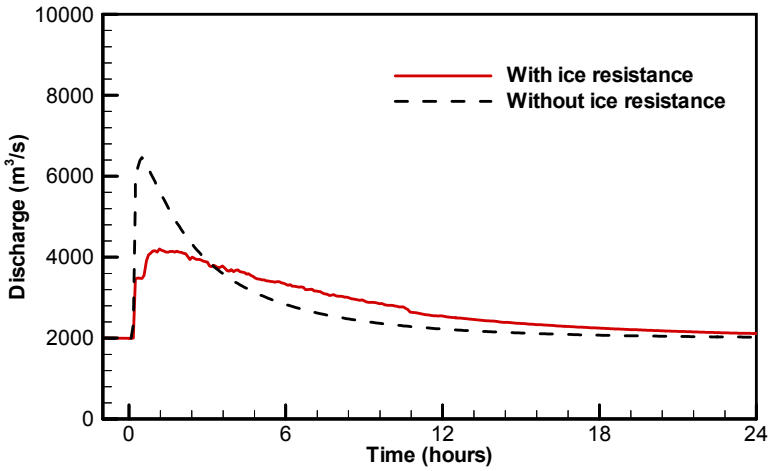

Figure 2.27: Comparison of discharge with and without the presence of ice [34]

the authors wanted to emphasize the importance of taking into account the presence of ice. As such, the authors did not compare their results with observations. Since the authors did not juxtapose their numerical findings with observational estimates, it is difficult to say to what extent their model was accurate. In terms of the work in this thesis, it will be shown that accuracy in capturing the very initial rise in flow velocities is not essential in determining whether there will be scouring in St. Clair River during and after the release of a jam. This is because a significant amount of scouring will take place during the prolonged high flow velocities after the initial spike and the passage of ice. In fact, if Liu and Shen [34] were right, higher prolonged flow velocities after the initial phase of a delayed release will contribute to even more scouring than predicted by the model in this thesis.

In 2005, Hicks et al. [37] applied the finite element model that had been used in previous studies [18] and [33], but incorporated ice effects more comprehensively than they had done previously [33], in order to reproduce the results by Shen et al [34] and the DynaRICE model that they had developed. A comparison was also made between simulations and field data from the Saint John River ice jam release event [19]. The formulation of the model was based on the assumption that released ice moves with

the surface water velocity. The equations of total (ice + water) mass and momentum were solved, and, separately, mass conservation for ice was solved. Bank resistance to ice movement was accounted for by introducing a resistance term to the total flow momentum equation. Longitudinal diffusion of the ice mass was approximated with an empirical diffusion term in the ice mass continuity equation. In comparing the results with those of Shen et al. [34], the same rectangular channel was used. Total flow continuity was:

$$\frac{\partial A}{\partial t} + \frac{\partial Q}{\partial x} = 0 \tag{2.60}$$

and total flow momentum gave:

$$\frac{\partial Q}{\partial t} + \frac{\partial UQ}{\partial x} + gA\frac{\partial H}{\partial x} = -gAS_f + gAS_o - 2R_i gB\eta S_f \ , \tag{2.61}$$

where H is water surface elevation, A is the total cross sectional area, Q is total discharge, U is the ice and water velocity and η is the ice thickness; R_i is a resistance coefficient that accounts for friction between ice and the banks. S_f is the friction slope, given by:

$$S_f = \frac{n^2 U|U|}{R^{\frac{4}{3}}} \ , \tag{2.62}$$

where n is Manning's coefficient and R the hydraulic radius. Continuity for ice was:

$$\frac{\partial \eta}{\partial t} + \frac{\partial U\eta}{\partial x} = D\frac{\partial^2 \eta}{\partial x^2} \ , \tag{2.63}$$

where D is an artificial numerical diffusion coefficient, that accounts for the longitudinal diffusion of ice. The coefficients D and R_i were adjusted for optimal results. Figure 2.28 gives a comparison with Shen's results [34], with respect to stage elevation, while Figure 2.29 gives a comparison with respect to discharge. Figure 2.30 shows a comparison with respect to the evolution of the ice jam profile.

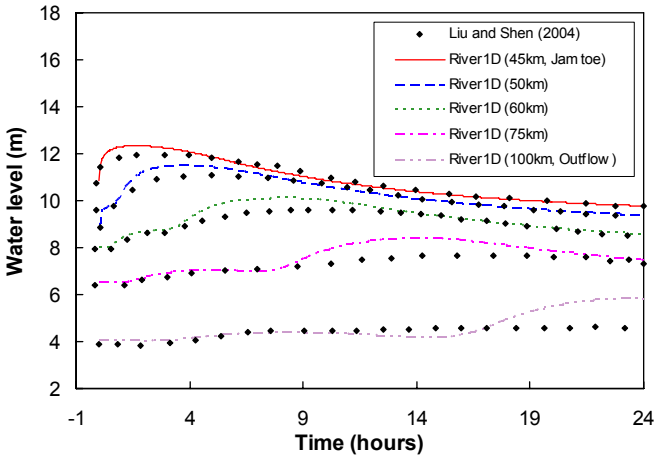

Figure 2.28: Comparison of water levels [37]

Shen's results [34] were accurately reproduced. Figure 2.31 shows a comparison between simulations with and without taking ice into consideration, with respect to water surface elevations and discharges for two locations.

As can be seen, the model reproduces differences between results that do and do not include the effects of the presence of ice. The authors applied their model to the Saint John River event, which had been previously studied [18] and [33]. The results were inconclusive, as there were marked differences in numerically derived and observed water levels for both the case without ice and with ice, as can be seen in Figure 2.32.

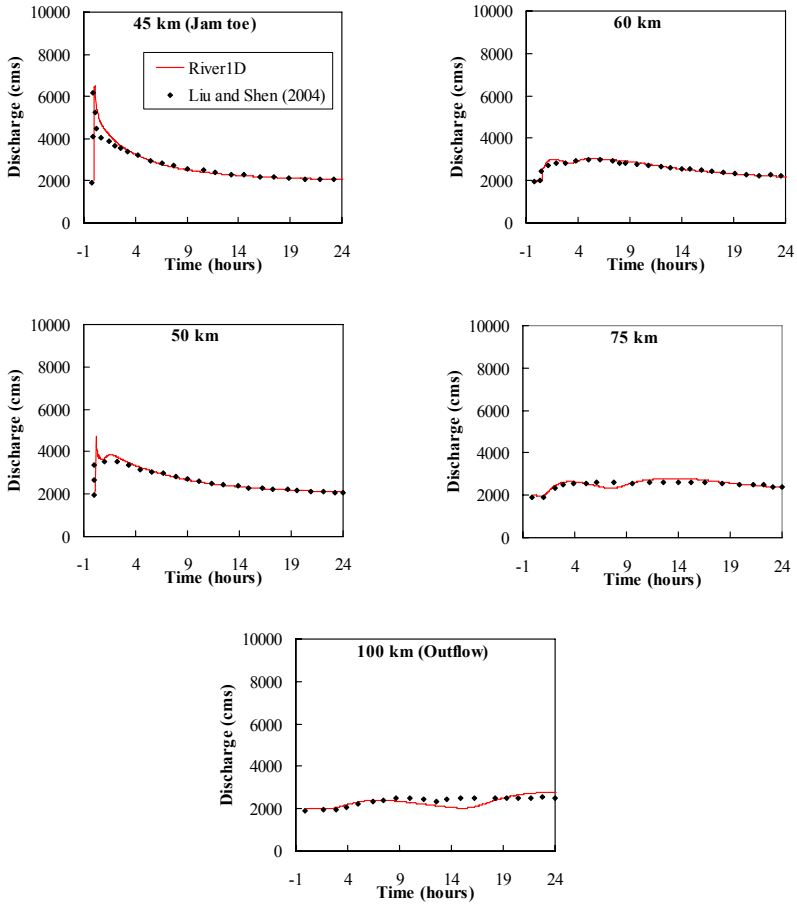

Figure 2.29: Comparison of discharges [37]

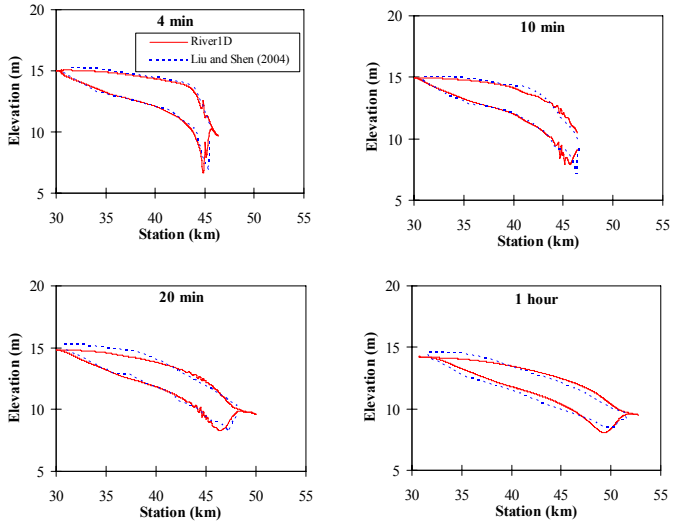

Figure 2.30: Comparison of ice jam evolution [37]

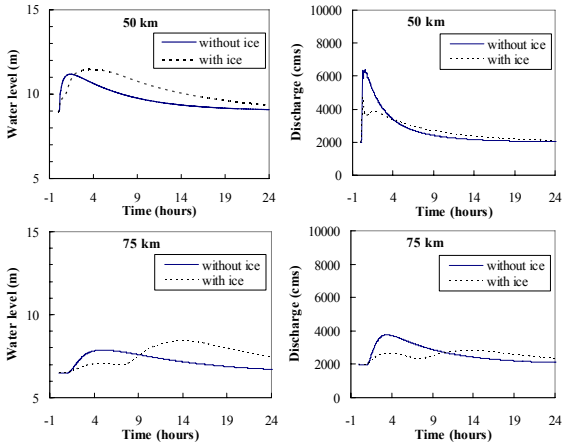

Figure 2.31: Simulation result comparisons with and without ice effects [37]

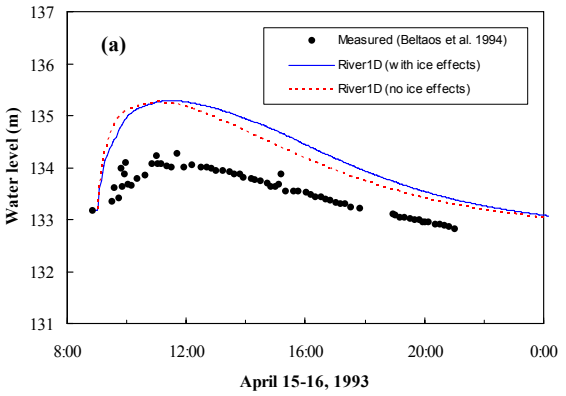

Figure 2.32: Comparison between simulation and observations for water levels [37]

2.2 A Numerical Study of the 1984 Ice Jam Event

In 2009, in response to the report by Beltaos [39], Kolerski and Shen [38] presented a case study of the 1984 jam event, where they applied the DYNARice model that was previously developed by Shen et. al [35]. The map of the region is shown in Figure 2.33.

The jam first formed at Port Lambton, on April 6, gradually grew upstream to reach St. Clair, and then stabilized. The jam released April 30th. Bathymetric data were obtained and the region was meshed with triangular elements. Nine zones with different Manning's coefficients were used, and the model was calibrated with respect to the coefficients, as well as ice discharge and concentration from Lake Huron, based

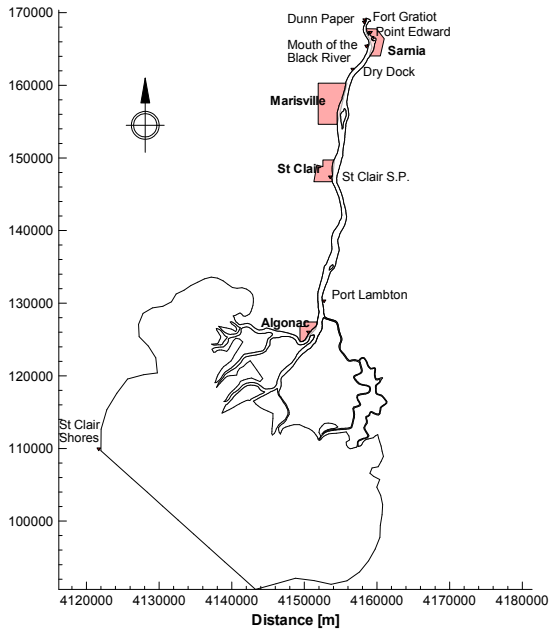

Figure 2.33: Map of the St. Clair River [38]

on recorded water levels at various locations upstream and downstream of the jam. The following formulas were used to estimate shear stresses on the bed:

$$\tau_{bx} = c_f \rho \frac{q_x (q_x^2 + q_y^2)^{\frac{1}{2}}}{H'^2} \tag{2.64}$$

and

$$\tau_{by} = c_f \rho \frac{q_y (q_x^2 + q_y^2)^{\frac{1}{2}}}{H'^2} \ , \tag{2.65}$$

where τ_{bx} and τ_{by} are bed shear stress components, c_f is the friction coefficient and q_x and q_y are flow rates. H' is the depth of water under the ice. Based on their simulations for the period prior to the release, the authors found that the flow velocities under the ice jam did not significantly differ from the open water ones. The jam began to release on April 28 and by April 30 had fully released. Figure 2.34 shows

the maximum increase in estimated bed shear during the period of the stationary jam, compared to open water conditions.

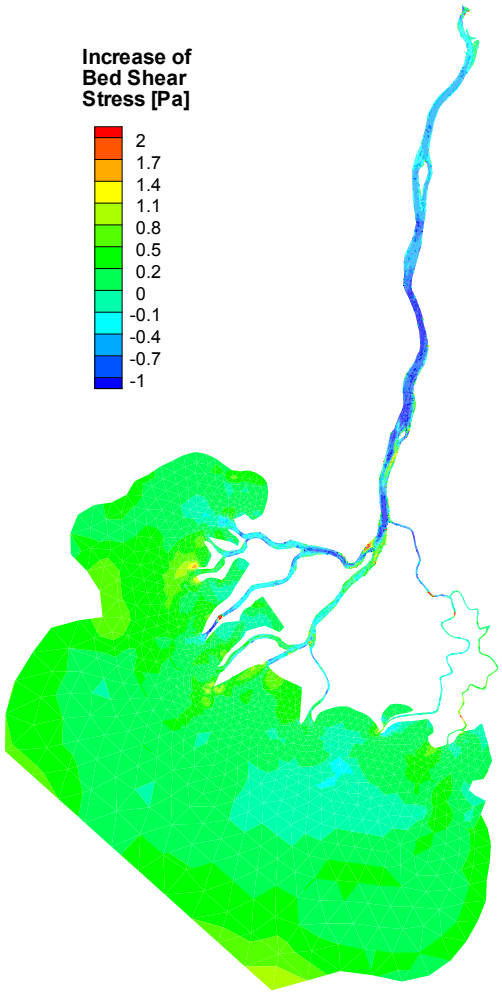

Figure 2.34: Increase of bed shear stress due the presence of the jam (ice condition minus May 1st open water condition) [38]

Based on their simulation results, the authors concluded that the presence of the jam would have had negligible impact on bed scouring.

With respect to the work by Kolerski and Shen [38], certain points need to be addressed. The authors studied the possible impact on scouring of the presence of the 1984 jam, prior to its release. It will be shown in this work that, according to numerical results, the bed stresses during the time the jam was in place were actually

lower than in normal open water conditions. Scouring was found to happen during and after the release of the jam, as a result of the ensuing high flow velocities, not before its release. Furthermore, the model by Kolerski and Shen was based on the depth-integrated momentum equations. A two-dimensional hydrostatic model cannot adequately capture a jam release phenomenon, which is characterized by strong three-dimensional turbulence and non-hydrostatic pressure gradients. Even under normal open water conditions, it is unclear whether a two-dimensional model can accurately capture the stresses on the St. Clair River bed, which are the product of complex three-dimensional turbulent flow patterns.

2.3 Hydrodynamic Models that Have Been Used in the Huron-Erie Corridor

Due to the significance of the region, hydrodynamical models of the HEC or its components have been developed since before the 80s. A map of the region can be seen in figure 2.35 and figure 2.36.

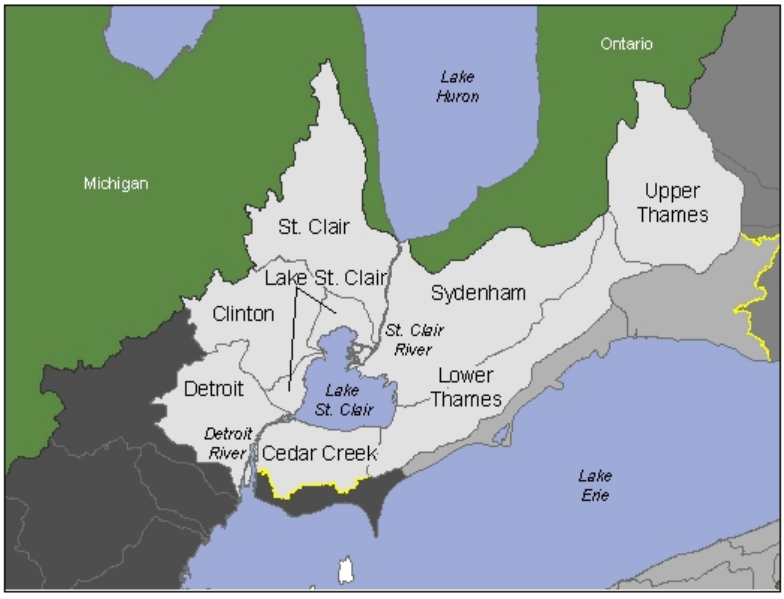

Figure 2.35: The Huron Erie Corridor

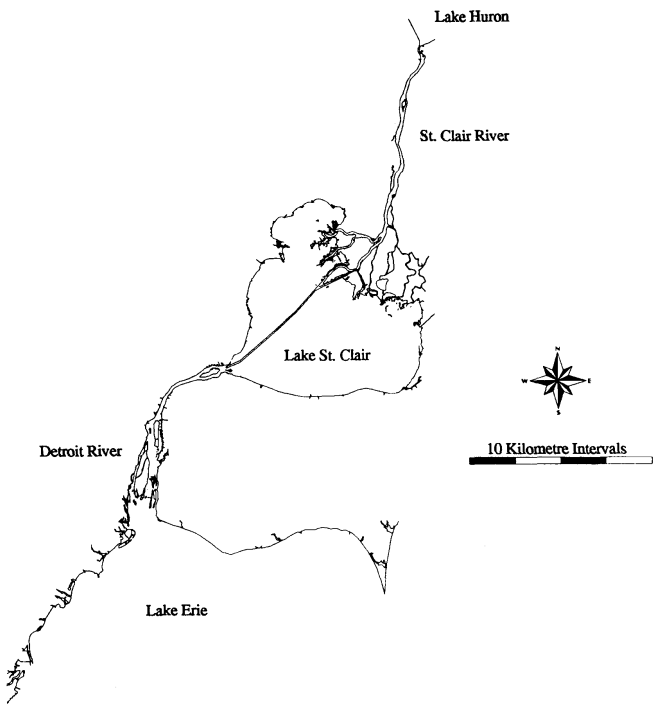

Figure 2.36: The St.Clair/Detroit River System

2.3.1 River Models

Quinn and Wylie [21] published in 1972 their work on a 1D, transient flow model, applied to the Detroit River, that connects lake St. Clair to lake Erie. The model solved the 1D continuity and momentum equations with a finite difference implicit scheme. The momentum equation used was:

$$\frac{1}{A}\frac{\partial Q}{\partial t} - \frac{2QT}{A^2}\frac{\partial z}{\partial t} + (g - \frac{Q^2T}{A^3})\frac{\partial z}{\partial x} + \frac{gn^2Q|Q|}{2.208A^2R^{\frac{4}{3}}} = 0 \ , \tag{2.66}$$

where Q is the volume flow rate, x is the distance in the flow direction and A is the channel cross-sectional area. T is the channel width, z is the water surface elevation, g is the acceleration of gravity, R is the hydraulic radius and n is Manning's roughness coefficient. The last term on the right accounted for shear-induced resistance to flow. The Detroit River was modeled in idealized form, as seen in Figure 2.37.

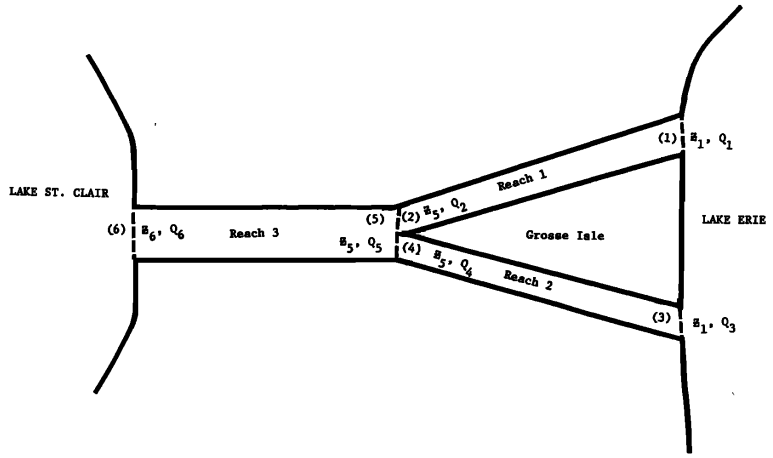

Figure 2.37: The Detroit River model [21]

Three Manning's coefficients were used, one for each reach (see Figure 2.37), which were obtained by calibrating the model in order to most accurately reproduce measured flow conditions. A sensitivity to the roughness coefficient analysis was performed in that study. The formula used for the Manning's coefficient is given below:

$$n = \frac{1.486AR^{\frac{2}{3}}}{Q}\left(\frac{(WSUP - WSDN)}{L} + \frac{Q^2\Delta A}{32.2LA^3}\right)^{\frac{1}{2}} , \tag{2.67}$$

where WSUP was the water surface elevation at the upstream gage, WSDN was the water surface at the downstream gage, ΔA was the difference in area between the upstream and downstream gages, and L was the length of the reach from upstream to downstream gage. The boundary conditions used were the water surface elevations at lakes St. Clair and Erie. The initial conditions were set by specifying water surface elevations at Lake St. Clair and Lake Erie and computing an approximate steady state flow configuration for each reach. The output of the model consisted of the flows at each end of the three reaches of the model/river, as well as the water surface elevations at the junction of the reaches.

Quinn also studied the effects of wind stress on the hydrodynamics of the HEC [23]. Again, the model solved the continuity and momentum equations for 1D unsteady flow, but a surface wind stress, τ_w, was included as:

$$\tau_w = \rho_a C_D U^2 \ , \tag{2.68}$$

where ρ_a is the air density, C_D is the drag coefficient, and U is the wind velocity. The momentum equation, from equation (2.66) was modified to:

$$\begin{gathered} \frac{1}{A}\frac{\partial Q}{\partial t} - \frac{2QT}{A^2}\frac{\partial z}{\partial t} + (g - \frac{Q^2 T}{A^3})\frac{\partial z}{\partial x} + \\ \frac{gn^2 Q|Q|}{2.208 A^2 R^{\frac{4}{3}}} - \frac{\rho_a}{\rho_w}\frac{U^2 cos(\phi - a)|cos(\phi - a)|C_D T}{1} = 0 \end{gathered} \ , \tag{2.69}$$

where ϕ is the channel azimuth, a is the wind direction and ρ_w is the water density. The resultant wind speeds were taken from measurements at the Detroit City Airport. It was found that the addition to the preexisting model [21] of wind shear effects for the annual average wind amounted to a 4.3% flow reduction in the Detroit River. The maximum daily wind effect was approximately a 7% reduction in flow. It was concluded that the inclusion of wind effects had little influence on monthly flow rates in the Detroit River, or the water level in Lake Erie (5mm difference in depth). However, wind had a significant effect on the water level in Lake St. Clair, equivalent to a 111mm depth difference. Variations of the model by Quinn [21] were presented in the late 70s and early 80s, [22], [24], based on the same 1D equations of continuity and momentum with or without the addition of wind effects. Their differences lay primarily in the degree of spatial/temporal discretization, as well as the frequency and accuracy of hydrodynamical measurements in the HEC.

Tsanis et al. [27] presented in 1996 a steady 2D turbulent model, called the RMA2 model, applied to the St. Clair and Detroit Rivers. The goal of the model was to accurately simulate river currents, in order to be able to track the movement and dispersion of pollutants. The equations used were the depth-integrated equations of momentum and continuity, as presented below; x - momentum was:

$$\frac{\partial u}{\partial t} + u\frac{\partial u}{\partial x} + v\frac{\partial u}{\partial y} + g\frac{\partial h}{\partial x} + g\frac{\partial a_o}{\partial x} - \frac{\epsilon_{xx}}{\rho}\frac{\partial^2 u}{\partial x^2} - \frac{\epsilon_{xy}}{\rho}\frac{\partial^2 u}{\partial y^2} - 2\omega v sin\phi + \frac{gu}{C^2 h}(u^2+v^2)^{\frac{1}{2}} - \frac{\xi V_a^2}{h}cos\psi = 0 \ . \tag{2.70}$$

y - momentum was:

$$\frac{\partial v}{\partial t} + u\frac{\partial v}{\partial x} + v\frac{\partial v}{\partial y} + g\frac{\partial h}{\partial y} + g\frac{\partial a_o}{\partial y} - \frac{\epsilon_{yx}}{\rho}\frac{\partial^2 v}{\partial x^2} - \frac{\epsilon_{yy}}{\rho}\frac{\partial^2 v}{\partial y^2} - 2\omega u sin\phi + \frac{gv}{C^2 h}(u^2+v^2)^{\frac{1}{2}} - \frac{\xi V_a^2}{h}sin\psi = 0 \tag{2.71}$$

and continuity was:

$$\frac{\partial h}{\partial t} + \frac{\partial uh}{\partial x} + \frac{\partial vh}{\partial y} = 0 \ , \tag{2.72}$$

where u and v are depth averaged flows in the x and y direction respectively, g is the acceleration of gravity, h is water depth and a_o is the water surface elevation. ϵ_{xx} and ϵ_{yy} are turbulent viscosities, in the x and y direction respectively. ϵ_{xy} and ϵ_{yx} are tangential turbulent eddy viscosities, in the x and y direction. ω is the Earth's angular rotation velocity, ρ is density and ϕ is latitude. C is the Chezy roughness

coefficient and ξ is a coefficient relating wind speed to stress exerted on the water surface. V_a is wind velocity and ψ is the angle between wind direction and the x-axis. The three equations were solved by the finite element method in an unstructured grid, which facilitated the more accurate capturing of the physical geometry. Bed friction was calculated with Manning's equation. The following formula was used for Manning's n:

$$n = 0.0382 k_s^{\frac{1}{6}} \ , \tag{2.73}$$

where k_s is the equivalent roughness that depends on the bed roughness, and was fixed, since n was fixed. The authors accounted for the fact that horizontal velocities were not uniformly distributed in turbulent flow. The velocity profiles were approximately logarithmic and could be expressed by:

$$\frac{u(z)}{u_*} = 2.5 ln(\frac{30.1z}{k_s}) \ , \tag{2.74}$$

where u(z) is the velocity as a function of distance from the bed and u_* is the shear velocity. The shear velocity was given by:

$$u_* = \sqrt{ghS_f} \ , \tag{2.75}$$

where S_f is the friction slope, that can be calculated via Manning's formula as:

$$S_f = (nU/R_h^{\frac{2}{3}})^2 \ , \tag{2.76}$$

where R_h is the hydraulic radius and U is the depth averaged flow velocity. Setting $z = h$ in equation (2.74) gave:

$$\frac{u_s}{u_*} = 2.5ln(\frac{30.1h}{k_s}) \ , \tag{2.77}$$

where u_s is the flow velocity at the water surface. Integrating equation (2.74) from the bottom to the water surface, and dropping small terms, the following formula was derived:

$$\frac{U}{u_*} = 2.5ln(\frac{11.0h}{k_s}) \ . \tag{2.78}$$

Combining equations (2.77) and (2.78), the authors derived:

$$u_s = \frac{U}{ln(11.0h/k_s)} ln \frac{30.1h}{k_s} \ . \tag{2.79}$$

From (2.79), the surface velocity could be calculated from the depth-averaged velocity, and was 15 - 20% higher than the latter. The authors used the depth-averaged velocities derived from their model to calculate surface velocities, from which they could compute the movement of surface pollutants. For the model, the upstream boundary condition was a given discharge, and the downstream boundary condition was water surface elevation. Both were fixed during the runs. The outputs of the model were water surface heights and discharges. The models were run for sections of the St. Clair and Detroit rivers, and the results were compared to field observations. Generally, there was very good agreement between simulations and field data. An example is given by Figure 2.38, where simulated and observed discharges in a

bifurcation of River St. Clair are compared.

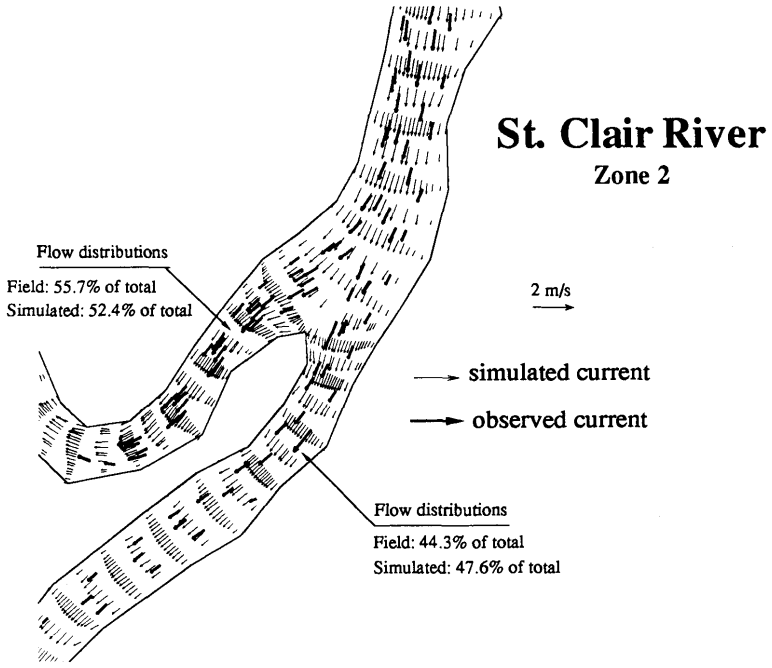

Figure 2.38: Comparison of simulated and observed results in a location of River St. Clair [27]

2.3.2 Lake Models

In 1981 Schwab, Bennett and Jessup [25] presented two 2D unsteady flow models applied to Lake St. Clair. The first was a free surface (gravitational response) model, intended for forecasting water level fluctuations. The second model was intended to simulate large scale circulation in the lake, and free surface fluctuations were neglected (rigid lid) in order to save in computational time. Both models were based on the vertically integrated shallow water equations. For the first model, x-momentum gave:

$$\frac{\partial M}{\partial t} - fN = -gD\frac{\partial H}{\partial x} + \rho^{-1}\tau_x^S - \rho^{-1}\tau_x^B \ . \tag{2.80}$$

y-momentum:

$$\frac{\partial N}{\partial t} - fM = -gD\frac{\partial H}{\partial y} + \rho^{-1}\tau_y^S - \rho^{-1}\tau_y^B \tag{2.81}$$

and continuity:

$$\frac{\partial H}{\partial t} + \frac{\partial M}{\partial x} + \frac{\partial N}{\partial y} = 0 \ , \tag{2.82}$$

where M and N are the components of the vertically integrated transport vector in the x and y directions respectively; H is the water level displacement from its mean value and D is the depth; f is the Coriolis parameter, with $f = 2\omega sin\phi$, where ω is the angular speed of rotation of the earth, and ϕ is latitude; g is the acceleration of gravity and ρ is the density of water; τ_x^S and τ_y^S are the x and y components of the wind stress vector, and τ_x^B and τ_y^B are the x and y components of the bottom stress vector. The following constitutive equations were provided for the bottom stress:

$$\tau_x^B = \frac{C_D}{D^2}\sqrt{M^2 + N^2}M \tag{2.83}$$

and

$$\tau_y^B = \frac{C_D}{D^2}\sqrt{M^2 + N^2}N \ . \tag{2.84}$$

Written in compact form the equations become:

$$\frac{\vec{\tau^B}}{\rho} = C_D|\vec{V}|\vec{V} \ , \tag{2.85}$$

where $\vec{V}$ is the average flow velocity. Provided that the surface stress (wind speed) is specified as a function of x, y and t, then the three equations (2.80), (2.81) and (2.82) form a closed set with three unknowns, H, M and N. For the rigid lid model, the equation of continuity became:

$$\frac{\partial M}{\partial x} + \frac{\partial N}{\partial y} = 0 \ . \tag{2.86}$$

Defining the stream function, ψ, and setting $M = -\frac{\partial \psi}{\partial y}$ and $N = -\frac{\partial \psi}{\partial x}$, the two momentum equations were combined into one, scalar, equation:

$$\begin{gathered} \frac{\partial}{\partial t}(\bigtriangledown \bullet D^{-1} \bigtriangledown \psi) + fJ(\psi, D^{-1}) = \\ \\ \frac{\partial}{\partial x}(\frac{\tau_y^S - \tau_y^B}{\rho D}) - \frac{\partial}{\partial y}(\frac{\tau_x^S - \tau_x^B}{\rho D}) \end{gathered} \ , \tag{2.87}$$

where:

$$J(\psi, D^{-1}) = \frac{\partial \psi}{\partial x}\frac{\partial D^{-1}}{\partial y} - \frac{\partial \psi}{\partial y}\frac{\partial D^{-1}}{\partial x} \ . \tag{2.88}$$

Also:

$$u = -\frac{1}{D}\frac{\partial \psi}{\partial y} \tag{2.89}$$

and

$$v = \frac{1}{D}\frac{\partial \psi}{\partial x} \ , \tag{2.90}$$

where u and v are the x and y components of the vertically averaged velocity, respectively. The isolines of the stream function, ψ, were the streamlines, to which the velocity vector was tangent. In the model the stream function varied with time (unsteady flow). The transformation of the momentum equations to a scalar stream-function-equation, in addition to being computationally advantageous, readily provided numerical means of tracking the movement of particles/pollutants in the flow, as will be seen below [26]. The models used a finite difference explicit scheme to solve the equations, with 1.2km grid squares forming the grid that approximates Lake St. Clair.

In 1989 Schwab et al. [26] presented a study of the circulation in Lake St. Clair, where they applied the rigid lid model described above [25], and compared their results with observations. Furthermore, a second model was used to track the movement of partially submerged particles in the lake. The importance of tracing and predicting the trajectories of particles lies, primarily, in being able to monitor and predict the movement of pollutants in the lake. A 1.2km characteristic-length-grid was constructed to approximate the geometry of the lake, as can be seen in Figure 2.39.

The model was driven by the hydraulic flow through the lake and by time-dependent wind stress at the surface. Wind stress was derived from hourly observations of wind speed and direction, air temperature and water temperature. The

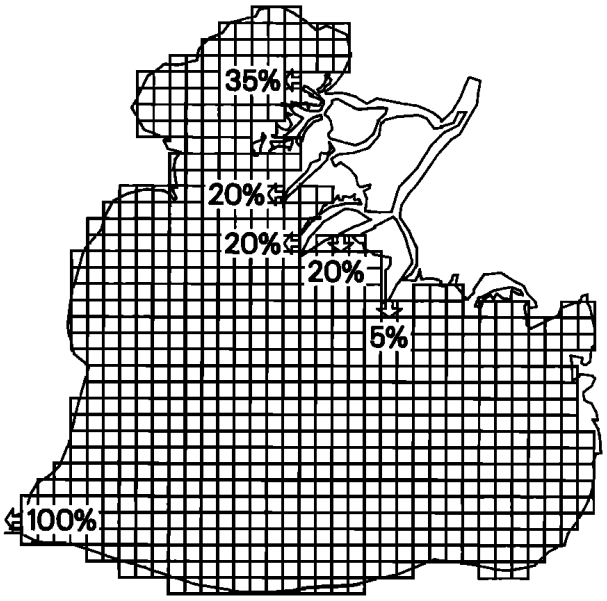

Figure 2.39: Numerical grid of Lake St. Clair [26]

wind drag coefficient varied with wind speed and temperatures of the air and the water. The particle trajectory model was implemented in the Pathfinder trajectory prediction system, used by the National Weather Service and the U.S. Coast Guard for tracking hazardous spills, as well as in rescue missions. The model used the equations of motion for a partially submerged drifting object:

$$\frac{dx}{dt} = u(x, y, t) = u_e(x, y, t) + a u_w(x, y, t) \tag{2.91}$$

and

$$\frac{dy}{dt} = v(x, y, t) = v_e(x, y, t) + a v_w(x, y, t) \ , \tag{2.92}$$

where u_e and v_e are components of the current velocity and u_w and v_w are wind

velocity components. The constant a represents a "windage" factor, that varies from zero for fully submerged objects to several percentage points for objects with over-the-surface exposure. The model used a highly accurate second order finite difference scheme. A limitation of the rigid lid model was that it did not account for vertical movements. As for the particle trajectory movement, a limitation was that it did not account for any diffusion or mixing at a sub-grid level. The 2D flow approximation was considered reasonable because of the shallowness of Lake St. Clair. There were difficulties in calculating the bottom friction coefficient for use in the circulation model. However, there was overall good agreement between computed results and observations for the drifter trajectories.

In 1985 Ibrahim and McCorquodale [28] presented a 3D steady state, finite element model, intended to study the circulation, as affected by wind and ice conditions, in Lake St. Clair. Their model's main objective was to generate representative flow patterns affected by wind, and to simulate the movement of pollutants. The authors made several assumptions in formulating the governing equations; stratification was neglected, horizontal momentum transfer was neglected, wind was assumed uniform over the lake and the time needed to attain steady state was short; furthermore, non-linear inertial terms were neglected. This assumption was based on certain computational results, which showed that the inclusion of the non-linear terms changed the values of velocities by only 3%. Finally, a constant eddy viscosity was assumed. The x, y and z momentum equations then became respectively:

$$-fv = -\frac{1}{\rho}\frac{\partial p}{\partial x} + \epsilon_z \frac{\partial^2 u}{\partial z^2} \ , \tag{2.93}$$

$$fu = -\frac{1}{\rho}\frac{\partial p}{\partial y} + \epsilon_z \frac{\partial^2 v}{\partial z^2} \tag{2.94}$$

and

$$g = -\frac{1}{\rho}\frac{\partial p}{\partial z} \ , \tag{2.95}$$

where p is (hydrostatic) pressure, ρ is the density of water and f is the Coriolis coefficient. g is the acceleration of gravity and ϵ_z is the turbulent viscosity. Continuity gave:

$$\frac{\partial u}{\partial x} + \frac{\partial v}{\partial y} + \frac{\partial w}{\partial z} = 0 \ , \tag{2.96}$$

where u, v and w are x, y and z velocities. The surface boundary conditions were:

$$\epsilon_z \frac{\partial u}{\partial z} = \tau_{sx} \tag{2.97}$$

and

$$\epsilon_z \frac{\partial v}{\partial z} = \tau_{sy} \ , \tag{2.98}$$

where τ_{sx} and τ_{sy} are wind stress functions in the x and y directions. For the wind stress function, equation (2.85) was used. Furthermore, a transport model was used for the simulation of pollutant circulation, based on a depth averaged transport

equation:

$$U\frac{\partial c}{\partial x}+V\frac{\partial c}{\partial y}=\frac{1}{h}\frac{\partial}{\partial x}(hE_x\frac{\partial c}{\partial x})+\frac{1}{h}\frac{\partial}{\partial y}(hE_y\frac{\partial c}{\partial y})- \\ \frac{E_x}{h}\frac{\partial c}{\partial x}\frac{\partial h}{\partial x}-\frac{E_y}{h}\frac{\partial c}{\partial y}\frac{\partial h}{\partial y}+kc+Q\ , \tag{2.99}$$

where c is the depth-averaged pollutant concentration, Q is a source/sink term and k is a reaction coefficient; E_x and E_y are turbulent eddy diffusivities in the x and y directions, h is depth and U and V are depth averaged velocities in the x and y directions. The flow and transport equations were solved by a finite element scheme. The model was calibrated by adjusting eddy viscosities. Good simulation of current magnitudes and fair prediction of current directions resulted. The model was also tested for an ice-covered-lake scenario, by setting wind stresses to zero and adding friction with ice on the top.

In 1989, Simons and Schertzer [29] presented a 2D unsteady model based on the linearized vertically integrated equations of motion. The model used a finite difference scheme, and the objective was to compute water levels as a function of wind stresses. The model was verified by correlating hourly values of computed and measured water levels, and a correlation coefficient of 0.92 was found for 1753 hourly values. The model was found to be very sensitive to the formulation of the bottom stress. Since the bottom stress was formulated first, and then the model was calibrated by adjusting the drag coefficient for wind stress, it was concluded that, from a computational perspective, the wind stress formulation depended heavily on the bottom stress formulation.

2.3.3 Combined-System Hydrodynamic Models

Holtschlag and Koschik [30] presented in 2002 a steady-state, 2D, finite element model for the HEC. The model was based on the RMA2 model developed by Tsanis et al. [27], presented above. The equations solved were the 2D depth-averaged RANS equations and continuity, that have been presented above in (2.70), (2.71) and (2.72). In the implementation of the RMA2 model, the Coriolis force, as well as wind effects, were excluded. For the bed shear, Manning's formula was used. The equations were solved by the Galerkin method of weighted residuals, that led to a system of nonlinear equations, solved by the Newton-Raphson method. The mesh comprised of triangular and quadrilateral elements, containing a total of 42,936 nodes. Calibration parameters were the Manning's coefficient, n, and the turbulent viscosities. The model was initiated with a given n value. Then 25 material zones with different Manning's coefficients were used, which were estimated based on seven scenarios/comparisons. A universal inverse modeling code was used to make the required adjustments, based on a nonlinear regression procedure. During the calibration procedure, the eddy viscosities were assigned values based on an assigned Peclet number. The boundary conditions were the flow velocity at the entrance of St. Clair River and the water level at the outflow of the Detroit River in Lake Erie. Outputs were flow velocities and water surface elevations. Overall, there was good agreement between simulated and expected results, as seen in figures 2.40 and 2.41.

In 2010, Anderson et al. [32] presented the first fully 3D, unsteady, hydrostatic, model, as applied to the HEC, that was based on the Finite Volume Coastal Ocean Model (FVCOM), developed by Chen et al. [31]. The equations on which the model was based are shown below; Continuity:

$$\bigtriangledown \bullet \vec{V} = 0 \ . \tag{2.100}$$

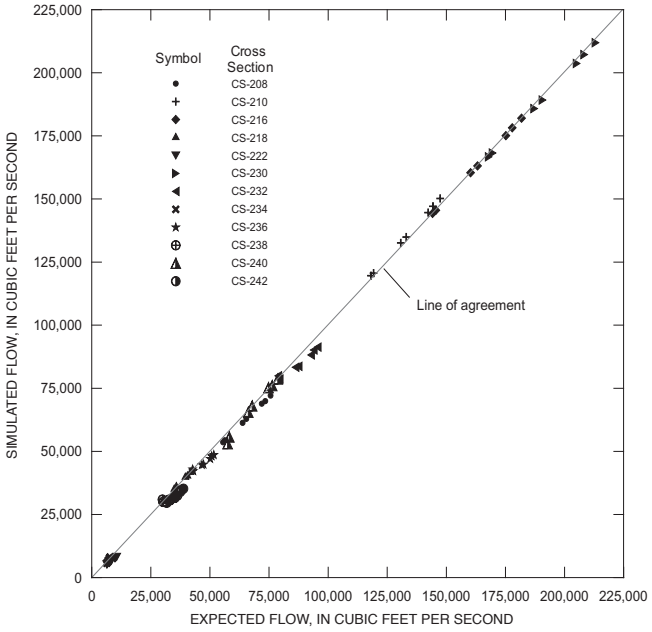

Figure 2.40: Comparison of simulated and expected flows [30]

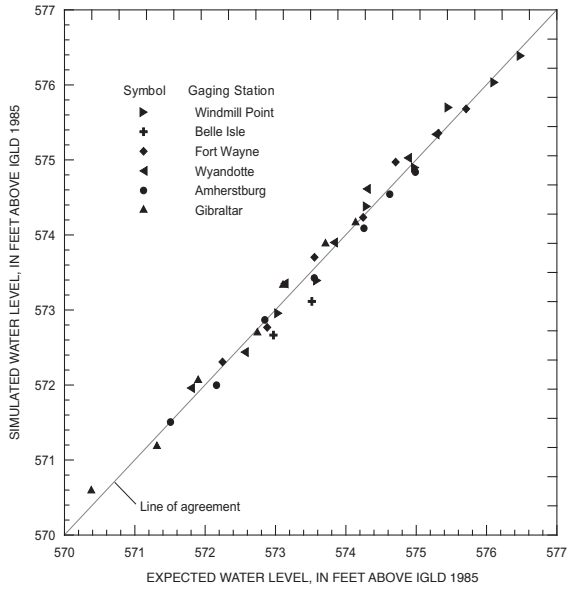

Figure 2.41: Comparison of simulated and expected water levels [30]

X-momentum:

$$\frac{Du}{Dt} - fv = -\frac{1}{\rho}\frac{\partial P}{\partial x} + \frac{\partial}{\partial z}(K_m \frac{\partial u}{\partial z}) + F_u \ . \tag{2.101}$$

Y-momentum:

$$\frac{Dv}{Dt} - fu = -\frac{1}{\rho}\frac{\partial P}{\partial y} + \frac{\partial}{\partial z}(K_m \frac{\partial v}{\partial z}) + F_v \tag{2.102}$$

and z-momentum:

$$\frac{\partial P}{\partial z} = -\rho g \ , \tag{2.103}$$

where $\vec{V}$ is the velocity vector and u and v are its components. f is the Coriolis parameter, ρ is the density of water and P is pressure; K_m is the vertical eddy viscosity and F_u and F_v are horizontal momentum diffusion terms. The model used a turbulent kinetic energy closure scheme. The boundary conditions were:

$$K_m \frac{\partial (u/v)}{\partial z} = \frac{1}{\rho}\tau_{x/y} \ , \tag{2.104}$$

where $\tau_{x/y}$ is the bottom (or surface) shear in the x/y directions, given by:

$$\frac{\tau_{x/y}}{\rho} = C_D \sqrt{u^2 + v^2}(u/v) \ , \tag{2.105}$$

where C_D is the drag coefficient, and u/v can be either the surface wind velocity components, or flow velocity components. An unstructured grid consisting of triangular elements was used, and a finite volume scheme was employed. The boundary conditions were the water levels at Lake Huron and Lake Erie, driving winds at Lake St. Clair, and water inflow from tributaries. The initial conditions in the model cor-

responded to a steady state. The steady state was achieved in the following manner: the system began with a flat water surface. Then the water was allowed to drain at the exit of the Detroit River into Lake Erie, until a surface elevation difference between 1.5 and 2 meters developed between Lake Huron and Lake Erie, which served as an initial condition. Bed roughness was taken to vary between different zones, and the model was calibrated based on the procedure followed by Holtschlag et al. [30]. Initially the model was calibrated (based on roughness values), with respect to water surface elevations at various locations. Once good agreement was achieved between measured and simulated water level values by changing individual roughness values, the model was calibrated with respect to flows by increasing or decreasing all roughness values simultaneously. Good agreement between expected values and simulated results was achieved, with the maximum difference in water level being approximately 4 cm and for most locations being less than 2 cm. Flows at the head of the St. Clair River were within 5% of measured values. The model was designed to provide both nowcasts and forecasts. Nowcasts were based on real-time (every six minutes) water level measurements, hourly figures for wind conditions in Lake St. Clair, and daily averages for tributary flows. 48h forecasts were based on wind and water level forecasts. Forecasts were updated every 12 hours, based on the newest measurements. As would be expected, the more time elapsed from the last forecast, the less accurate that forecast was. The limiting factor was the accuracy of the weather forecasts.

2.3.3.1 Other Models Currently in Use

The HEC-RAS model computes water surface profiles for one-dimensional steady, gradually varied flow in rivers of any cross section, and was developed by the US Army Corps of Engineers.

The TELEMAC-2D is a model that uses the finite element method to solve the depth averaged equations of flow (shallow water equations).

The HydroSed2D model solves the depth averaged equations of flow, but also incorporates sediment transport.

All three models were used in the International Joint Commission Report [1], briefly described in the introduction.

CHAPTER III

The Hydrodynamic Model

As seen from the study of previous models, a fully 3D turbulent, unsteady, non-hydrostatic model had not been implemented on any of the parts of the Huron Erie Corridor until now. This is precisely the type of model that is used in this work. The hydrostatic model is based on the work by Fringer et al [40], which solves the RANS equations on an unstructured grid using the finite volume method. The unstructured triangular grid is capable of capturing complex geometries. The model is the basis of the Suntans project (Stanford Unstructured Nonhydrostatic Terrain-following Adaptive Navier-Stokes Simulator), that is widely used in oceanographic studies. It has scalar transport capabilities and can account for surface winds. The Suntans platform readily allows for the unix-based code to run on multiple processors. The non-hydrostatic solver is based on the predictor-corrector method originally developed by Casulli [41].

3.0.4 A description of the equations

The conservative form of the Reynolds-Averaged Navier-Stokes equations for momentum are:

$$\frac{\partial u}{\partial t} + \bigtriangledown \bullet (\vec{u}u) - fv + bw = -\frac{1}{\rho_o}\frac{\partial p}{\partial x} + \bigtriangledown_H \bullet (\nu_H \bigtriangledown_H u) + \frac{\partial}{\partial z}(\nu_V \frac{\partial u}{\partial z}) \ , \tag{3.1}$$

$$\frac{\partial v}{\partial t} + \bigtriangledown \bullet (\vec{u}v) + fu = -\frac{1}{\rho_o}\frac{\partial p}{\partial y} + \bigtriangledown_H \bullet (\nu_H \bigtriangledown_H v) + \frac{\partial}{\partial z}(\nu_V \frac{\partial v}{\partial z}) \tag{3.2}$$

and

$$\frac{\partial w}{\partial t} + \bigtriangledown \bullet (\vec{u}w) - bu = -\frac{1}{\rho_o}\frac{\partial p}{\partial z} + \bigtriangledown_H \bullet (\nu_H \bigtriangledown_H w) + \frac{\partial}{\partial z}(\nu_V \frac{\partial w}{\partial z}) - \frac{g}{\rho_o}(\rho_o + \rho) \ . \tag{3.3}$$

Continuity leads to the incompressibility constraint:

$$\bigtriangledown \bullet \vec{u} = 0 \ , \tag{3.4}$$

where u, v and w are x, y and z velocity components, respectively. ρ_o is a constant reference density and ρ is the density variation, while the total density is given by $\rho_o + \rho$, f and b are Coriolis terms, and ν_H and ν_V are the horizontal and vertical eddy viscosities respectively. p is the total pressure. We also note that $\bigtriangledown_H$ stands for the horizontal gradient operator:

$$\bigtriangledown_H = \mathbf{e_x}\frac{\partial}{\partial x} + \mathbf{e_y}\frac{\partial}{\partial y} \ . \tag{3.5}$$

The pressure, p, is broken into hydrostatic, p_h, and nonhydrostatic, q, components,

such that $p = p_h + q$, with the hydrostatic pressure defined by:

$$\frac{\partial p_h}{\partial z} = -(\rho_o + \rho)g \ . \tag{3.6}$$

In this work density and other scalar gradients (temperature and salinity) were neglected, since flow in the St. Clair River is vigorously mixed. Dropping the density gradient and Coriolis terms, and neglecting atmospheric pressure variations, gives:

$$\frac{\partial u}{\partial t} + \bigtriangledown \bullet (\vec{u}u) = -\frac{1}{\rho_o}\frac{\partial q}{\partial x} - g\frac{\partial h}{\partial x} + \bigtriangledown_H \bullet (\nu_H \bigtriangledown_H u) + \frac{\partial}{\partial z}(\nu_V \frac{\partial u}{\partial z}) \ , \tag{3.7}$$

$$\frac{\partial v}{\partial t} + \bigtriangledown \bullet (\vec{u}v) = -\frac{1}{\rho_o}\frac{\partial q}{\partial y} - g\frac{\partial h}{\partial y} + \bigtriangledown_H \bullet (\nu_H \bigtriangledown_H v) + \frac{\partial}{\partial z}(\nu_V \frac{\partial v}{\partial z}) \tag{3.8}$$

and

$$\frac{\partial w}{\partial t} + \bigtriangledown \bullet (\vec{u}w) = -\frac{1}{\rho_o}\frac{\partial q}{\partial z} + \bigtriangledown_H \bullet (\nu_H \bigtriangledown_H w) + \frac{\partial}{\partial z}(\nu_V \frac{\partial w}{\partial z}) \ , \tag{3.9}$$

where h is the free surface elevation. Integrating the continuity equation (3.4) from the bottom, $z = -d(x, y)$ to the free surface, $z = h(x, y, t)$, gives the depth-integrated continuity equation:

$$\frac{\partial h}{\partial t} + \frac{\partial}{\partial x}(\int_{-d}^{h} u \, \mathrm{d}z) + \frac{\partial}{\partial y}(\int_{-d}^{h} v \, \mathrm{d}z) = 0 \ , \tag{3.10}$$

The following kinematic boundary conditions have been employed at z=h and

z=-d:

$$\frac{\partial h}{\partial t} + \mathbf{u_H}|_{z=h} \bullet \bigtriangledown_H h = w|_{z=h} \tag{3.11}$$

and

$$-\mathbf{u_H}|_{z=-d} \bullet \bigtriangledown_H d = w|_{z=-d} \ , \tag{3.12}$$

where $\mathbf{u_H} = u\mathbf{e_x} + v\mathbf{e_y}$ is the horizontal velocity vector. Equations (3.4), (3.7), (3.8), (3.9) and (3.10) comprise a set of equations for the flow velocity components, u, v and w, the free surface elevation , h, and the non-hydrostatic pressure, q.

3.0.5 The turbulence model

Suntans uses the Mellor and Yamada 2.5 turbulence closure model. The model rests on the assumption that horizontal turbulence transport is negligible with the resolved horizontal scale, which is much larger than the vertical. The only Reynolds stresses that remain then are $\overline{u'w'}$ and $\overline{v'w'}$. In accordance to the Boussinesq hypothesis:

$$-\overline{u'w'} = \nu_V \frac{\partial u}{\partial z} \tag{3.13}$$

and

$$-\overline{v'w'} = \nu_V \frac{\partial v}{\partial z} \ , \tag{3.14}$$

where v', u' and w' are velocity fluctuations (u, v and w are average values). The vertical turbulence viscosity, ν_V, is given by:

$$-\nu_V = lqS_M \ , \tag{3.15}$$

where l is a length scale, q is the turbulent kinetic energy and S_M is a, so called, stability function given as an algebraic expression of the term G_M, where:

$$G_M = \frac{l^2}{q^2}[(\frac{\partial u}{\partial z})^2 + (\frac{\partial v}{\partial z})^2] \ . \tag{3.16}$$

The Mellor and Yamada model is a two-equation model, the two equations being prognostic equations for q and l. The equation that gives the evolution of q is:

$$\frac{D(q^2/2)}{Dt} - \frac{\partial}{\partial z}(lqS_q\frac{\partial}{\partial}(\frac{q^2}{2}) = P_s - \epsilon \ , \tag{3.17}$$

where S_q is a constant and ϵ is the turbulent kinetic energy dissipation rate with:

$$\epsilon = \frac{q^3}{B_1 l} \ . \tag{3.18}$$

B_1 is a constant. The term P_s is:

$$P_s = -\overline{u'w'}\frac{\partial u}{\partial z} - \overline{v'w'}\frac{\partial v}{\partial z} \ . \tag{3.19}$$

The prognostic equation for l is:

$$\frac{D}{Dt}(q^2 l) - \frac{\partial}{\partial z}[qlS_l \frac{\partial}{\partial z}(q^2 l)] = lE_1 P_s - \frac{q^3}{B_1}[1 + E_2(\frac{l}{\kappa L})^2] \; . \tag{3.20}$$

In the equation above S_l, E_1 and E_2 are constants and κ is the Von Karman constant. L is a distance from the wall. The given set of equations provides a closure scheme from which the vertical eddy viscosity can be computed. In the model a constant value is given for the horizontal viscosity, for stability purposes.

3.0.6 The grid

The grid is first constructed by two-dimensional Delaunay triangulation and is completed in the third dimension by stacking elements horizontally in the z-direction. The circumcircle of each triangle is formed by the Delaunay points at the vertices, and each pair forms a Delaunay edge. The Voronoi points are the centers of the circumcircles. The grid is constructed in such a way that no triangle lies in the circumcircle of another triangle, but the Voronoi point of a triangle might do so. Furthermore, the edges that connect the Voronoi points of neighboring triangles, the Voronoi edges, are perpendicular to the faces of the Delaunay triangles (Delaunay edges) shared by those triangles, thus forming an orthogonal unstructured grid. A schematic of the description above can be seen in Figure 3.1. In theory the grid is meant to be orthogonal, that is the lines connecting the Voronoi points of neighboring triangles are perpendicular to the edges shared by the triangles. However, the meshing software used in this work – Gambit – did not guarantee such a condition, and additional numerical error, with potential for instabilities, was introduced.

The model employs a staggered grid. All scalars (eddy viscosity, diffusivities, temperature, salinity etc, as well as pressure) are defined at the centers of cells. The horizontal velocities, U, are defined normal to each vertical cell face, at the intersection

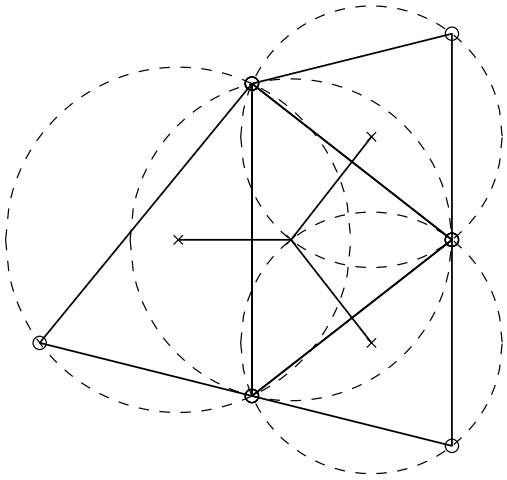

Figure 3.1: Schematic of the implemented Delaunay triangulation; the Delaunay points are denoted by '-o-' ,the circumcircles are denoted by '- -', and the Voronoi points by '+' [40]

of the Delaunay and Voronoi edges. The vertical velocities, w, are defined at the Voronoi points at the top and bottom of cells. Figure 3.2 shows this description.

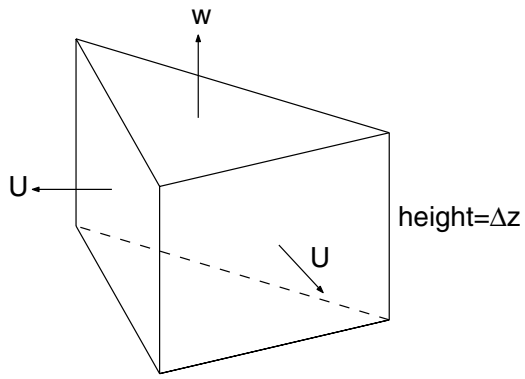

Figure 3.2: Description of a 3D prismatic grid cell [40]

3.0.7 Numerical discretization

The horizontal momentum equations are solved at the vertical faces of each cell, by taking the dot product of the face-normal vector, **n** with the horizontal momentum equations (3.7) and (3.8):

$$\frac{\partial U}{\partial t} + \mathbf{n} \bullet \bigtriangledown \bullet (\mathbf{uu}) = -\frac{1}{\rho_o}\frac{\partial q}{\partial n} - g\frac{\partial h}{\partial n} + \bigtriangledown_H \bullet (\nu_H \bigtriangledown_H U) + \frac{\partial}{\partial z}(\nu_V \frac{\partial U}{\partial z}) \ , \qquad (3.21)$$

where $\frac{\partial}{\partial n}$ is the face-normal gradient and $\mathbf{u}$ is the horizontal velocity vector. The vertical momentum equation is given by:

$$\frac{\partial w}{\partial t} + \bigtriangledown \bullet (\mathbf{u}w) = -\frac{1}{\rho_o}\frac{\partial q}{\partial z} + \bigtriangledown_H \bullet (\nu_H \bigtriangledown_H w) + \frac{\partial}{\partial z}(\nu_V \frac{\partial w}{\partial z}) \ . \qquad (3.22)$$

Based on the old non-hydrostatic pressure at the previous time step, a velocity at edge number j and grid level k at the next time step, $n+1$, is computed from:

$$\frac{U_{j,k}^{n+1} - U_{j,k}^{n}}{\Delta t} = \frac{1}{2}(3F_{j,k}^{n} - F_{j,k}^{n-1}) - \frac{1}{\rho_o}\frac{\partial q^{n-\frac{1}{2}}}{\partial n} - g\theta\frac{\partial h}{\partial n}\bigg|_j^{n+1} - g(1-\theta)\frac{\partial h}{\partial n}\bigg|_j^{n}$$

$$+\theta\frac{\partial}{\partial z}(\nu_V^n \frac{\partial U_{j,k}^{n+1}}{\partial z}) + (1-\theta)\frac{\partial}{\partial z}(\nu_V^n \frac{\partial U_{j,k}^{n}}{\partial z}) \qquad (3.23)$$

and a vertical velocity at cell number i and vertical level k is computed from:

$$\frac{w_{i,k}^{n+1} - w_{i,k}^{n}}{\Delta t} = \frac{1}{2}(3H_{j,k}^{n} - H_{j,k}^{n-1}) - \frac{1}{\rho_o}\frac{\partial q^{n-\frac{1}{2}}}{\partial z} + \theta\frac{\partial}{\partial z}(\nu_V^n \frac{\partial w_{i,k}^{n+1}}{\partial z}) + (1-\theta)\frac{\partial}{\partial z}(\nu_V^n \frac{\partial w_{i,k}^{n}}{\partial z}) \qquad (3.24)$$

The vertical diffusion and free surface terms have been discretized semi-implicitly with the theta method. The explicit terms are discretized with the second order Adams-Bashforth method as:

$$F_{j,k} = -C_H(U_{j,k}) - C_V(U_{j,k}) + D_H(U_{j,k}) \tag{3.25}$$

and

$$H_{j,k} = -C_H(w_{j,k}) - C_V(w_{j,k}) + D_H(w_{j,k}) \ , \tag{3.26}$$

where $C_H()$, $C_V()$ and $D_H()$ are horizontal and vertical advection and horizontal diffusion operators, respectively. Boundary conditions for the horizontal velocity at the bed are given by the drag law:

$$\nu_V \frac{\partial U}{\partial z}\bigg|_{z=h} = C_{d,B}|U|U \ , \tag{3.27}$$

Where $C_{d,B}$ is the bed drag coefficient, more about which will be said below. In the original model numerical values were directly given to the bed drag coefficient. As part of this work, a bed particle size distribution is provided and from there drag coefficients are computed. At the free surface, a drag law with wind stress can be imposed, but in this work wind-induced drag was not considered, so the upper-boundary boundary condition was zero traction. In vector form, the depth-integrated continuity equation is given by:

$$\frac{\partial h}{\partial t} + \bigtriangledown_H \bullet \int_{-d}^{h} \mathbf{u}_H \, \mathrm{d}z = 0 \ , \tag{3.28}$$

which is discretized as:

$$\frac{h_i^{n+1} - h_i^n}{\Delta t} + \frac{1}{A_i}\theta \sum_{m=1}^{N_s}\sum_{k=1}^{N_{ke}} U_{m,k}^{n+1}\Delta z_{i,k} N_m df_m + \frac{1}{A_i}(1-\theta)\sum_{m=1}^{N_s}\sum_{k=1}^{N_{ke}} U_{m,k}^{n}\Delta z_{i,k}^{uw} N_m df_m = 0 \ , \tag{3.29}$$

where A_i – in the horizontal plane –is the area of the cell i with N_s sides and at which the free surface height is h_i. N_{ke} is the number of levels in the vertical direction at side m, and df_m is the length of the $m-th$ side of the cell triangle. $U_{m,k}$ is the normal component of the velocity at the $m-th$ side at the $k-th$ depth level. $\Delta z_{i,k}$ is the height of cell i at level k. Equation (3.29) gives the free surface at the next time step, $n+1$. The way the scheme works is to first replace the horizontal velocity at time step $n+1$ in the horizontal momentum equation (3.23), U^{n+1}, with a predicted velocity, U^*. In the free-surface equation (3.29) the predicted horizontal velocity, U^*, is used instead of the one at the next time step, without loss of much accuracy. Then, the horizontal momentum equation (3.23) and the free surface equation (3.29) have two unknowns, h^{n+1} and U^*. The two variables can be computed by first substituting for the free surface height in the momentum equation and solving for the predicted horizontal velocities and then going back to the free surface equation to find the free surface elevations at the next time step. The predicted vertical velocity, w^*, can be readily computed from previous step values. The horizontal and vertical predicted velocities, U^* and w^*, are adjusted after a non-hydrostatic pressure correction term is computed.

3.0.7.1 Nonhydrostatic pressure

The predicted velocity field, U^* and w^*, was derived by means of depth-integrating the continuity equation. As such, it does not satisfy local continuity. To correct this, a non-hydrostatic pressure field that forces local continuity is computed. This is

done by correcting the horizontal and vertical velocity fields with a non-hydrostatic pressure correction term, qc, as follows:

$$U_{j,k}^{n+1} = U_{j,k}^{*} - \Delta t(\frac{qc_{G_{2j},k} - qc_{G_{2j+1},k}}{D_j}) \tag{3.30}$$

and

$$w_{i,k}^{n+1} = w_{i,k}^{*} - 2\Delta t(\frac{qc_{i,k} - qc_{i,k-1}}{\Delta z_{i,k} + \Delta z_{i,k-1}}) \ , \tag{3.31}$$

where j is a face index, k is a level index and i is a cell index. The indices G_{2j} and G_{2j+1} refer to neighboring cells and D_j is the distance between the Voronoi points of neighboring cells. The continuity equation is integrated over a cell with N_s sides, to give:

$$A_i(w_{i,k+1}^{n+1} - w_{i,k}^{n+1}) + \sum_{m=1}^{N_s} U_{m,k}^{n+1} \Delta z_{m,k} df_m = 0 \tag{3.32}$$

The velocities at the next time step, U^{n+1} and w^{n+1}, in equation (3.32) are substituted for the pressure-corrected velocities of equations (3.30) and (3.31) to give a Poisson equation to be solved for the pressure correction terms. Once the pressure correction terms are determined, the predicted flow field is updated to the flow field at the next time step, and the pressure field is also updated to find the new pressure field.

3.0.8 Concluding remarks on the hydrodynamic model

A few significant points need to be addressed about the hydrodynamic model (suntans). The semi-implicit treatment of vertical diffusion terms in the momentum equations provides stability at relatively large time steps, even when there is a high degree of vertical grid refinement, provided horizontal grid scales remain large enough. This makes the model suitable for use in geometries where vertical length scales are much smaller than horizontal. Another characteristic of the model is that the way the free surface movements are tacked is by extending or shortening the cells in the top layer of the grid; cells are not added or subtracted from the top layer as the free surface moves. This can make the model unstable when dealing with high free surface fluctuations, because if the free surface drops at or below the height of the top cell, the vertical Courant number goes to infinity and the code becomes unstable. On the other hand, if the height of the top cell is too big, the flow field will not be properly resolved. This is a weakness of the model and was of significance in the validation case for the bedload transport model. With respect to stability, the time step used is proportional to the square of the horizontal length scale. When horizontal grid refinement doubles, without changing the vertical refinement, the time step has to be divided by a factor of 4. Computation time increases then by a factor of 8 (since the number of cells doubles). This makes the model unsuitable for use in small-scale geometries, since the time steps involved prohibit reasonable simulation run times. The reason(s) for the discrepancy between theoretical and practical stability limits is not clear. Another characteristic of the model is that approximately 90% of computational time is taken up by the non-hydrostatic pressure solver. The solver uses an iterative procedure which is computationally intensive.

CHAPTER IV

Modeling Bedload Transport

4.1 Previous Work on Sediment Transport Models

The first fluid-dynamical computational models with sediment transport capabilities appeared in the 80's. The first fully 3D models were developed starting 2000, the first by Wu et al [42] in 2000 to model scouring in a channel with a 180^o turn. It employed the finite volume method in a non-staggered adaptive grid to solve the RANS equations with a two-equation $(k-\epsilon)$ closure scheme. The position of the free surface was computed by depth integrating the x and y momentum equations, presented below:

$$\frac{\partial U}{\partial t} + U\frac{\partial U}{\partial x} + V\frac{\partial U}{\partial y} = -g\frac{\partial z_s}{\partial x} + \frac{1}{\rho}\frac{\partial T_{xx}}{\partial x} + \frac{1}{\rho}\frac{\partial T_{xy}}{\partial y} - \frac{1}{\rho h}\tau_{xb} \tag{4.1}$$

and

$$\frac{\partial V}{\partial t} + U\frac{\partial V}{\partial x} + V\frac{\partial V}{\partial y} = -g\frac{\partial z_s}{\partial y} + \frac{1}{\rho}\frac{\partial T_{xy}}{\partial x} + \frac{1}{\rho}\frac{\partial T_{yy}}{\partial y} - \frac{1}{\rho h}\tau_{yb}\ , \tag{4.2}$$

where V and U are average flow velocities, z_s is the coordinate of the free surface,

T_{xx} and T_{xy} are averaged stresses, τ_{xb} and τ_{yb} are stresses on the bed. h here is the water depth. Differentiating the x-momentum equation with respect to x and y-momentum with respect to y and combining the two equations leads to a Poisson equation in z_s:

$$\frac{\partial^2 z_s}{\partial x^2} + \frac{\partial^2 z_s}{\partial y^2} = \frac{Q}{g} \,, \tag{4.3}$$

where Q contains the re-arranged terms from the differentiated equations, from the previous time step. The depth-integrating process implied hydrostatic pressure distribution, so the model assumed only gradually varied flow. This was a weakness of the model, since flow around bends is non-hydrostatic due to the centripetal acceleration, and is characterized by secondary transverse flows, which are the ones that cause scouring. The scouring in channel bends is primarily in the transverse direction due to the secondary flows that tend to move material from the outer bank to the inner bank. These currents are plotted in figure 4.6. All hydrodynamic models that were developed after the work by We et al [42] that employed scouring solved the non-hydrostatic RANS equations. This is a necessity for accurate simulations of flow in channels with bends, as well as flow around obstacles which involves decelerations.

Both entrained and bedload sediment transport was employed by Wu et al in their model. Suspended sediment transport was modeled by solving a convection-diffusion equation with empirical pickup and deposition functions for the boundary between the bed and the flow field. Of interest is the bedload transport model. For the stresses on the bed a log law was employed, much like the one used as part of the work of this thesis, and which will be presented later. The median grain diameter, d_{50}, was used to calculated the bed roughness, which is commonly used to calculate the stresses on river beds. The bed load flux, q_b was computed from these stresses and the Exner

equation (mass balance) was solved to find the evolution of the bed:

$$(1-p)\frac{\partial z_b}{\partial t} + \frac{\partial q_{bx}}{\partial x} + \frac{\partial q_{by}}{\partial y} = 0 \ , \tag{4.4}$$

where z_b is the bed elevation, p is the sediment porosity and q_{bx} and q_{by} are the bed load fluxes in the x and y direction respectively, given by:

$$q_{bx} = \alpha_{bx} q_b, q_{by} = \alpha_{by} q_b \ , \tag{4.5}$$

where α_{bx} and α_{by} are direction cosines of the flow velocity vector. The angle of inclination of the bed and the component of the weight of the grains in that direction were not taken into account, since the direction cosines were those of the flow velocity near the bed. The results of the model were compared to those of the experiment by Odgaard and Bergs [43], of scouring in a channel with a 180^o bend and the agreement was good as seen in figure 4.1.

Nagata et al developed a fully 3D non-hydrostatic RANS solver model with bed-load transport capabilities [50]. The model used a finite volume scheme on a staggered Cartesian deformable grid. The grid deformed both following free surface movements and the moving bed. For the RANS solver, a $k-\epsilon$ model was used. To validate the model, the authors simulated flow around a spur dike and around a bridge pier in a channel, both frequently used hydraulic structures. Their results compared well with experimental data from Michiue et al for the case of the dike [51] and Melville [52], [53] for the case of the bridge pier. For the bed elevation, the following formula was used:

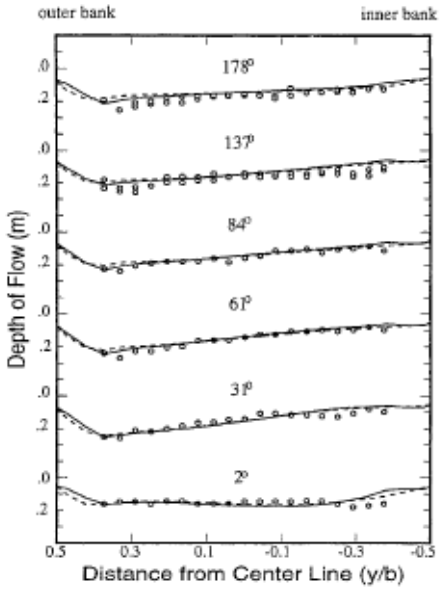

Figure 4.1: Scouring profiles in a channel: Experimental and numerical results compared [43]

$$\frac{\partial z_b}{\partial t} = \frac{A_1 A_2}{A_3} \frac{(V_d - V_p)}{S_p} \ , \tag{4.6}$$

where z_b is the bed elevation, A_1, A_2 and A_3 are shape coefficients for the sediment grains and S_p is the area of the projected bed surface on the horizontal plane. V_d is the sediment volume deposition rate and V_p is the sediment volume pickup rate.

For the sediment volume pickup rate, the following formula was used:

$$V_p = \frac{A_3 d_{50}}{A_2} p_s S_p \ . \tag{4.7}$$

d_{50} is the median sediment grain diameter, while the pickup rate, p_s, was a function of the dimensionless Shields stress,

$$\theta = \frac{u_*^2}{(s-1)gd_{50}} \ , \tag{4.8}$$

where s is the specific gravity of the sediment, g is the acceleration of gravity and u_* is the friction velocity, which is a measure of the flow induced stress on the bed, and which will be explained more later. It will suffice here to say that to calculate u_* the authors assumed a logarithmic velocity profile based on bed-roughness height equal to $2.5d_{50}$. The Shields stress gives the magnitude of the stress on the bed that induces sediment motion, relative to the immobilizing weight of the sediment particle. To calculate the velocity vector of a sediment particle, $\mathbf{u}_{sed}$, the authors solved a momentum equation, taking into account the local bed inclination, the angle between the particle velocity vector and the direction of maximum bed slope, as well as the angle between the particle velocity vector and the proximal flow vector. This approach is similar to the one followed by Roulund et al the same year [47] and will be presented later. The position of a sediment particle after being picked up at the next time step, n, was given by:

$$\mathbf{p}_{sed(n)} = \mathbf{p}_{sed(n-1)} + \Delta t \mathbf{u}_{sed} \ , \tag{4.9}$$

and the distance of sediment movement, $s_{(n)}$, was:

$$s_{(n)} = \sum \Delta t |\mathbf{u}_{sed}| \ . \tag{4.10}$$

To find the volume deposition rate of the sediment moving from point j at the time it reached the position $\mathbf{p}_{sed(n)}$ the authors used a stochastic approach:

$$V_{d(j,n)} = V_{p(j)} f_s(s_{(n)}) |\mathbf{u}_{sed(n)}| \Delta t \ , \tag{4.11}$$

where $V_{d(j,n)}$ is the volume deposition rate and $V_{p(j)}$ is the total volume flow rate of particles moving from point j. $f_s(s_{(n)})$ is a probability density function of step length, given by:

$$f_s(s_{(n)}) = \frac{1}{\lambda} e^{(-\frac{s_{(n)}}{\lambda})} \ , \tag{4.12}$$

where λ is the average step length. The originality of the approach followed by the authors was in calculating the sediment volume deposition rate by means of a stochastic approach, while at the same time solving a momentum equation to find individual sediment grain velocities.

At approximately the same time as Nagata et al [50] presented their model, Roulund et al [47] presented a model similar in some respects, that simulated scouring around a circular pile. The model was based on EllipSys3D, a RANS non-hydrostatic solver, that was originally developed at the Technical University of Denmark [54]. The solver used the finite volume method on a curvilinear deformable grid. The $k - \omega$ turbulence model was used. The authors conducted experiments and compared numerical and experimental results. Figure 4.2 shows a photo from one of the scouring experiments that the authors conducted.

The bedload transport model that was implemented is of particular interest, since part of the methodology used to calculate bedload fluxes was used in the model that is part of this thesis. Like in the model of Nagata et al [50], the velocity of a grain particle, $\mathbf{U}_b$, is assumed to be different from that of the flow field at the bed, $\mathbf{U}$. $\mathbf{U}$ is given as $\mathbf{U} = \alpha \mathbf{U}_f$, $\mathbf{U}_f$ being the friction velocity, calculated by assuming

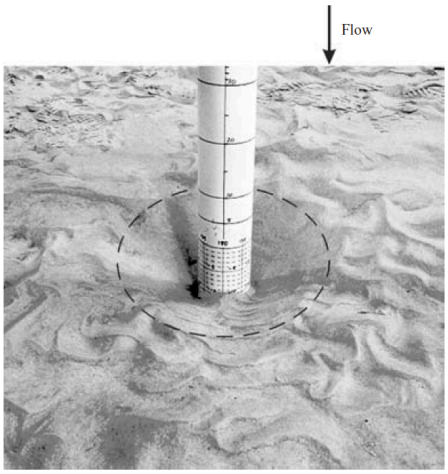

Figure 4.2: A photograph of scouring around a circular pile [47]

a logarithmic velocity profile (law of the wall), and α being a constant, following Engelund and Fredsoe [55], set equal to 10. The rate of bedload transport is given by:

$$\mathbf{q}_b = \frac{1}{6}\pi d^3 \frac{PEF}{d^2}\mathbf{U}_b \; . \tag{4.13}$$

Here $\mathbf{q}_b$ is the rate of bedload transport vector given as volume per unit time per unit length. d is the median grain diameter. PEF is the percentage of particles in motion in the surface layer of the bed, while $\mathbf{U}_b$ is the velocity of a bed particle. The parameters that have to be found in order to calculate the bedload rate of transport are PEF and $\mathbf{U}_b$. For the percentage of particles in motion the following formula is used from Engelund and Fredsoe [55]

$$PEF = [1 + (\frac{\frac{1}{6}\pi\mu_d}{\theta - \theta_c})^4]^{-1/4} \; , \tag{4.14}$$

where θ is the Shields stress, θ_c is the critical Shields stress and μ_d is the coefficient

of dynamic friction. If the Shields stress exceeds the critical Shields stress motion is initiated. The critical Shields stress depends on the local angle of inclination of the bed, β, as well as the angle that the flow velocity vector makes with the direction of maximum slope, α, and is given by:

$$\theta_c = \theta_{c0}(\cos\beta\sqrt{(1 - \frac{\sin^2\alpha\tan^2\beta}{\mu_s^2})} - \frac{\cos\alpha\sin\beta}{\mu_s}) \ , \tag{4.15}$$

where μ_s is the coefficient of static friction and θ_{c0} is the critical Shields stress for a flat bed, taken equal to 0.05. The forces on a sediment particle are the weight component:

$$W\sin\beta \ , \tag{4.16}$$

where W is the weight of a grain particle adjusted for buoyancy, given by:

$$W = \frac{1}{6}\pi\rho g(s-1)d^3 \ . \tag{4.17}$$

s is the submerged specific gravity, d is the grain diameter and ρ is the water density. The drag force, F_D, on the particle is given by

$$F_D = \frac{1}{2}\rho c\frac{\pi}{4}d^2U_r^2 \ , \tag{4.18}$$

where U_r is the flow velocity relative to the particle and c is a force coefficient given by Fredsoe and Deigaard [48] :

$$c = \frac{4\mu_s}{3a^2(\frac{1}{2}\theta_{c0})} \ . \tag{4.19}$$

The stabilizing force is friction, given by:

$$(W cos\beta)\mu_d \ . \tag{4.20}$$

Friction acts in the direction to oppose particle motion. Figure 4.3 shows schematically the kinematic and dynamic relations that govern the motion of a sediment particle.

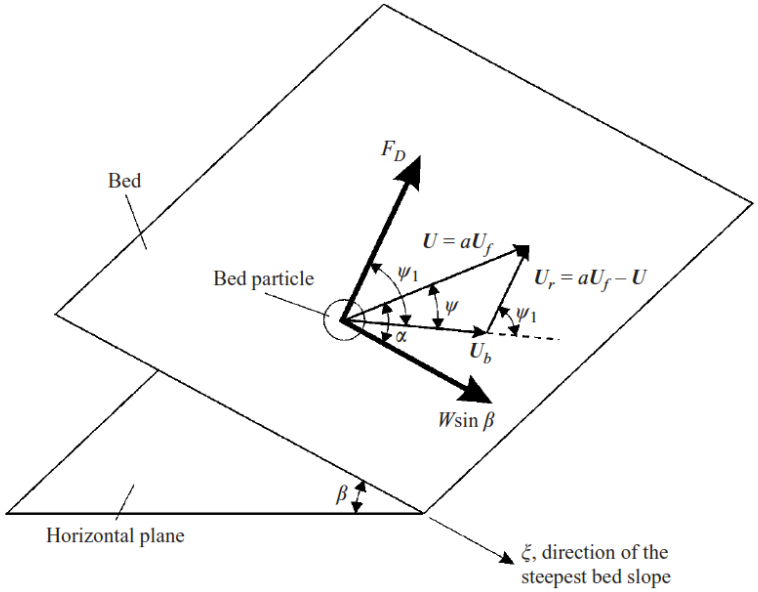

Figure 4.3: Kinematic and dynamic relations of the movement of a bed particle [47]

The kinematic relation that ties the relative-to-the-flow particle velocity to the flow velocity and the particle absolute velocity is expressed in vector form as:

$$\mathbf{U}_r = \alpha \mathbf{U}_f - \mathbf{U}_b \ , \tag{4.21}$$

where $\mathbf{U}_f$ is the friction velocity, $\mathbf{U}_r$ is the relative velocity and $\mathbf{U}_b$ is the absolute velocity of the bed particle. The relationship above can be expressed by two scalar equations, and referring to figure 4.3 they are:

$$U_r sin\Psi_1 - \alpha U_f sin\Psi = 0 \ , \tag{4.22}$$

and

$$U_r cos\Psi_1 - \alpha U_f cos\Psi + U_b = 0 \ , \tag{4.23}$$

where U_r, U_f and U_b are magnitudes. Force balance gives the following relations, expressed as algebraic equations, and referring to figure 4.3:

$$F_D cos\Psi_1 + W sin\beta cos(\alpha - \Psi) - (W cos\beta)\mu_d = 0 \ , \tag{4.24}$$

and

$$F_D sin\Psi_1 - W sin\beta sin(\alpha - \Psi) = 0 \ , \tag{4.25}$$

where F_D is the drag force induced by the relative flow velocity, W is the weight of the particle adjusted for buoyancy, and μ_d is the coefficient of dynamic friction. The

angles α, β, Ψ_1 and Ψ are depicted in figure 4.3. Equations (4.22) to (4.25) forms a system of four non-linear algebraic equations in four unknowns, namely U_r, U_b, Ψ_1 and Ψ. While the authors did not say what methodology they followed to solve the system, in the work of this thesis the Newton-Raphson algorithm is employed. Furthermore, while the solution gives the magnitude of $\mathbf{U}_b$ and not its x and y components, a second linear system in three unknowns is solved in this work. Once the velocity of a bed particle, $\mathbf{U}_b$, is calculated, and having found the Shields stress, θ, and in effect the percentage of particles in motion (4.14), the bedload flux vector, $\mathbf{q}_b$, is computed. Once the bedload fluxes are known the change in bed elevation is calculated by using the Exner equation (4.4), given below in integral form, after having applied the divergence theorem:

$$\frac{\partial h}{\partial t} = \frac{-1}{1-n}\frac{1}{A}\sum_{i=1}^{4}[(\mathbf{q}_{b,i} \bullet \mathbf{n}_i)|l_i|] \ , \tag{4.26}$$

where h is the bed elevation, n is the sediment porosity and A is the projected area of an element on the horizontal plane. $\mathbf{q}_{b,i}$ is the bedload flux vector through side i, $\mathbf{n}_i$ is the outward normal on side i and $|l_i|$ is the length of side i. Note that the fluxes are computed as volume flow rates per unit length, and, as such, the Exner equation is essentially a conservation of volume equation. The derivation of equation (4.26) and its use will be explained more later when describing the model developed in this thesis. The model by Roulund et al [47] includes a sandslide algorithm that goes into effect once the angle of inclination exceeds a critical angle, the angle of repose, dependent on the sediment type and size. In this case, the sediment particle velocity is aligned with the weight component in the direction of maximum slope, and is given by:

$$Wsin\beta - \mu_d Wcos\beta - \frac{1}{2}\rho C_D \frac{\pi}{4} d^2 U_b^2 = 0 \ , \tag{4.27}$$

where C_D is the particle drag coefficient. The model assumes that sand slides are instantaneous in time, and stop once the angle of repose is not exceeded. As part of this thesis, a modified sand slide algorithm is implemented that gives equivalent results. Below is a figure comparing experimental and numerical results of scouring around a circular pile.

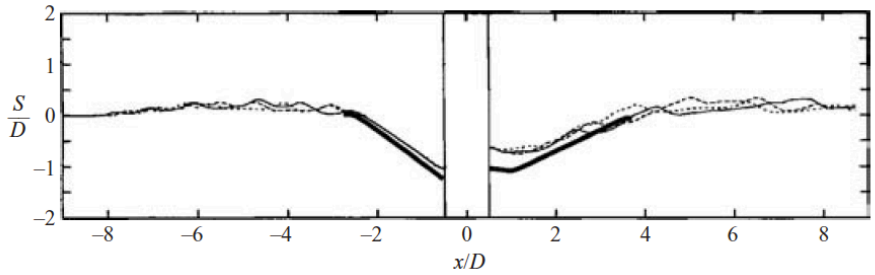

Figure 4.4: Comparison between experimental and numerical results; the thick line corresponds to the experiment after equilibrium is established. The continuous thin line corresponds to the simulation after equilibrium is achieved. The dashed lines correspond to scouring depths at different times before equilibrium [47]

The model that the authors developed slightly under-predicted the degree of scouring around a circular pile. The modeled upstream scour depth was approximately 15% less than the experimental, while the downstream depth was approximately 30% less. Nonetheless, the results were considered acceptable. It should be noted that for the scouring model the authors used a steady state hydrodynamic flow model, and that may have contributed to the discrepancies between experimental and numerical results. Furthermore the authors did not account for a free surface in their model, although the depth was enough to be able to ignore the free surface, at least in theory. Finally only one grain diameter size was used in both the experiment and the model.

Khosronejad et al [58] presented a numerical model for scouring in a 90^o channel bend. They compared their results with experimental data derived from experiments by Matsuura et al [59]. The hydrodynamic model used the finite volume method on a curvilinear deformable grid to solve the non-hydrostatic RANS equations. For closure the model used either a $k-\omega$ or a $k-\epsilon$ turbulence scheme. The authors implemented both suspended sediment transport by solving a convection-diffusion equation, as well as bedload transport. Of interest here is the latter. For calculation of the stresses on the bed a logarithmic velocity profile was assumed, allowing the use of a drag law. The Exner equation (sediment continuity equation) was used to update the bed elevation:

$$(1-\lambda)\frac{\partial z_b}{\partial t}+\frac{\partial q_{T\xi}}{\partial \xi}+\frac{\partial q_{T\zeta}}{\partial \zeta}=0\ , \tag{4.28}$$

where λ is the sediment porosity, z_b is the bed elevation, ξ and ζ are cuvilinear coordinates and $q_{T\xi}$ and $q_{T\zeta}$ are total fluxes, both of suspended sediment and of bed load. Of importance are the bedload fluxes, $q_{b\xi}$ and $q_{b\zeta}$, and the methodology that was followed in order to calculate them. For the magnitude of the bedload flux vector, $\mathbf{q}_b$, Van Rijn's bedload transport formula [60] was used:

$$q_b=0.053[\frac{\rho_s-\rho}{\rho}g]^{0.5}\frac{d_{50}^{1.5}T^{2.1}}{D_*^{0.3}}\ , \tag{4.29}$$

with

$$T=\frac{\tau_0-\tau_{cr}}{\tau_{cr}} \tag{4.30}$$

and

$$D_* = d_{50}[\frac{(\rho_s - \rho)g}{\nu^2}]^{1/3} \ , \tag{4.31}$$

where τ_0 is the bed shear stress, τ_{cr} is the critical bed shear stress for an inclined bed, ρ_s is the sediment density, ρ is the water density and ν is the kinematic viscosity of water. d_{50} is the median grain diameter and g is the acceleration of gravity. The critical shear stress, τ_{cr}, depends on the local angle of inclination, and the authors corrected for that. As for the bedload flux components, the following formulas were used by Duan et al [76], [62]:

$$q_{b\xi} = q_b(\frac{1}{\sqrt{1 + tan^2\gamma}}) \tag{4.32}$$

and

$$q_{b\zeta} = q_{b\xi}(tan\gamma + \frac{1 + \chi tan\phi}{\lambda_s tan\phi}\sqrt{\frac{\tau_{cr}}{\tau_0}}tan\beta_2) \ , \tag{4.33}$$

where χ and λ_s are constants, ϕ is the friction coefficient (the tangent of the angle of repose), β_2 is the transverse bed slope angle and γ is the deviation angle given by:

$$\gamma = arctan(\frac{w}{u}) - \theta_t \ , \tag{4.34}$$

where u and w are horizontal velocity components in the x and z directions respectively (the authors took the x-z plane as the horizontal plane), and θ_t is the angle

between the centerline and positive x-axis.

The authors simulated scouring in a 90 degree bend of a channel, following experiments by Matsuura [59]. Figure 4.5 presents a comparison between experimental and numerical results. As mentioned earlier, in a channel bend, due to the rapid accelerations to which the fluid is subjected, secondary, transverse, circular currents appear that tend to move bedload material towards the inner bank and scour the outer bank. The rapid accelerations necessitate the use of non-hydrostatic hydrodynamic models to simulate flows under such conditions. Figure 4.6 shows the streamlines of transverse sections on a channel bend, where the transverse currents are clearly visible.

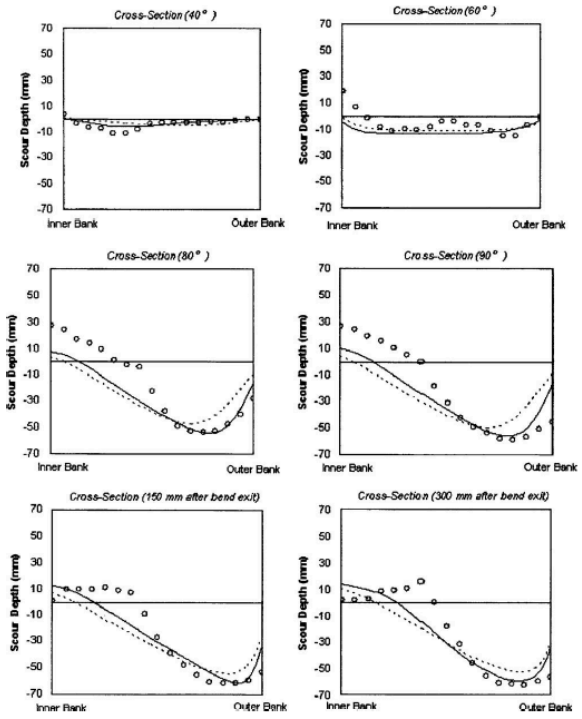

Figure 4.5: Comparison between experimental and numerical results for scouring in a 90 degree channel bend for different sections; the continuous line is from experimental data, the dotted line is from the model using the $k-\omega$ turbulence scheme and the line with circular markers is from using the $k-\epsilon$ turbulence scheme [58]

The numerical results did not disagree with the experimental by more than 13%,

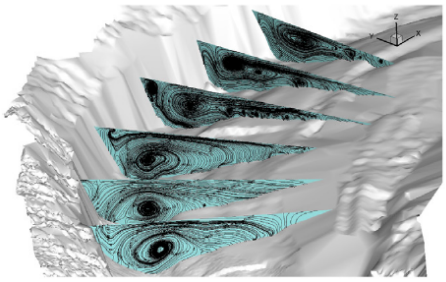

Figure 4.6: Transverse currents in channel bend [64]

and the model was considered to be of acceptable accuracy. The best results were obtained from the model that used the $k-\omega$ turbulence scheme. This is because $k-\omega$ models are considered to capture shear stresses on the bed better than $k-\epsilon$ models [63]. The authors concluded that there were three sources of significant error; the assumption of isotropic turbulence in channels is innaccurate, since the scales in each direction are very different. Furthermore, the empirical relationships used to calculate the bed load fluxes and their direction are inherently inaccurate. Finally, the authors applied a rigid lid model, which may have suppressed the appearance of certain secondary currents.

In 2008 Garcia et al [65] presented a free-surface flow, non-hydrostatic deformable mesh model with bed scouring capabilities, and ran simulations of scouring from a horizontal jet impinging on a movable bed, based on experiments carried out by Chatterjee et al [66]. Figure 4.7 shows a schematic of the setup on which the experiments and simulations were based.

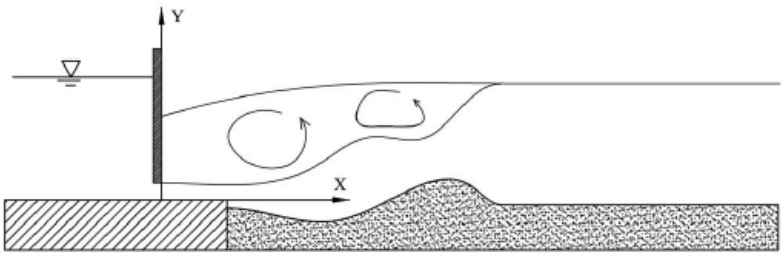

Figure 4.7: Turbulent wall jet impinging on a movable bed; schematic view [65]

The hydrodynamic model was based on the finite volume approach in an unstructured deformable mesh. The free surface was modeled using the VOF scheme. For bed scouring the authors used a quasi-steady approach. Like in previous work the authors used the Shields criterion for initiation of scouring. The bedload fluxes were calculated from the following formula:

$$q_i = q_o \frac{\tau_i}{|\tau|} - C|q_o| \frac{\partial \eta}{\partial x_i} \ , \tag{4.35}$$

where τ_i is the i component of the local stress on the bed, $|\tau|$ is the stress magnitude, η is the bed elevation, C is a constant that varies between 1.5 and 2.3, and which determines the effect that the bed slope has on the bedload fluxes [67]. q_o is the bedload flux magnitude for a flat bed, given by:

$$q_o = q^* \sqrt{Rgdd} \ , \tag{4.36}$$

where R is the sediment submerged specific gravity, d is the sediment median diameter size and g is the acceleration of gravity. q^* is a dimensionless bedload transport rate given by [55]:

$$q* = 18.74(\theta - \theta_c)[\theta^{1/2} - 0.7\theta_c^{1/2}] \ , \tag{4.37}$$

where θ is the Shields stress and θ_c is the critical Shields stress. The critical Shields stress is a function of the critical Shields stress for a flat bed, θ_{c0} and the local angle of inclination. For its computation the same formula used by Roulund et al [47], (4.15), was used. However, while Garcia accounted for the local angle of inclination in the

bed morphology in his model, he used an empirical formula in the Exner equation to account for it, while Roulund et al [47] solved the specific equations of motion to find the bedload flux vector. The authors used the finite volume approach to solve the Exner equation. Figure 4.8 shows the results of their simulation for scouring at different times compared to experimental results from Chatterjee et al [66].

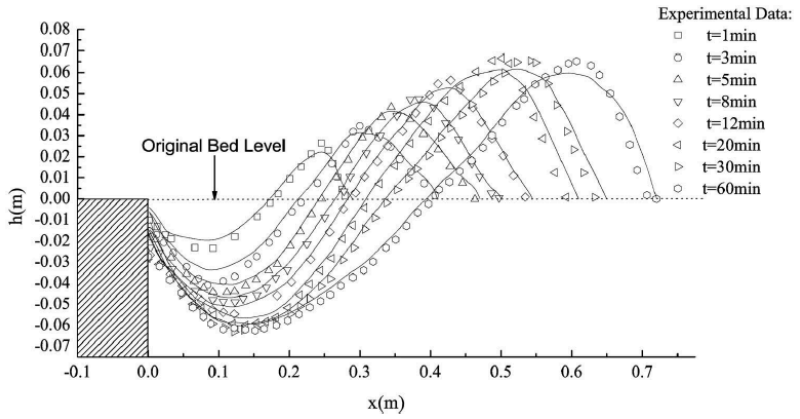

Figure 4.8: Comparison between numerical and experimental results [65]

It can be seen from the figure that the authors got good agreement with experimental data. Figure 4.9 shows the flow field at a certain time of their simulation, and it can be seen that the model captured areas of recirculation well. A two-equation $k-\epsilon$ turbulent scheme was implemented, which may have been appropriate for a case like theirs where turbulence in the domain or interest could be considered isotropic.

In the work of this thesis two modules are incorporated in the scouring model, which can be used interchangeably. One implements the methodology by Roulund et al [47] to calculate the bedload fluxes while the other module implements the methodology by Garcia et al [65] to account for the bed inclination in the flux calculation. The difference between the two methodologies in terms of practicality is that the latter is more computationally efficient, since having to solve a set of non-linear equations of motion is not necessary.

Apsley et al [68] presented a model for bedload transport in 2008. The model was implemented within a finite volume RANS solver that used a curvilinear adaptive

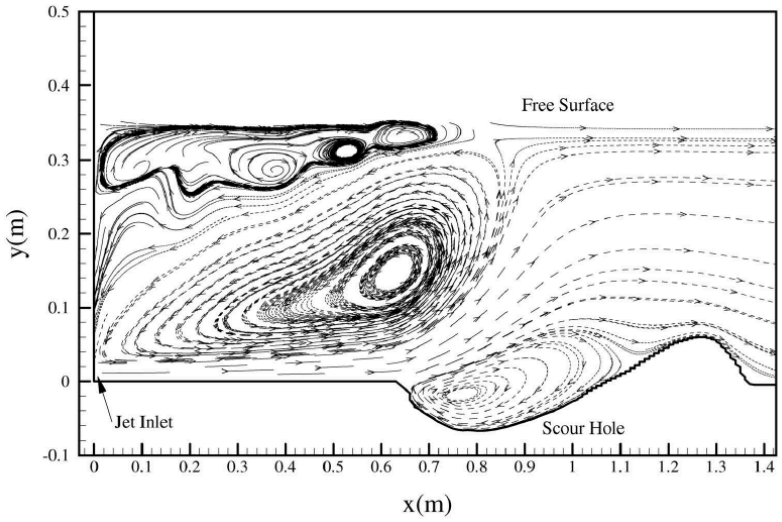

Figure 4.9: Flow field during scouring [65]

grid. The model used an 'effective stress' instead of a flow induced stress in the direction of the flow, by accounting for the weight component of a bed particle in the direction of maximum slope, which in general is not aligned with the flow vector. The bed has a local angle of inclination. The plane of inclination was defined by the normal vector, given by:

$$\hat{\mathbf{n}} = \frac{1}{\sqrt{1 + \mid \bigtriangledown z_b \mid^2}}(-\frac{\partial z_b}{\partial x}, -\frac{\partial z_b}{\partial y}, 1) \ , \tag{4.38}$$

where z_b is the bed elevation. The angle of inclination, β is $\beta = cos^{-1} n_z$, where n_z is the component in the z direction. If $\hat{\mathbf{e}}_\mathbf{z}$ is the unit vector in the vertical direction, the unit vector in the direction of maximum slope, $\hat{\mathbf{b}}$, will be given by $(\hat{\mathbf{e}}_\mathbf{z} \times \hat{\mathbf{n}}) \times \hat{\mathbf{n}}$. The forces acting on a bed particle were the fluid force, $\boldsymbol{\tau} A_s$, where $\boldsymbol{\tau}$ was the flow induced stress and A_s was a representative area of the particle; then there was the buoyancy-reduced weight component, $W' sin\beta \hat{\mathbf{b}}$, W' being the weight adjusted for buoyancy; finally there was the frictional force that acted against the combination of the other two forces, and was given by $\mu W' cos\beta$, where μ is a friction coefficient, given

by $\mu = tan\phi$, where ϕ is the angle of repose. The authors combined the flow-induced stress force with the weight component into what they called the effective stress force:

$$\boldsymbol{\tau}_{eff} A_s = \boldsymbol{\tau} A_s + W' sin\beta \hat{\mathbf{b}} \ . \tag{4.39}$$

The authors adjusted the critical Shields parameter for the local inclination:

$$\boldsymbol{\tau}^*_{eff,crit} = \boldsymbol{\tau}^*_{crit,0} cos\beta \ . \tag{4.40}$$

The above formula is much simpler than that one used by Roulund et al [47] (formula (4.15)). The difference is that the authors did not account for the angle between the flow velocity vector and the weight component in the direction of maximum slope when adjusting the critical Shields parameter. Their argument was that any local inclination reduces the weight component in the vertical direction, and thus reduces the frictional force that is opposed to motion. Once the three vectors were calculated – the flow-induced stress, the weight component and the frictional force – the authors computed the bedload flux vector. The approach followed for calculating the forces on a bed particle and applying a force balance to find the fluxes was similar to the one followed by Roulund et al [47], with the difference that the latter did not assume a flow-induced drag in the direction of flow, but instead solved for the more general case in which the flow induced drag is in the direction of a relative-to-the-flow particle velocity; in theory the approach by Roulund et al was more complete and more accurate than the one by Apsley et al [68], even though it was published three years prior. The authors also incorporated an avalanche (sand slide) algorithm in their model. The sand slide flux was given by:

$$q_{aval} = (1-p)\frac{\frac{1}{2}L^2(tan\beta - tan\phi)}{cos\beta\Delta t}\ , \tag{4.41}$$

where p is the sediment porosity, L is the length of the side through which there is flux, ϕ is the angle of repose and β is the angle of inclination (greater than the angle of repose). The sand slide flux, as given above, should adjust the angle of inclination, so that it not exceed the angle of repose, in a single time step. This was a different methodology from the iterative approach with smaller (virtual) time steps in an inner loop, implemented by Roulund et al [47], where the sand slide fluxes were calculated by means of a physical argument taking into account the specific forces that generate the sand slide. In both cases the sand slide flux was directed along the slope of maximum inclination, $\hat{\mathbf{b}}$. To update the bed elevation the authors solved the Exner equation by using a finite volume approach. The bedload fluxes had to be computed at the cell edges, and the problem was set up so that neighboring cell halves share a common angle of inclination. To find the angle of inclination, so that it be shared by sections of neighboring cells, the authors fitted a plane on control points, that is cell centers, of neighboring cells that exchange bedload material. The equations of motion to find the grain velocities were based on the inclination of the fitted planes. Figure 4.10 shows the procedure in 2D, as well as a problem that arose; the inclined bed that the bedload model 'saw' was not made up of the actual cell surfaces, but instead was a 'virtual' plane created by means of interpolation. A sawtooth pattern (in 2D) appeared, which the bedload model failed to 'see' and account for, but instead reinforced. To solve this problem the authors had to add an artificial flux term based on the inclination of the actual cell surfaces, which created a movement of material from the elevated half of a cell to the lower half.

This problem as well as the method used to solve it is very similar to one in an

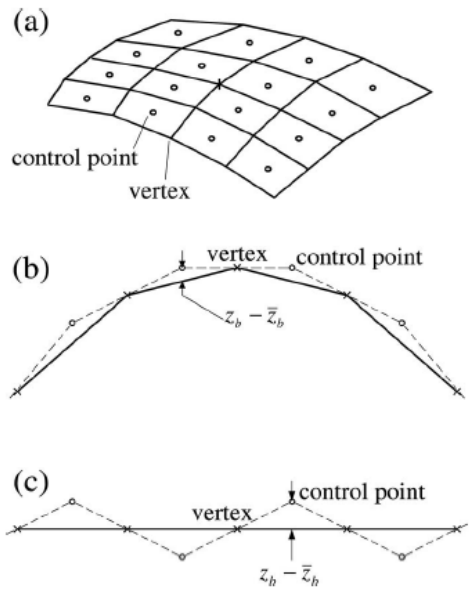

Figure 4.10: Methodology followed to find the local inclination, as well as the sawtooth instability that arose [68]

initial bedload transport methodology that is developed independently as part of this thesis. A 'virtual' bed surface is created in that model by means of an averaging process, and the equations of motion are solved on that surface. Because the model fails to 'see' the actual bed morphology, a checkerboard pattern appears, which in 2D would be a sawtooth pattern. To solve this an artificial flux term is added. Another methodology is chosen though, developed later, that directly accounts for the actual localized inclination, and which is devoid of such numerical instabilities. Both models will be described below.

The authors tested their model by simulation of scouring in a 90^o channel bend, following experiments carried out by Kawai et al [69]. Figure 4.11 depicts the bed elevations at maximum-scour locations along the inner and outer banks of the channel; their results are juxtaposed to experimental data. The authors got relatively good agreement with experimental data.

Sotiropoulos et al [70] presented the latest bedload transport model to date in 2011. The hydrodynamic model used a finite volume RANS solver in a curvilinear

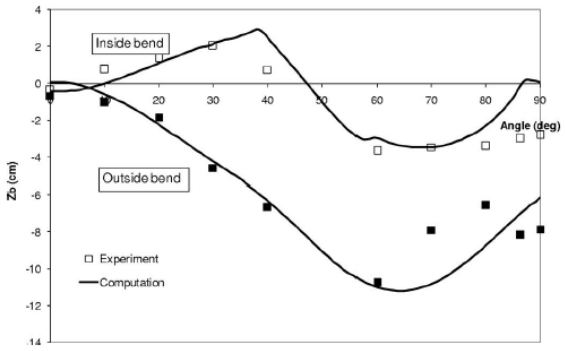

Figure 4.11: Experimental and numerical results of maximum scouring along inner and outer banks of a channel bend [68]

grid, with a $k - \omega$ closure scheme. What was unique in the model was that it used an immersed boundary method to model a moving bed. In the method only a part of the grid – the part above the bed – was 'active', that is the flow field was resolved in that part. A schematic of the grid is shown in figure 4.12.

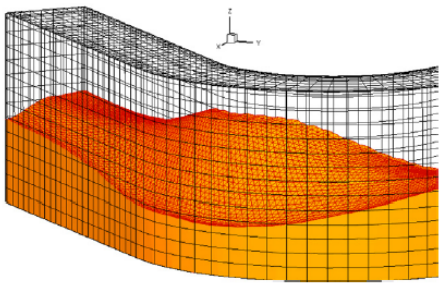

Figure 4.12: Grid with immersed boundaries used in the model [70]

As the bed moved new grid nodes were exposed and the flow field was expanded, or existing grid nodes were covered by the bed, and the volumes they delineated were 'deactivated'. The advantage of the approach is that re-meshing was not required and the cost of doing so was avoided. Furthermore, the method allowed for capturing complex geometries, since various features outside the flow field could just be embedded in it. At the same time, the bed was discretized as an unstructured triangular mesh, forming a C^0 continuous surface. Since the boundary velocities were not readily available for the scouring model an interpolation methodology was followed, as

shown in figure 4.13.

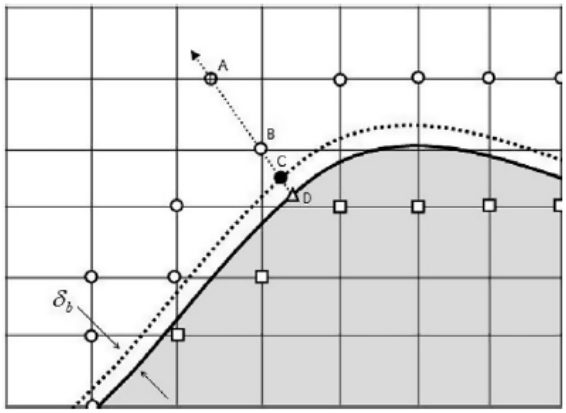

Figure 4.13: Immersed boundary method on a moving bed [70]

A normal was taken from a node adjacent to the bed (node B) to the bed and the normal was extended into the flow (point A). The flow velocity at point A was found by interpolation from adjacent nodes. Once that was found and applying the law of the wall, the friction velocity was computed. From knowing the friction velocity and applying the law of the wall one more time, the velocity at the boundary node (node B) was found. Once the boundary node velocities were known, a normal was drawn from the centroid of the triangle forming the bed mesh (point D). The velocity at the intersection of the normal with the edge of the bed load layer (point C) was calculated once the nodal velocities were known. The velocities at the edge of the bedload layer were used in the scouring model by using the formula:

$$\mathbf{q}_{BL} = \Psi |d\mathbf{s}| \delta_{BL} \mathbf{u}_{BL} \ , \tag{4.42}$$

where $\mathbf{q}_{BL}$ is the bedload transport rate through edge $d\mathbf{s}$ with normal δ_{BL}, and $\mathbf{u}_{BL}$ is the flow velocity at the edge of the bedload layer. Ψ is the local sediment concentration on the bed, given by Van Rijn [72] as follows:

$$\Psi = 0.015 \frac{d_{50}}{\delta_b} \frac{T^{\frac{3}{2}}}{D_*^{\frac{3}{10}}} \ , \tag{4.43}$$

where

$$D_* = d_{50} [\frac{(\rho_s - \rho) g}{\nu^2}]^{\frac{1}{3}} \tag{4.44}$$

and

$$T = \frac{\tau_* - \tau_{*cr}}{\tau_{*cr}} \ , \tag{4.45}$$

where d_{50} is the median grain diameter, δ_b is the bedload layer thickness, ρ and ρ_s are the density of water and bed material respectively, g is the acceleration of gravity and ν is the kinematic viscosity of water. τ_* is the Shields stress and τ_{*cr} is the critical Shields stress. Equation (4.44) is similar to equation (4.14) that gives the percentage of bed particles in motion by Roulund et al [47]. The critical Shields stress was computed from the critical Shields stress for a flat bed by adjusting for the local angle of inclination and the direction of flow, using formula (4.15) that was described in the work by Roulund et al [47]. However, it should be noted that the authors do not explicitly account for a weight component in the direction of maximum slope, like in the work by Roulund et al [47] or that by Apsley et al [68], but assumed that the bedload fluxes were in the direction of the flow. Once the bedload fluxes were computed, the bed elevation was updated by solving the Exner equation using the divergence theorem (4.4). The hydrodynamic model did not conserve mass locally as the bed morphology changed, since the algorithm that re-created the bed surface did

not have such a provision. Global mass conservation was achieved by adjusting the mass outflow rate in accordance to the bedload material volume change rate as:

$$Q_{out} = Q_{in} + \frac{\partial V}{\partial t} \ , \tag{4.46}$$

where Q_{out} is the volume outflow flow rate, Q_{in} is the inflow flow rate and $\partial V/\partial t$ is the bed material volume change rate. To solve the Exner equation the authors alternatively implemented two different schemes. The GAMMA scheme is a hybrid first-order upwind, second-order central scheme, while a first-order upwind (FOUW) scheme was also implemented. To validate their model, the authors ran simulations of flow in channels with bends of varying degrees and movable beds, in accordance to experiments carried out by Pirestani [71]. Figure 4.14 show a comparison of results for flow in a 90^o channel bend.

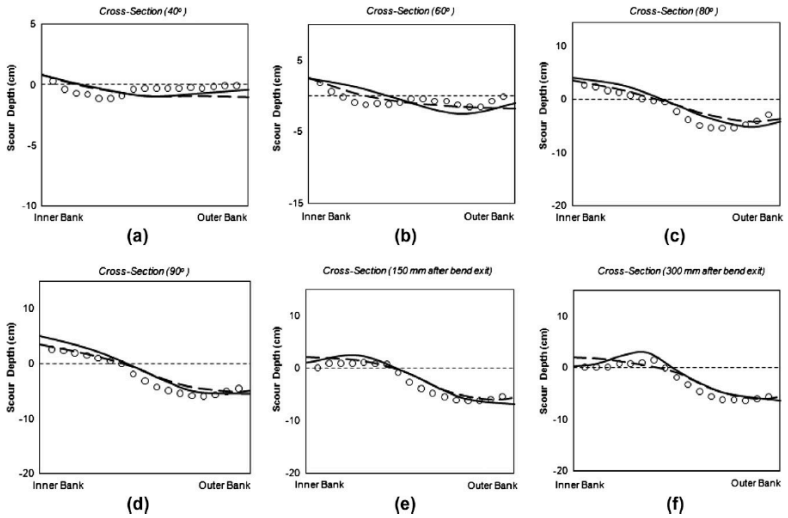

Figure 4.14: Comparison of measured results (circles) with computed with FOUW (dashed lines) and GAMMA (solid lines) schemes [70]

The authors achieved good agreement with both schemes for solving the Exner equations. The GAMMA scheme gave slightly better results, due to its less diffusive nature.

4.2 The Movable Bed Model

4.2.1 Mode of Sediment Transport in the St. Clair River

In this work, emphasis is given on bedload transport and a model is developed and coded that can do that. The question that arises is why expect sediment transport to happen by way of bedload transport and not by way of suspended sediment transport instead. The drop in stage elevation from the entrance of St. Clair River in Lake Huron to the outflow in Lake St. Clair is approximately 1.6 meters, and the average flow velocity is 1.7m/s. Observations show that there are no abrupt drops in stage elevation along the length of the river and the flow is always well into the subcritical domain with the Froude number always below unity. The material comprising the bed was studied experimentally [78] and it was found that the river bed along its length and for the greater part of its width consisted of gravel with average diameter no less than 12mm. Figure 4.15 shows the longitudinal distribution of gravel size in St. Clair River.

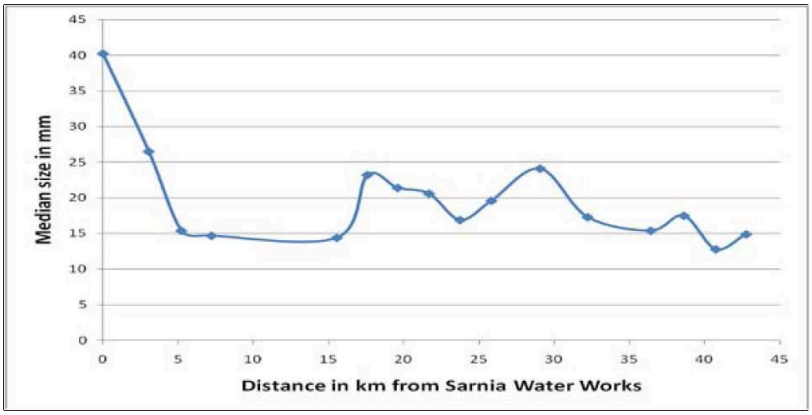

Figure 4.15: Longitudinal median grain diameter distribution along the river thalweg[78]

The type of sediment transport is governed by the Rouse number, which is a ratio of the gravity force on sediment grains that tends to keep them on the river bed, to the upward forces of lift and drag. The Rouse number is given by equation (4.47) :

$$P = \frac{w_s}{\kappa u_*} \, , \tag{4.47}$$

where w_s is the settling velocity of the sediment, κ is the Von Karman constant taken equal to 0.41, and u_* is the shear or friction velocity (explained later). The criterion that governs the dominant mode of sediment transport is given in table 4.16, based on experimental observations and analytical studies [45]:

Mode of Transport	Rouse Number
Initiation of motion	>7.5
Bed load	>2.5, <7.5
Suspended load: 50% Suspended	>1.2, <2.5
Suspended load: 100% Suspended	>0.8, <1.2
Wash load	<0.8

Figure 4.16: Criterion that determines mode of sediment transport [45]

The settling velocity of sediment, which is the constant fall velocity in an undisturbed fluid, when there is balance between gravity and drag, is given by the universal formula by Ferguson et al [46] as:

$$w_s = \frac{RgD^2}{C_1\nu + (0.75C_2RgD^3)^{0.5}} \, , \tag{4.48}$$

where R is the submerged specific gravity (1.65 for quartz in water), g is the acceleration of gravity and ν is the kinematic viscosity of the fluid (water). D is the grain diameter. C_1 and C_2 are constants, which for natural grains are given the values $C_1 = 18$ and $C_2 = 1$ of Ferguson [46].

For the sake or argument, it can be calculated that for a grain with diameter equal to 4mm, in order for the Rouse number to be equal to 2.5, the flow velocity 0.5 meters above the bed must be equal to $4.73m/s$. For a grain diameter equal to 10mm, the

velocity has to be $6.65 m/s$. Considering the grain size distribution in figure 4.15, it becomes evident that for the St. Clair River sediment transport will be practically exclusively by means of bedload transport. This means that the grains will move very near the bed, their movement characterized by sliding and saltation.

4.2.2 Modeling The Drag Force on the River Bed

The boundary condition that Suntans uses at the river bed is based on a drag law and is given below:

$$\nu_V \frac{\partial U}{\partial z}\bigg|_{z=h}^{n+1} = C_{d,B}|U|U \ , \tag{4.49}$$

where U is the horizontal velocity, ν_V is the vertical turbulent viscosity and $C_{d,B}$ is the bed drag coefficient. The equation is derived from the law of the wall, first formulated by Von Karman, that states that the average flow velocity at a point in a turbulent flow field is proportional to the logarithm of the distance from that point to the wall, which in this case is the bed of the channel. The law applies well to velocity profiles of natural streams, but is more accurate near the bed ($< 20\%$ of the height of the flow), which is well within the range that the model uses to calculate the stress on the bed of the channel. In dimensional form the law is written as:

$$u = \frac{u_*}{\kappa} \ln \frac{y}{y_0} \ , \tag{4.50}$$

where u is the average velocity a distance y from the wall and y_0 is the theoretical distance from the wall at which the velocity goes to zero. κ is Von Karman's constant taken as 0.41. u_* is the so-called friction velocity given by:

$$u_* = \sqrt{\frac{\tau_w}{\rho}} \,, \tag{4.51}$$

where τ_w is the wall stress and ρ is the density of water. The friction velocity is a measure of the flow-induced stress on the bed. The distance y_0 is calculated differently depending on whether the roughness elements for the wall are within the viscous sublayer (hydraulically smooth flow) or whether they 'stick out' (hydraulically rough flow). In our case it is easy to ascertain that the flow is rough. If the roughness elements are within five wall units from the wall (within the viscous sublayer), then the flow is smooth. A wall unit is given by the formula:

$$y^+ = \frac{yu_*}{\nu} \,, \tag{4.52}$$

where y^+ is a wall unit and ν is the kinematic viscosity of water. Open channel flow theory [44] estimates the shear stress on the bed by the following formula:

$$\tau_w = \frac{\rho g n^2}{H^{\frac{1}{3}}} |U| U \,, \tag{4.53}$$

where g is the acceleration of gravity, n is Manning's coefficient (units $s/m^{\frac{1}{3}}$), H is the depth of flow and U is the average flow velocity. For a flow depth of 7m, an average flow velocity of 1m/s and a very conservative figure for Manning's n of $0.02 s/m^{\frac{1}{3}}$, the shear stress on the bed is approximately 2.05Pa. The numerical values chosen are representative of St. Clair River. Then, a roughness element of 10mm will be 452 wall units in height. The flow is hydraulically rough, in which case y_0 is calculated by:

$$y_0 = \frac{k_s}{30} \, , \tag{4.54}$$

where k_s is a roughness length scale, called the Niduradse roughness coefficient, which for river beds can be taken as [57] :

$$k_s \approx 3.5 d_{85} \, . \tag{4.55}$$

d_{85} is the the 85th percentile grain diameter, and is approximately 1.5 times the median grain diameter, d_{50}, of the bed [56]. Using equation (4.50) one can derive equation (4.49) by taking:

$$C_{d,B} = (\frac{1}{\kappa} \ln \frac{y}{y_0})^{-2} \, . \tag{4.56}$$

Then equation (4.49) is obtained by setting:

$$\frac{\tau_w}{\rho} = \nu_V \frac{\partial U}{\partial z} \, , \tag{4.57}$$

where the coordinate y has been replaced by z, and the derivative is numerically calculated by using a small distance from the bed, $\Delta z/2$. The final formula then by which $C_{d,B}$ is calculated is then:

$$C_{d,B} = (\frac{1}{\kappa} \ln \frac{\frac{\Delta z}{2}}{\frac{3.5 * 1.5 * d_{50}}{30}})^{-2} \, . \tag{4.58}$$

Then the friction velocity, u_τ, can be calculated by using:

$$u_* = \sqrt{C_{d,B}}|U| \ , \tag{4.59}$$

where $|U|$ is the magnitude of the flow velocity some distance $\Delta z/2$ from the bed, based on which the drag coefficient $C_{d,B}$ is calculated. Nondimensionalizing the stress on the bed we get:

$$\theta = \frac{u_*^2}{(s-1)gd_{50}} \ , \tag{4.60}$$

where θ is the non-dimensional Shields stress, s is the specific gravity of the sediment, g is the acceleration of gravity and d_{50} is the median grain diameter of the sediment. Based on experimental work, it has been observed that measurable bedload transport occurs when θ exceeds a certain value. This critical value is called the critical Shields stress, which we will denote by θ_{cr}, and the criterion that it defines is called the Shields criterion. The critical Shields stress value varies depending on the kind of sediment that comprises the surface layer of the bed. For a bed with a uniform grain size, the nominal value of 0.047 is given [73], [77]. However, based on experimental studies and field observations of bedload transport in rivers, for beds with mixed grain composition, the value of 0.03 is most accurate [75], [76], [74]. The reason for the lower value is that while the critical Shields stress for grains of median diameter, d_{50}, has a certain value, in mixed grain sediments smaller grains will be mobilized at lower stress values. As such, the Shields stress value at which sediment transport becomes significant will be lower than the nominal value for sediment of uniform grain size. The value of 0.03 has been adopted in the simulations of flow in the St. Clair River. While the Shields stress on the bed is below the value of

0.03 under normal flow conditions in the St. Clair River, there still is a very small but detectable amount of bedload material transported downstream [78]. This is significant in terms of the argument above on selective sediment mobilization.

4.2.3 Modeling Bedload Transport

Implementing a bedload transport model involves knowing the stresses on the bed, as well as the angle of inclination at various locations on the bed. As was seen in previous models, the critical Shield's stress as well as the direction of sediment movement at a certain location depend on the inclination of the bed at that location. Suntans implements a z-axis grid, and the bed morphology is modeled as a series of 'steps'. This means that angles of bed inclination at different bed locations are not readily obtainable. This feature is unique to Suntans, since all previous models used adaptive griding, where the bottom-most cells followed the contour of the bed. To the author's knowledge, the only model that did not use an adaptive deformable mesh was that by Sotiropoulos et al [70], who used the immersed boundary method in their model. On the other hand, there are advantages to using a z-axis grid. One of them is that the model allows for unsteady geometries without having to continuously re-mesh the domain. The top layer of cells expands or shrinks to follow the movement of the free surface, while the code is adjusted to allow for an unsteady bed morphology. This is done by changing the height of the bottom-most cells to adapt to changes in morphology, and if the changes in height exceed a certain value the code adds or subtracts cells from the bottom layer of the grid. The benefit is twofold; by not having to re-mesh the entire domain, computational cost is minimal. Uniformity of the grid as a whole is maintained even after big changes in bed morphology, because the code just adds or subtracts elements from the grid boundary. This was not the case for other unstructured adaptive grid models, like the one by Garcia et al [65]. Furthermore, boundary velocities are readily available from resolving the flow field, unlike in the

model by Sotiropoulos et al [70], who had to use an interpolation technique to find flow velocities near the bed. Finally, unlike models that used structured grids, Suntans uses an unstructured grid that allows for meshing complex domains without grid deformations. In developing the bedload transport model work was done for finding the local angle of inclination at any location on the bed. One method that is developed is to map the discontinuous 'stepwise' domain to a C^0 continuous surface domain. This is achieved by assigning at each node of the triangular mesh that is a shared vertex a depth equal to the weighted average of the depths of the cells that share the node. The process can be visualized in figure 4.17 below, where the 2D equivalent case is also presented.

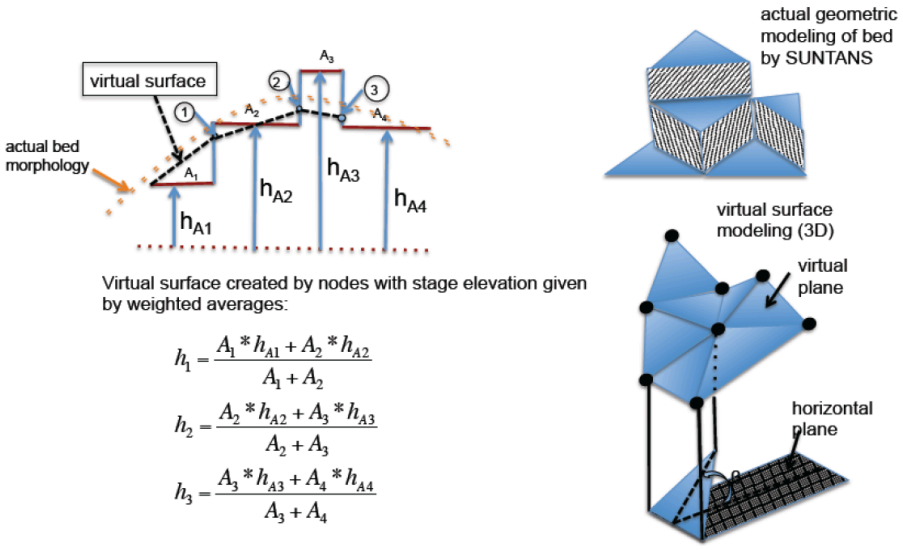

Figure 4.17: Constructing the bed geometry

The created virtual surface, which is an approximation of the bed morphology, consists of triangular elements at a certain inclination with the horizontal. Specifically, for each element, there is an angle of inclination, β, corresponding to the direction of maximum slope with respect to the horizontal plane, which affects both the magnitude and the direction of the bedload fluxes. Figure 4.18 shows the geometric relationships for finding β.

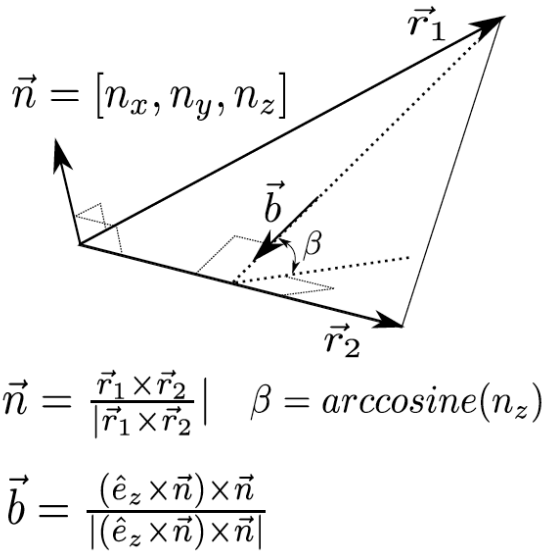

Figure 4.18: Finding the bed inclination

The direction of maximum slope, which is the line of action of the weight component along the bed, is given by the unit vector, $\vec{b}$:

$$\vec{b} = \frac{(\hat{e}_z \times \vec{n}) \times \vec{n}}{|(\hat{e}_z \times \vec{n}) \times \vec{n}|} \,, \tag{4.61}$$

where $\vec{n}$ is the unit vector normal to the bed and $\hat{e}_z$ is the unit vector in the z direction. Once a continuous bed morphology has been computed, the bedload fluxes can be calculated for each inclined triangular element that comprises the continuous surface. The approach followed to compute the bedload fluxes, once the bed inclination is found, is adopted from the work by Roulund et al [47], and involves solving the equations of motion for a single – representative – bed particle, and then extrapolating to find the bedload fluxes on each cell. Figure 4.19 shows the forces acting on a bed particle, as well as the dynamic and kinematic relations governing the movement of a bed particle.

The angle α between the weight component and flow velocity vector is computed by simply taking $\alpha = arccosine(\frac{\vec{U}}{|\vec{U}|} \bullet \vec{b})$, where $\vec{U}$ is the flow velocity vector near the

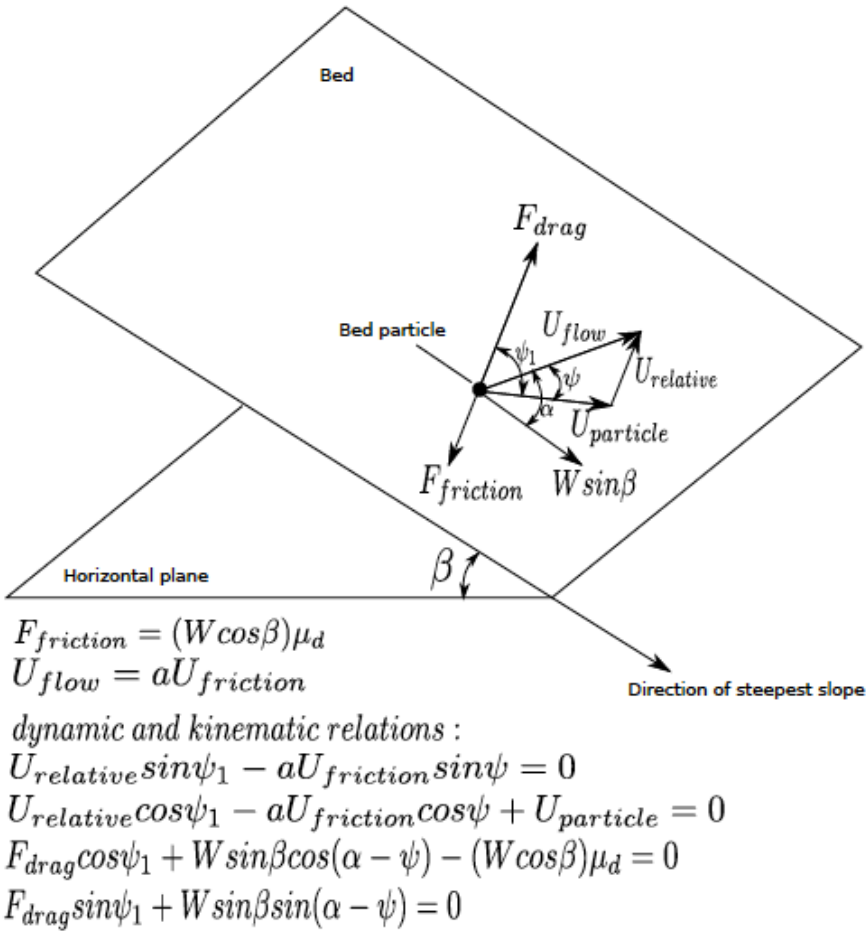

Figure 4.19: Geometric and analytic relations governing the movement of a bed particle

bed, taken as a multiple of the friction velocity vector [47].

Roulund [47] does not provide a methodology for calculating the geometric characteristics of the bed. He presents the necessary dynamic and kinematic relationships to solve and find the velocity of a bed particle, as seen above ((4.22), (4.23), (4.24), (4.25)). While the author does not say how he solved the system of non-linear algebraic equations, in this work the Newton-Raphson algorithm was successfully implemented. The algorithm provided necessary accuracy with only a few iterations, and proved to be computationally efficient. Once the bedload fluxes at each cell are calculated, the Exner equation is solved numerically in order to update the bed elevation. The Exner equation is:

$$\frac{\partial \eta}{\partial t} = -\frac{1}{1-n} \bigtriangledown \bullet \vec{q}\,, \tag{4.62}$$

where η is the bed elevation, n is the porosity of the sediment and q is the flux vector. The Exner equation is formulated and solved in the horizontal plane, so only the x and y components of the flux vector enter the equation. Integrating over an area A gives:

$$\int_A \frac{\partial \eta}{\partial t} = -\frac{1}{1-n} \int_A \bigtriangledown \bullet \vec{q} \tag{4.63}$$

and applying the divergence theorem gives:

$$A\frac{\partial \eta}{\partial t} = -\frac{1}{1-n} \int_{\partial A} \vec{q} \bullet \vec{n}\,, \tag{4.64}$$

where $\vec{n}$ is the outward normal. Discretizing for a computational cell i gives:

$$\frac{\Delta \eta_i}{\Delta t} = -\frac{1}{1-n}\frac{1}{A_i} \sum_{j=1}^{3} \vec{q}_j \bullet \vec{n}_j l_j\,, \tag{4.65}$$

where A_i is the horizontal area of the cell, i, $\vec{q}_j$ is the flux through side j with normal $\vec{n}_j$ and of length l_j. Referring to figure 4.20, if i and k are neighboring cells, the flux through the shared edge j is found by interpolation using a central scheme:

$$\vec{q}_j = \frac{\Delta x_1 \vec{q}_i + \Delta x_2 \vec{q}_k}{\Delta x_1 + \Delta x_2}\,. \tag{4.66}$$

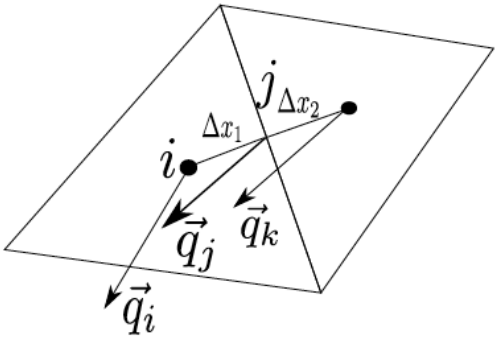

$$\vec{q}_j = \frac{\Delta x_1 \vec{q}_i + \Delta x_2 \vec{q}_k}{\Delta x_1 + \Delta x_2}$$

Figure 4.20: Method for calculating fluxes through edges

Figure 4.21 shows scouring under a sluice gate based on a simulation using this methodology for modeling the bed geometry.

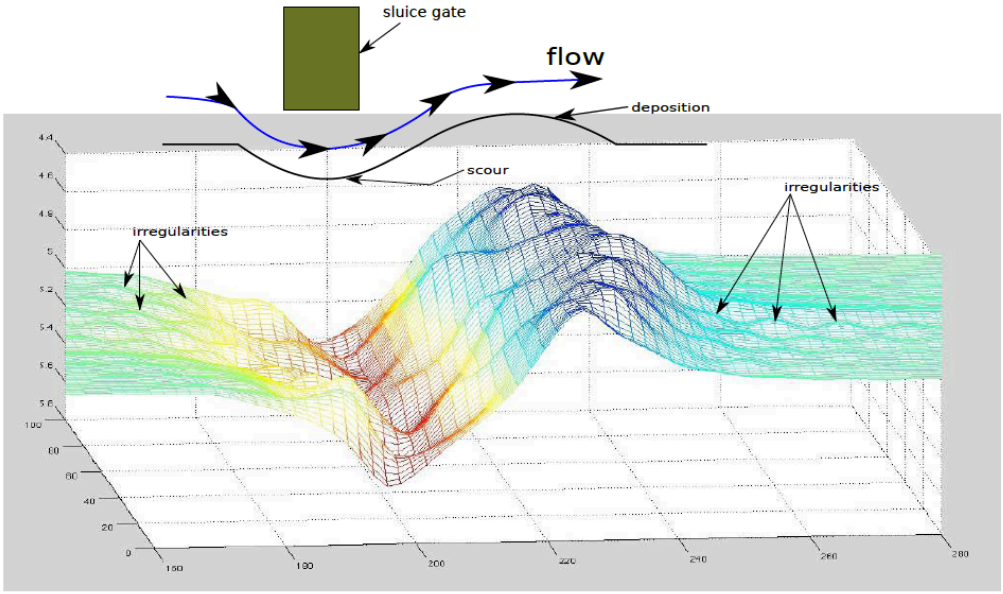

Figure 4.21: Scouring under a sluice gate

This method for modeling the bed geometry gives qualitatively intuitive results, provided a diffusive flux is added to the solution of the Exner equation. Referring to figure 4.21, a checkerboard type of instability appears in the solution, which can faintly be discerned in the figure. Figure 4.22 depicts an inclined plane after a sand

slide, where checkerboarding is clearly visible.

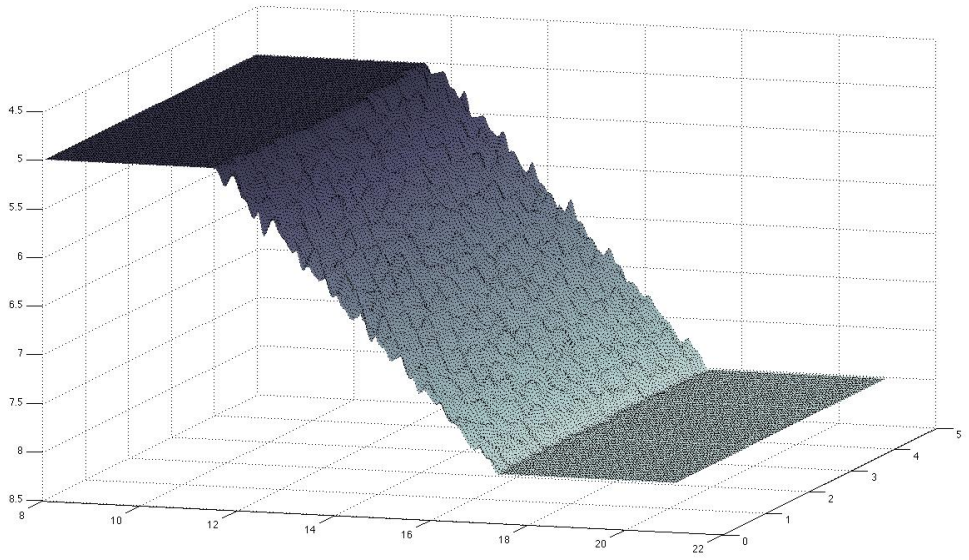

Figure 4.22: Sand slide simulation with checkerboarding

The reason for the instability is similar to the one described by Apsley et al [68] in their work for bedload transport modeling, and goes back to the way the bed morphology is reconstructed as a continuous surface. Since the depths at the vertices are produced by means of averaging out the depths of the cells sharing them, the model cannot 'see' the checkerboarding since the nodal depth averages out to a middle level. The mechanics of the instability are expressed in figure 4.23, which for simplicity depicts the instability in a 2D case.

The diffusive term that was added to the Exner equation was a function of the depth difference between neighboring cells, and, referring to figure 4.20 and equation (4.66), was included in the flux equation as:

$$\vec{q_j} = \frac{\Delta x_1 \vec{q_i} + \Delta x_2 \vec{q_k}}{\Delta x_1 + \Delta x_2} + f(d_1 - d_2) + g(d_1 - d_2) * |\frac{\Delta x_1 \vec{q_i} + \Delta x_2 \vec{q_k}}{\Delta x_1 + \Delta x_2}| \,, \qquad (4.67)$$

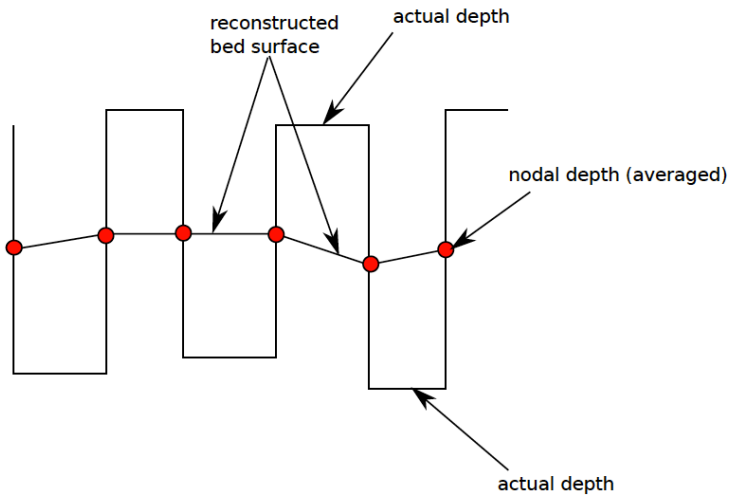

Figure 4.23: Mechanics of checkerboard instability

where d_1 and d_2 are the depths of neighboring cells and f is a monotonic function of the depth difference, that has a cutoff beyond which there is no diffusion; this is to prevent the bed from becoming completely flat over time. Typically the cutoff can be set to be some depth difference, below which diffusion stops. g is also a monotonic function of the depth difference, which has as a multiplier the flow-induced flux. The logic behind this third term is that cells experiencing high levels of fluxes are more prone to checkerboarding and need higher levels of diffusion to prevent it.

With the addition of artificial diffusion, the model was tested in sand slide simulations, and the results for simple geometries were good. In the case of sand slides, the velocity of bed particles was given by Roulund et al [47] (4.27). The sand slide algorithm works in an internal loop, assuming that sand slides are instantaneous in time, and the time step is adjusted so that the distance traveled by a particle in a time step does not exceed a characteristic length of the grid. Figure 4.24 shows the result of a sand slide in an inclined plane, where artificial diffusion has been used. There are no visible irregularities in the final configuration after the slide. The model works in such a way that sand slide is initiated when the local angle of inclination

exceeds the angle of repose by 2^o or more, and stops when it is 2^o below the angle of repose (here set to be 30^o). In the figure the plane is initially inclined at 45^o and after the slide it is inclined at 30.07^o. The scheme in this particular case proved to be highly accurate.

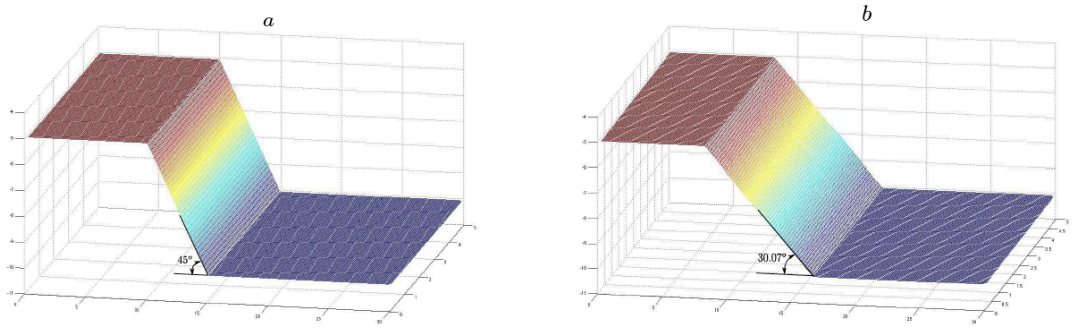

Figure 4.24: Sand slide in an inclined plane; (a) is the initial configuration with an angle of inclination of 45^o and (b) is the final configuration where the angle of inclination is 30.07^o. Artificial diffusion has been added

Because of the accuracy of the scheme in simulating sand slides, it has been adopted as the scheme of choice when it comes to large-scale sand slides, while for flow-induced scouring a different scheme is implemented that is inherently stable, as will be described below. Figures 4.25 and 4.26 show a sand slide in a conical pile of sand, with figure 4.25 showing the initial configuration before the slide and figure 4.26 showing the pile after the slide. The critical angle of repose condition is met within one degree after the slide stops.

As mentioned above, a different geometric modeling scheme is used for flow-induced scouring, that does not require the addition of artificial diffusion terms in the Exner equation. Figure 4.27 depicts the methodology followed.

In this scheme, neighboring cells share an inclined plane formed by taking the cross product of the shared edge and the vector formed by connecting the Voronoi points

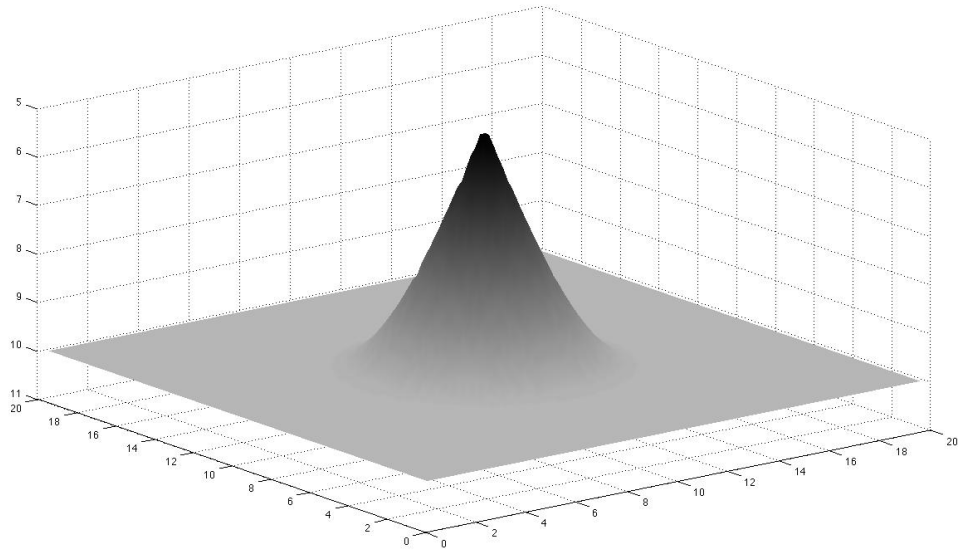

Figure 4.25: Sand slide in a conical pile of sand; initial configuration

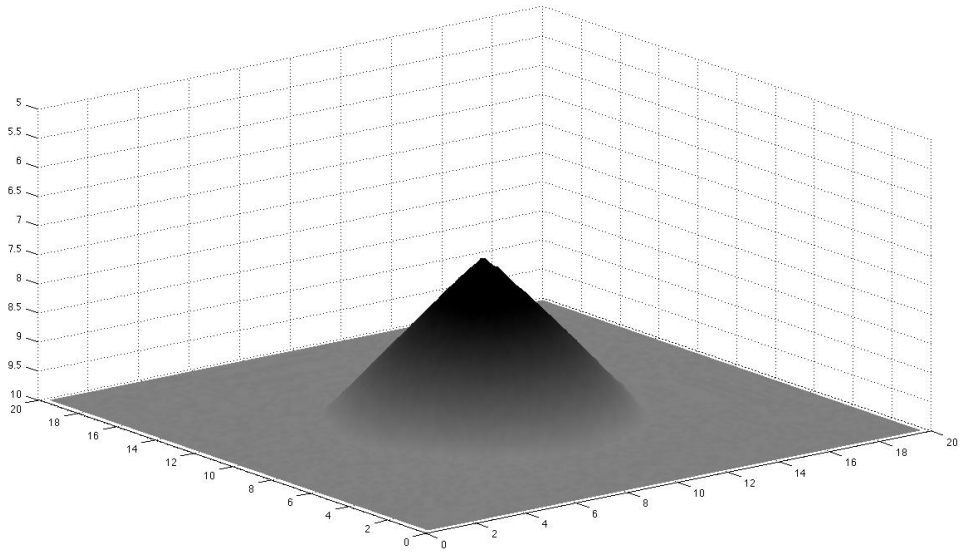

Figure 4.26: Sand slide in a conical pile of sand; final configuration

of the two cells. In this way, each cell is divided in three parts where to each part there corresponds a different angle of bed inclination, β. To find the sediment fluxes

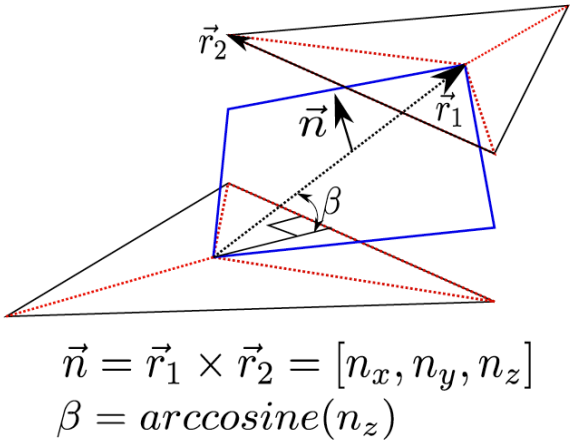

Figure 4.27: Geometric scheme followed in order to find the bed inclination

through the edges, while the flow velocity at the center of each cell is considered, the velocity of the grains and by extension the fluxes are computed separately for each third of the cell, since each third has a different angle of inclination. Furthermore, neighboring thirds of cells don't share the same flux, since, while they share the same angle of inclination, to each cell there corresponds a different flow velocity. Figure 4.28 depicts the scheme followed to compute the fluxes at the edges, as well as the way that the Exner equation is numerically solved.

The success of the method is based on the fact that there is no averaging process to derive the bed inclination and any checkerboarding is avoided. Once the angles of inclination are computed, two different methodologies are available to find the particle velocities and fluxes. One is that already used in previous versions of the model, and involves solving the equations of motion according to the methodology originally presented by Roulund et al [47] and adopted in this work, as seen in figure 4.19. The other methodology for computing the fluxes involves accounting for the bed inclination by using an empirical formula in the following way:

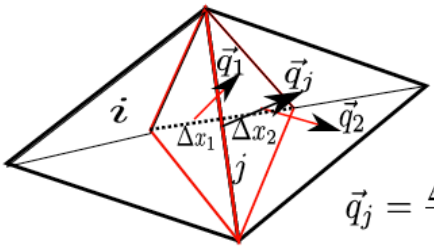

$$\vec{q}_j = \frac{\Delta x_1 \vec{q}_1 + \Delta x_2 \vec{q}_2}{\Delta x_1 + \Delta x_2}$$

Exner equation: $\frac{\partial \eta}{\partial t} = -\frac{1}{1-n} \nabla \bullet \vec{q}_j$ η:bed elevation, n:porosity

$$\int_A \frac{\partial \eta}{\partial t} = -\frac{1}{1-n} \int_A \nabla \bullet \vec{q}_j \; -> A \frac{\partial \eta}{\partial t} = -\frac{1}{1-n} \int_{\partial A} \vec{q}_j \bullet \vec{n} dS$$

$$\frac{\Delta \eta_i}{\Delta t} = -\frac{1}{1-n} \frac{1}{A_i} \sum_{j=1}^{3} \vec{q}_j \bullet \vec{n}_j l_j$$

Figure 4.28: Scheme developed in order to find the fluxes through the edges; solution to the Exner equation

$$q_i = q_o \frac{\tau_i}{|\vec{\tau}|} - C q_o \frac{\partial \eta}{\partial x_i} \; , \tag{4.68}$$

as already used by Garcia et al [65] in their model. q_i is the flux in the i direction, q_o is the flux magnitude for a flat bed and τ_i is the flow induced stress in the i direction. η is the bed elevation and C is a constant. As seen in this empirical formula, the flux for a flat bed is adjusted by adding a second term that accounts for the local bed inclination. Figures 4.29 and 4.30 depict scouring under a sluice gate, in a similar fashion to that depicted in figure 4.21, where the two methodologies for computing the fluxes have been used alternatively. It can be seen that the results are similar for this simple case with a coarse grid. Furthermore, no checkerboarding is present, despite the lack of artificial diffusion.

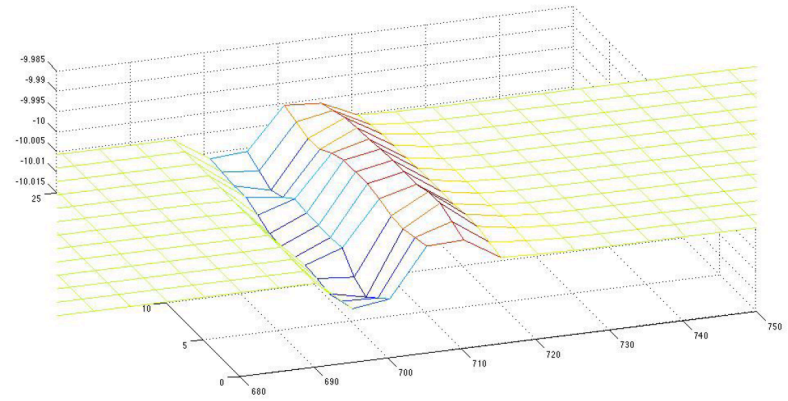

Figure 4.29: Scouring under a sluice gate; the fluxes are computed by solving the equations of motion for an inclined plane. No checkerboarding is present

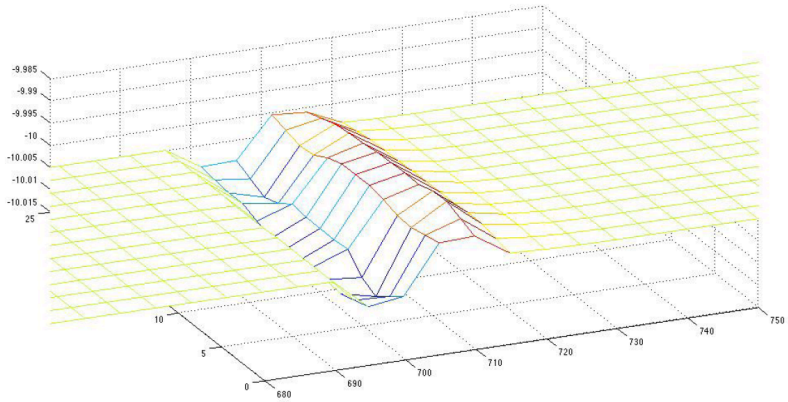

Figure 4.30: Scouring under a sluice gate; fluxes are computed by adjusting the fluxes for a flat bed to account for the bed inclination, by means of an empirical formula (4.68). No checkerboarding is present

4.2.4 Validation of The Model

In terms of validating the model, there are two considerations that need to be addressed. The first is that while all work that has been done by investigators, in terms of developing movable bed models, has been validated by comparing results with experiments in miniaturized settings, it is not clear that experimental findings in miniaturized settings accurately replicate moving bed phenomena in actual scales. To the knowledge of the author, there have not been any experiments in scales larger than the ones previously described, which are all miniaturized. The two key non-

dimensional parameters that characterize flow in open channels, the Froude number and the Reynolds number, differ by orders of magnitude between the miniature settings and the actual scales, provided the parameters that govern the movement of bed particles are kept the same, namely the Rouse number and the particle Reynolds number. The second, more practical consideration, is that Suntans was developed for large scale simulations and is computationally inefficient when dealing with very small scales, as in those encountered in experimental work. Specifically, every time the characteristic length scale of the grid is halved, the time step has to be divided by a factor of 4. Taking into account the doubling of the number of cells means that every time the grid is refined by a factor of 2, the computational time increases by a factor of 8. In light of this, it was not possible to run simulations with grid refinements similar to those used by other investigators.

The experiment that is chosen as a validation case is that of the horizontal jet impinging on a movable bed. The same case was simulated by Garcia et al [65], as has been described, and is based on experiments conducted by Chatterjee et al [66]. A schematic of the setup can be seen in figure 4.31.

The simulations that are carried out were based on one of the runs conducted by Chatterjee [66]; the setup is 3 meters long and the depth is approximately 0.3 meters. The jet aperture is 2 centimeters in height and the movable bed starts 0.66 meters downstream of the jet exit, the bed being rigid closer to that. The jet velocity is 1.56 m/s and the sand consists of uniform grain size of 0.76 millimeters. As pointed out by Garcia [65], the nature of the phenomenon is essentially two-dimensional, and the simulation is treated as such, in order to save in computational time. The grid constructed has 300 cells in the horizontal, with a characteristic length of 2 centimeters, and has 40 levels in the vertical, where the vertical length scale becomes finer towards the bed. At this level of refinement, the largest time step at which Suntans is stable was found to be 0.002 seconds. The run time for simulating flow

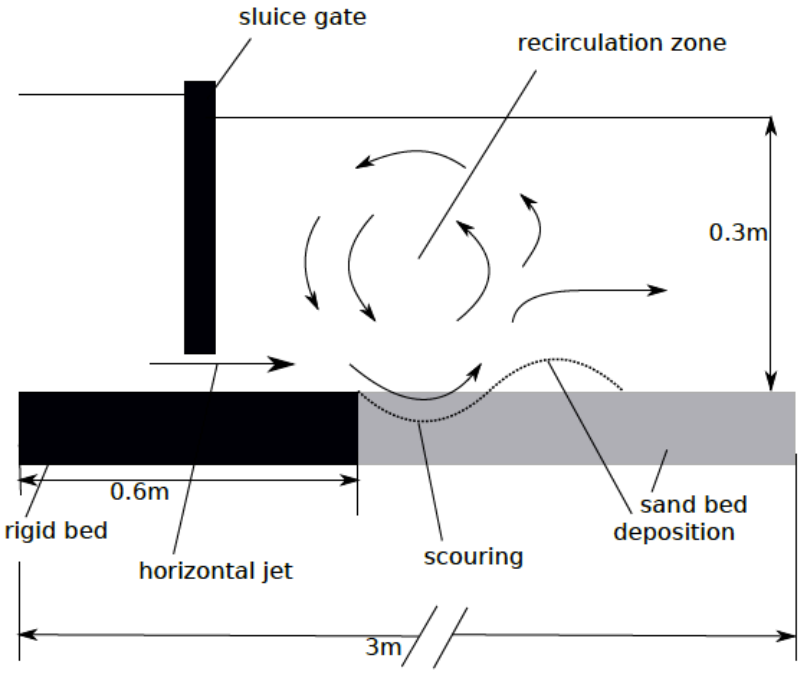

Figure 4.31: Schematic of experimental setup, based on which simulations for validation were conducted

for 5 min is approximately 5 hours. Most of that time (90%) is taken by the non-hydrostatic solver. Two more grids are used with characteristic horizontal lengths of 2.5 centimeters and 3 centimeters. Figure 4.32 is a plot of the Shields stress on the bed as a function of distance from the jet exit for the three grids, before any scouring has taken place.

It is clear from the figure that at these levels of grid refinement, the stress distributions on the bed under normal flow conditions with no scouring are practically identical for the three grids. Furthermore, it can be seen that the Shields stress clearly exceeds the threshold value of 0.05 [65] at the location of the beginning of the movable bed ($x = 0.66cm$) and for a distance downstream. Although the model zeroed out the flow-induced fluxes distances shorter than 0.66cm from the jet exit, sand slides were allowed to induce fluxes starting at shorter distances. This is in agreement with the model developed by Garcia et al [65]. The results from simulating flow with scouring for a duration of 5 minutes are shown in figure 4.33.

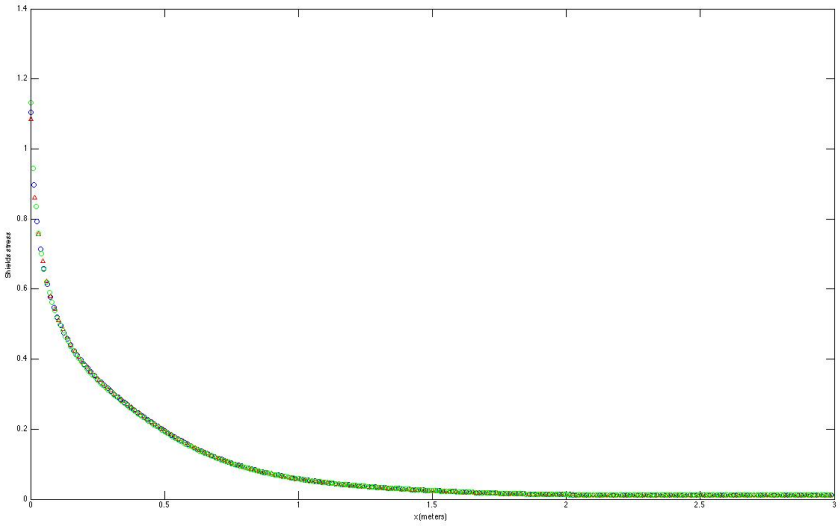

Figure 4.32: Plots of the Shields stress on the bed for the three different grids under normal flow conditions with no scouring; blue circles belong to the 2cm characteristic length grid; red triangles to the 2.5cm one and green circles to the 3cm one. It can be seen that at these grid resolutions there is no significant difference

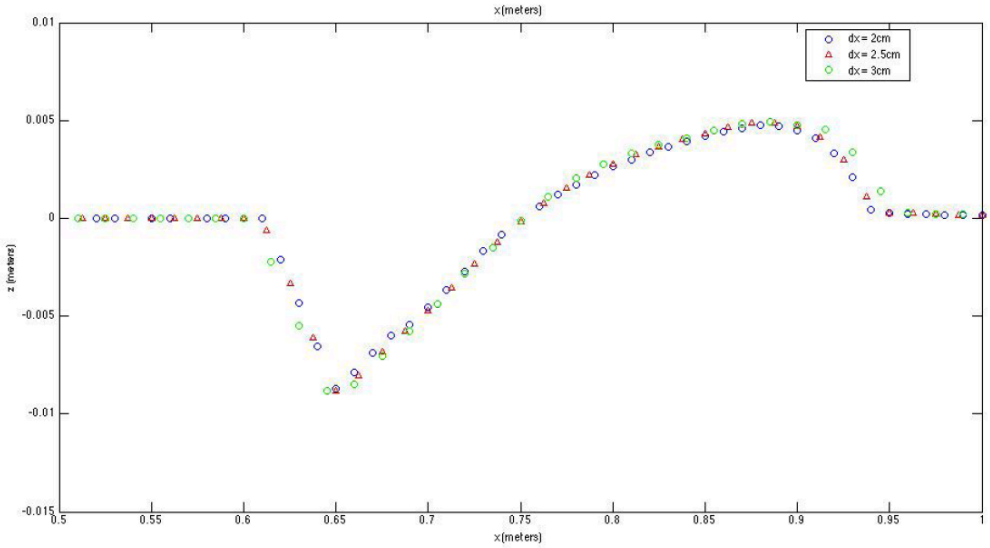

Figure 4.33: Simulation results for scouring from impinging horizontal jet, with three different grids; blue circles belong to the 2cm characteristic length grid; red triangles to the 2.5cm one and green circles to the 3cm one. It can be seen that at these grid resolutions there is no significant difference

It can be seen in the figure that there is no significant difference between the three grid sizes. The scouring depth is approximately 30% of what we would expect from experiment for the same time duration. Furthermore, in the simulation scouring ceases halfway through, because the stresses on the bed fall below the critical value, based on the Shields criterion. This can be seen in figure 4.34 where the Shields stress is plotted after scouring has taken place for five minutes.

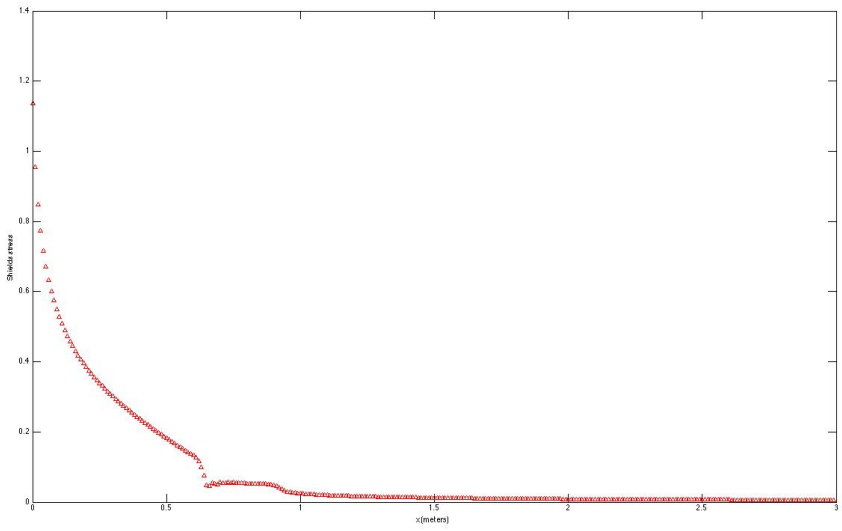

Figure 4.34: Plot showing the Shields stress as a function of distance from the jet exit, after scouring has taken place for five minutes; the stress values have dropped below critical level at the location where the movable bed starts and beyond, and no more scouring is taking place

Extending the simulation time does not make any difference in the depth of scouring, since that has ceased to occur within the first five minutes of flow. It was found that increasing the jet velocity and, as such, the stresses on the bed, played only a small role in the depth of scouring, which remained well below experimental values. Again, scouring stopped taking place within the first five minutes of flow. Figure 4.35 shows a close-up of the flow field near the location of the jet exit and where scouring has taken place. It also shows how the model works in increasing or reducing the size of the grid by adding or removing computational cells from the boundary.

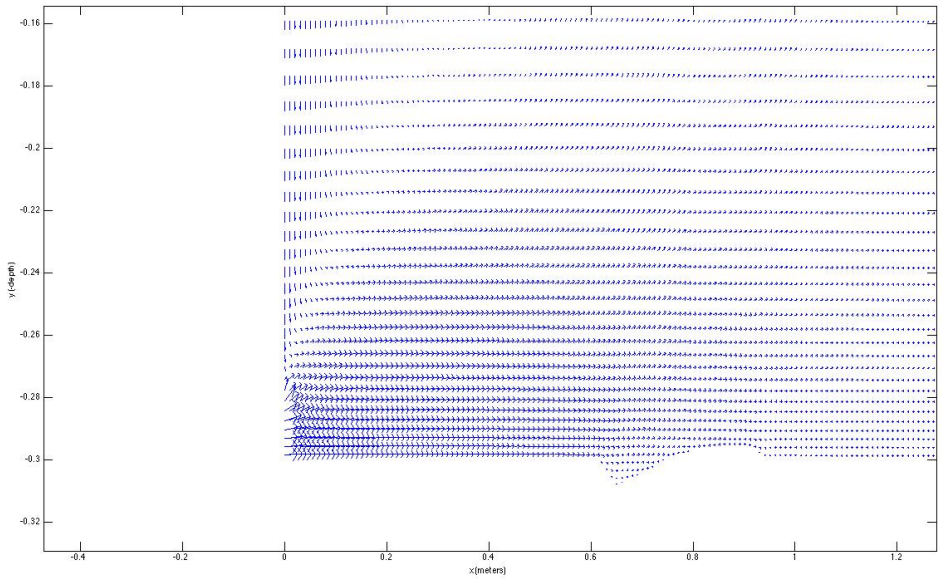

Figure 4.35: Flow-field near the location of the jet exit. Depicted are the flow velocity vectors. There is no recirculation in the location of the scoured bed

The plot of the flow field shows no recirculation in the pocket created by scouring. In Garcia's model [65], a recirculation zone is created in the hole that is dug out. This can be seen in figure 4.9 given above, which plots the flow field in Garcia's model. It is not clear if Garcia's model accurately captures the flow field. If it does, it is interesting that the recirculating flow moves opposite to the direction of the average flow. This would imply that material is picked up by the recirculating flow and is entrained in the flow above the recirculation zone, which then deposits it further downstream. Garcia's model implemented entrained sediment transport as well as bedload transport, and the former mode of transport could capture the pickup and deposition process, in a way that accurately reproduced the final bed morphology. However, the exact physics of the pickup and deposition mechanism do not point to a passive scalar mode of transport, irrespective of whether Garcia was able accurately reproduce the final morphology in the experiments by Chatterjee [66]. The Rouse number is above 2.5 in the scouring region, and any pickup and deposition

would amount to long-distance saltating particles rather than passively entrained fine sediment. A Lagrangian approach for tacking the trajectory of particles would best suit the physics of the problem. In that case, even if Suntans captured the recirculation region of the flow field, the transport model developed in this thesis would not be able to capture the precise physics of the movement of sediment in the scour hole.

4.2.4.1 Conclusions

While the results of the attempt to validate the bedload transport model are disappointing, it is evident that the source of error lies not in the bedload transport model but in the fact that the hydrodynamic model does not accurately capture the flow dynamics in the particular case, at least not at the level of grid refinement implemented. Finer grids were tested, but the hydrodynamic model proved to be unstable even at very small time steps. A problem with the hydrodynamic model that has already been mentioned is that at very high grid resolutions, even slight changes in the free surface can cause the water level to drop below the height of cells at the top layer, causing the code to become unstable. To counteract this an attempt was made to run the simulation in a rigid lid configuration, by setting the acceleration of gravity to very high values, but the code still proved unstable. Nonetheless, while the hydrodynamic model failed to accurately reproduce the flow field in this particular case, the transport model was consistent in following the stress levels on the bed. It is not clear whether the RANS model used, or any RANS model for that matter, can accurately reproduce the flow field in this two-dimensional case. The fact, though, that in none of the three grids used was there a recirculation zone implies that the particular RANS model is not well suited. A reason for that could be that the Mellor and Yamada model rests on an anisotropic turbulence assumption which does not hold in the particular case.

Finally, had the recirculation zone been captured by Suntans, the bedload transport model in this work would not be able to capture a complex pickup-and-deposition phenomenon that would require particle trajectory tracking using a Lagrangian approach for particles moving in the flow field in a non-passive manner. The reason this particular case was used for validation is that it was the only case that could remotely be handled in terms of computational load and simulation times. As pointed out, the time steps required for stability in small scale simulations by Suntans prohibit the use for validation of any of the other cases described in the literature.

Considering the fact that there are no actual-scale experimental data it is not clear to what extent the bedload transport model can be validated, at least when coupled with the Suntans hydrodynamic model in actual scales. On the other hand, and as pointed out above, small-scale experiments on scouring do not exactly correlate with large scale phenomena. The flow parameters, Reynolds number and Froude number, that govern flow patterns in rivers, differ by orders of magnitude between experimental scales and full-blown-river scales. It would be physically impossible to achieve dynamic similarity in terms of flow and at the same time match Rouse numbers between small scale experiments and actual scales. The only true way then to validate the bedload transport model in this work, provided the hydrodynamic model is validated, is to compare it with field observations that involve scouring. Field observations of such accuracy do not exist.

CHAPTER V

Results

The flow rate through the St Clair River fluctuates depending on the season. It can be as low as $4200m^3/s$ in the winter and can be as high as $5500m^3/s$ in the summer [79]. The difference in water levels between Lake Huron and Lake St. Clair stays approximately the same at 1.6 meters. What mostly causes the variation in flow rates is the water levels in the two lakes, and as such in St. Clair River. In other words, the river is deeper during the summer months. This can be seen in the graphs in figure 5.1 (black lines), which were obtained from GLERL's (Great Lakes Environmental and Research Laboratory) website, and show water levels in Lakes Huron and St. Clair. The same graphs, however, show that there can be significant variation in water levels over the years (red and green lines).

A grid was created of the St. Clair River, with approximately 50,000 elements in the horizontal and a total of approximately 600,000 cells. The horizontal characteristic length of the grid was 55 meters and the vertical approximately 1 meter. The grid can be seen in figure 5.2.

The two lakes that the grid connects have been modeled as wide openings at the respective ends. The goal is for the openings to be wide enough so that flow velocities can be considered negligible at the open boundaries, as will be explained below. The estuary where St. Clair River opens in Lake St. Clair has been omitted from the grid,

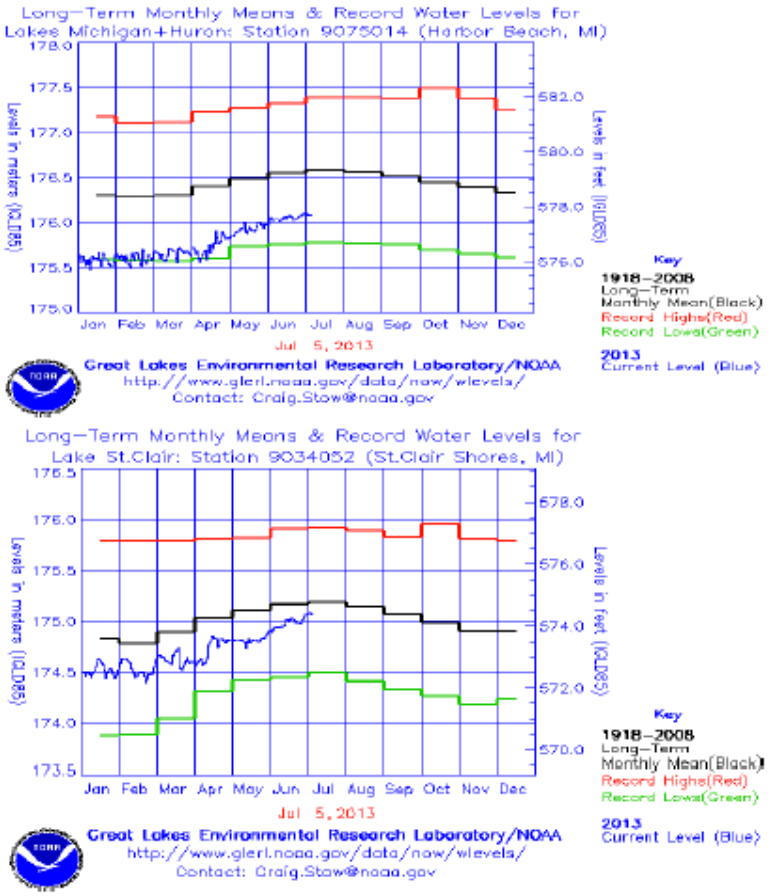

Figure 5.1: Water level fluctuations in Lakes Huron (top) and St. Clair (bottom); black lines give average values

because it would add unnecessary complexity to the geometry of the problem without affecting the hydrodynamic behavior of the system. The water level drop from the entrance to the exit of the estuary is 0.2 meters, so in the boundary conditions, the water level difference is 1.4 meters instead of 1.6 meters. Bathymetric data were obtained from GLERL, NOAA, [79] in the form of latitude and longitude versus depth. The latitude/longitude were converted to Cartesian coordinates in Matlab. The model has a built-in interpolation function that sets depths at the Voronoi points of the grid triangles, based on any $x - y - z$ data file. A figure of the grid showing the depths at various parts of the river can be seen in figure 5.3.

The depths vary from approximately 10 meters to spots where the water can be

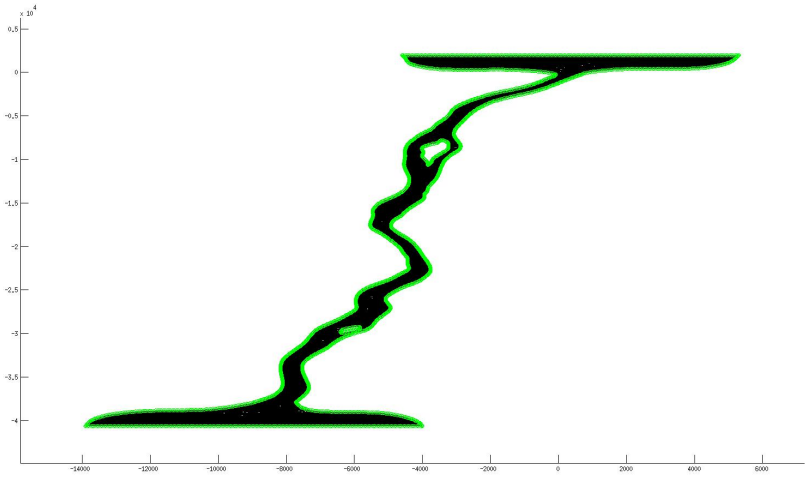

Figure 5.2: Computational grid. The entrance and exit have been widened to simulate hydro-dynamically the lake openings. The scale of the abscissa is greater than that of the ordinate

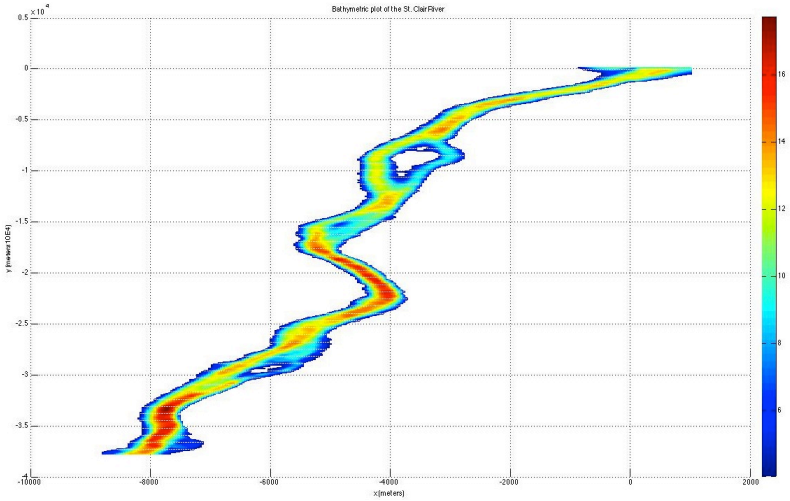

Figure 5.3: Bathymetric plot of the St. Clair River. Deeper parts of the river are colored in red

as deep as 17 meters. Points were added to the bathymetric data that assign depths in the openings at Lakes Huron and St. Clair.

The 1984 ice jam event took place in the month of April. The flow rate was approximately $4800m^3$, which agrees with annual flow variation. Open water flow simulations were carried out and the steady state flow rate was adjusted by varying the depth of the whole river to match the $4800m^3/s$ figure. It was found that adding 0.15 meters of depth to the bathymetric data gave the desired flow rate with reasonable

accuracy ($4834m^3/s$). The need for only a slight adjustment to the depth data in order to achieve an average flow rate is an indication of both accuracy of the bathymetric data, as well as accurate capturing of the flow dynamics by the model. The sediment grain size distribution along the river has been studied [78] and has been given in figure 4.15. These values were used in the movable bed model and a linear plot of the size distribution employed can be seen in figure 5.4.

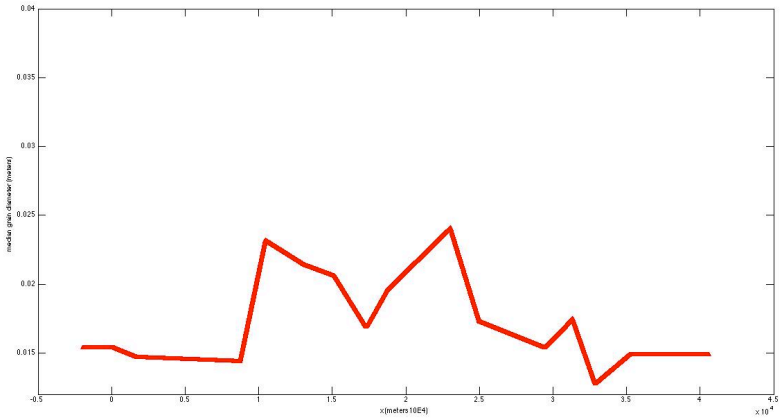

Figure 5.4: Grain size distribution as used in the model along the St. Clair River thalweg. The distribution used was taken and linearized from published data [78] (figure 4.15), in order to be computationally usable

For the river banks, as well as the banks in the two islands (Stag Island and Fawn Island), no-slip boundary conditions are set. For the river bed a drag law is applied, as has been described. The drag coefficient near the banks is set to a lower value that corresponds to finer grain size than that in the thalweg (5.4). This is in accordance to the grain size distribution in St. Clair River, with the banks having finer sediment on the bed [78]. For the entrance and exit, water levels are set and the flow velocities in the open boundary cells are set to zero. The physical interpretation of this boundary condition is that flow velocities become negligible well into the lakes, and water is gradually accelerated from zero at the entrance, and gradually decelerated to negligible values at the exit. This is the reason that the grid entrance and exit are made so wide. Zero traction is set at the free surface, since wind-induced

stresses are not taken into account. A 5 second time step is used. The stresses on the bed were computed under normal flow conditions and are plotted in figure 5.5.

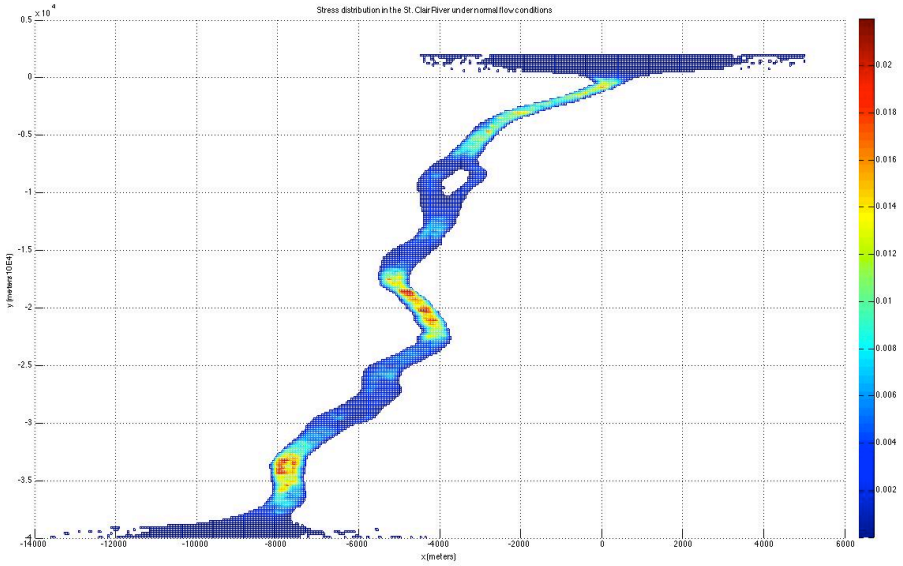

Figure 5.5: Stress distribution (Shields stress values) in the St. Clair River under normal flow conditions. There are three regions where stresses are elevated (yellow and red color) but below critical values

The results reveal three regions of elevated stresses on the river bed (red and yellow colors). The Shields stresses in all three parts are below critical values, but that is not the case during an ice jam release where the stresses locally exceed critical values, sometimes for extended periods of time. The regions of elevated stresses are a new finding and were not present in the results of the work by Kolerski and Shen [38], who used a 2D model based on the shallow water equations.

After simulating normal flow conditions, flow presence of an ice jam was simulated. The ice jam is modeled based on the 1984 ice jam [2]. A map showing the location of the jam before release is shown in figure 5.6.

Records show that during the last days of the jam, flow dropped by about 65% and the water level in Lake St. Clair dropped by approximately 0.6 meters. The boundary conditions then at the open boundaries were set to a 2 meter water level difference between Lakes Huron and St. Clair. These open boundary conditions were

Figure 5.6: Map showing the location of the 1984 ice jam. The upstream end of the jam almost reached St. Clair and the downstream end reached Algonac

maintained throughout the simulations of a jam release, because simulation times were short enough to assume that the water level in Lake St. Clair remained constant. With these boundary conditions the flow was adjusted by altering the thickness of the jam along its length until the flow was approximately $1700 m^3/s$. Figure 5.7 shows the flow field in a straight two-dimensional channel with a jam, the same length and thickness as the one constructed in the actual model. The constructed jam has a head thickness of 2 meters and a toe thickness of 4 meters.

The purpose of the figure is to show that the flow field in the model can be modified to account for the presence of an ice jam, or any stationary object in the flow field for that matter. The jam is simulated by setting the fluxes through the walls of the cells at the boundaries of the jam to zero, in which case the whole region of the flow field within the jam behaves as a stationary object. This can be seen in the figure 5.7, where the flow field in the region taken by the jam is zero. Friction was added at the underside of the jam by imposing a drag law like in the case of the bed. Based on recent studies on ice-covered rivers [80] the drag coefficient for

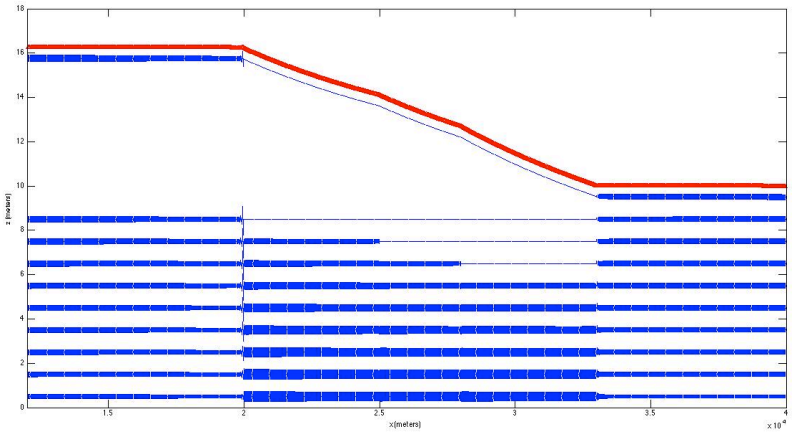

Figure 5.7: Flow field in a straight two-dimensional channel in the presence of an ice jam. The ice jam has the same length and thickness as the one in the model. The red line depicts the free surface

ice in a jam is given a value equal to 0.0025. Noticeable from the figure 5.7 is the smooth transition of the free surface (red line) between upstream and downstream of the jam water levels. This feature of the model captures reality more accurately when it comes to the release of the jam, than having an abrupt step-like transition like in early work on ice jam releases. Flow was simulated for 25000 seconds (6.9 hours) with the ice jam in place until steady state was achieved and the rate of discharge was stabilized at $1743 m^3/s$. Figure 5.8 shows the difference in stresses under normal flow conditions and in the presence of a stationary jam.

It can be seen in the figure that stresses under the jam are lower than during open water flow conditions, with the exception of the banks where there is a slight elevation in stresses, but not enough to warrant attention. The reason for the elevated stresses on the bed near the banks may be due to the lower friction that flow encounters there, because of the finer sediment and lower drag coefficient. Flow under the ice could be shifted near the banks because it encounters less friction. All in all, the result shows that, contrary to hypothesis [1] and previous findings [38], stresses under the jam and along the thalweg prior to release should be lower than under open water conditions, a finding that disproves the scenario that scouring could have taken place prior to

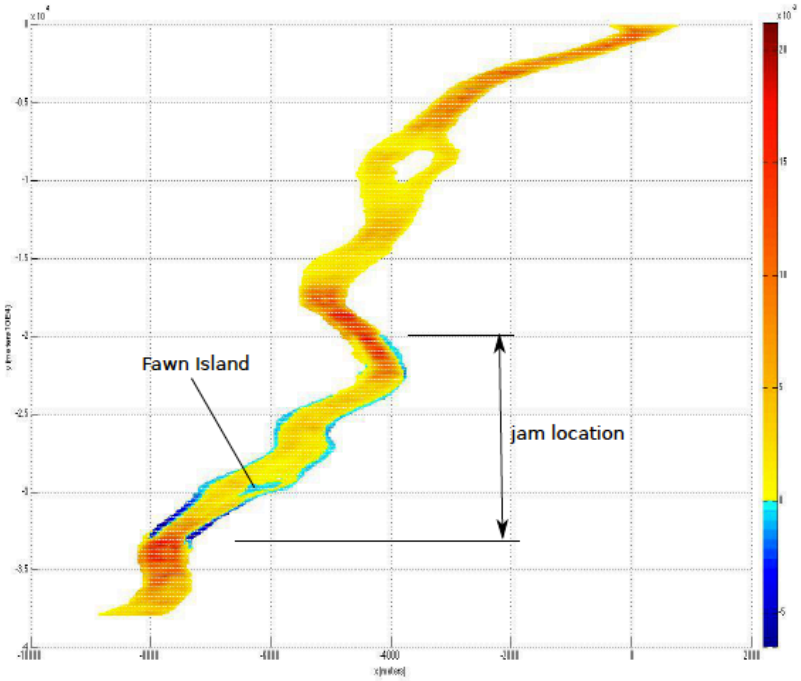

Figure 5.8: Plot showing the difference in Shields stress values between normal flow conditions and during the stationary jam; with the exception of the banks, stresses under the jam are lower (yellow or red color) than under normal flow conditions

release, as studied by Mercer [13].

The jam is released in the flow by removing the zero-flux restriction through the jam boundaries, as well as the enforced drag on the bottom surface of the jam. Essentially the jam release is simulated by releasing an initially stationary body of water into the flow. At the same time when the jam was released, the scouring model went into effect. Flow and scouring were allowed to continue for 25,000 more seconds. From field observations during the 1984 ice jam [2] it is known that the water level in Lake St. Clair was restored by 75% in the first four days following the release. Since the water level difference between Lakes Huron and St. Clair decreased with time, flow and scouring were allowed to occur under the initial boundary conditions for 6.9 hours after the release. Furthermore, it will be shown that for the case where the water level difference between entrance and exit is 2 meters, most scouring happens in the first 5000 seconds after the release. Figure 5.9 shows the evolution of the

stresses on the bed along the river with time. The stresses as a function of the x and y coordinates are projected on the $y - z$ plane, in order to produce a 3D figure showing evolution in time. The z axis shows stress levels.

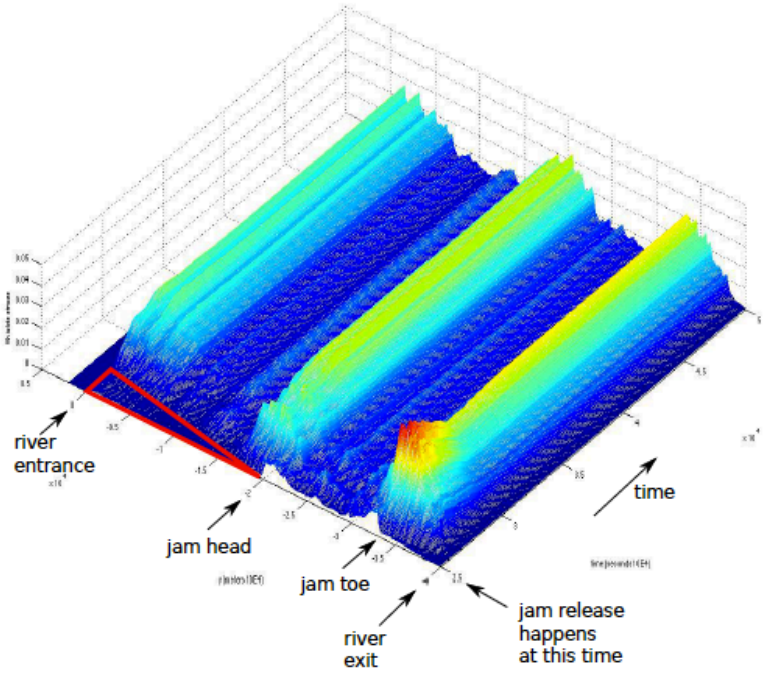

Figure 5.9: Evolution of bed stresses with time during jam release

There are certain things to note in figure 5.9. The three regions in the river that experience high stresses under normal flow conditions experience even more elevated stresses during the jam release. At the jam toe, there is a spike in stresses that subsides to lower values after approximately 2500 seconds. In all three regions stresses remain relatively high even after the initial surge, because the water level difference between the two lakes is higher than normal. This means that scouring can persist at certain locations, even after the initial surge. It takes more than 1000 seconds after the release for the stresses to spike at the location right below the jam toe. That location coincides with a location of elevated stresses under normal flow conditions, which become much higher during the surge. The time lag means that it takes time for the initially still mass of water to accelerate to appreciable values.

Then the assumption that ice in a jam release will accelerate very quickly to water flow values [9] does not hold. In the figure it can also be seen that following the release of the jam, an upstream-moving wave propagates originating at the head of the jam (red triangle). The wave covers approximately 30 kilometers in 2500 seconds, with an approximate speed of $12m/s$. This corresponds to a wave traveling in a straight channel of approximate depth of 15 meters, according to open channel flow theory. This is close to average depths in St. Clair River. Figure 5.10 shows the change in depth 25,000 seconds after the jam release. Blue colors signify scouring and red colors deposition. From the figure it can be seen that there is localized scouring near the river entrance. There is also a region in the central portion of the river with several locations where there is scouring intermingled with deposition. Most importantly there is a region of extensive scouring near the exit of the river (green and blue color). It can be seen from the figure that scouring in that region extends several kilometers and occupies the central portion along the width of the river, while there is deposition close to the banks. A net amount of approximately 9000 m^3 of bedload material are displaced during the period of scouring that was simulated.

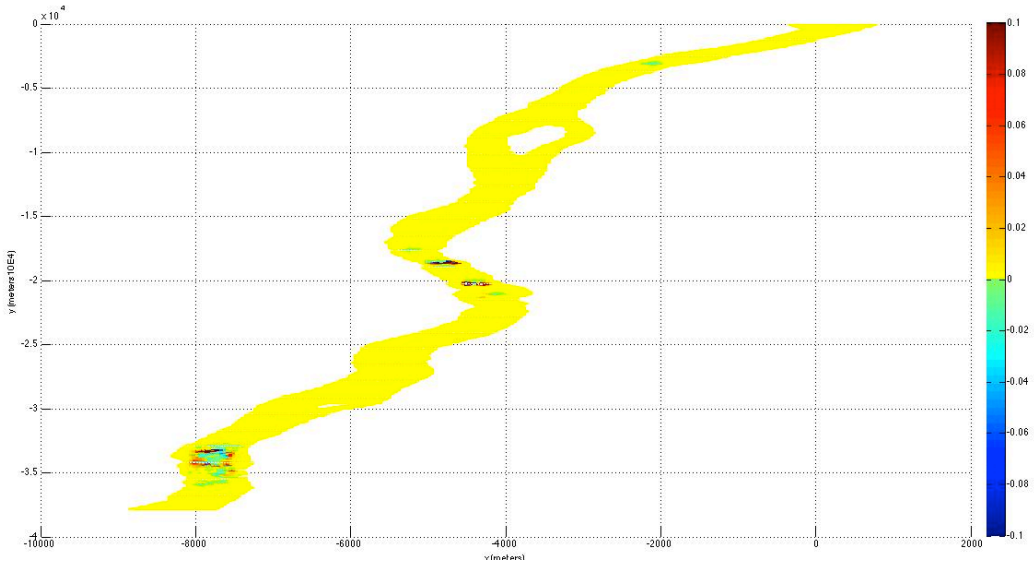

Figure 5.10: Difference in initial and final depth after jam release in St. Clair River. Blue and green colors show scouring and red deposition

Figure 5.11 shows depth change, but with blue and green colors showing scouring more than 1 centimeter in depth. It can be seen in the figure that significantly smaller regions experience scouring more that 1 centimeter in depth.

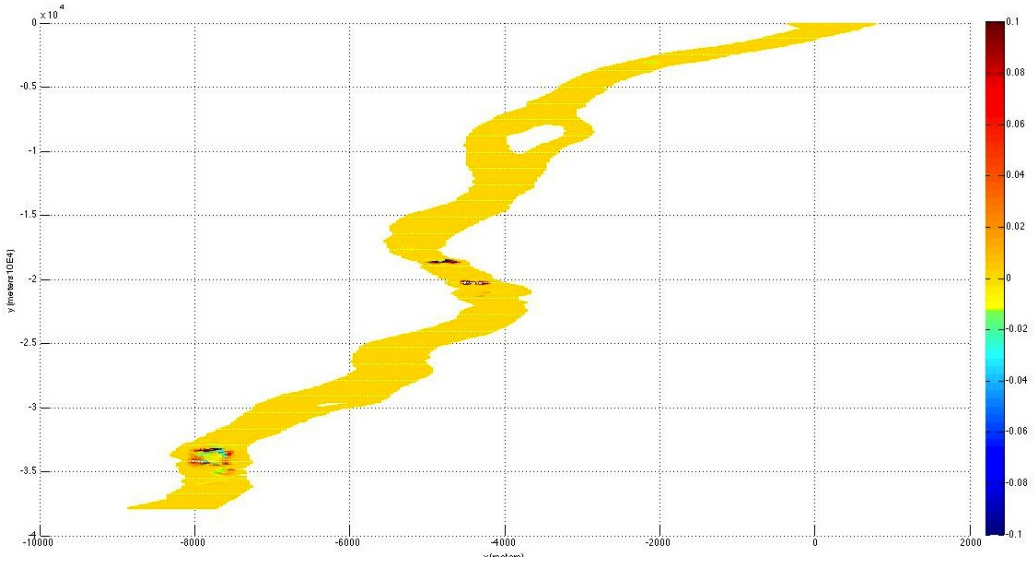

Figure 5.11: Difference in initial and final depth after jam release in St. Clair River. Blue and green regions show scouring more than 1 centimeter in depth

Figure 5.12 shows scouring that happens after the initial surge, due to persisting high flows. This is scouring that happens between 30,000 and 50,000 seconds, the jam released at 25,000 seconds. Blue regions in the figure show scouring more than 1 centimeter in depth. It is seen that scouring continues after the initial surge. This is an important finding because it means that, surge aside, the high flows due to the higher-than-normal water level difference between Lakes Huron and St. Clair can lead to scouring. The 1984 ice jam lasted for 24 days, during which the water level in Lake St. Clair dropped by 0.6 meters. Lake St. Clair is a small lake and an imbalance between inflow and outflow caused by a jam can cause water levels to drop quickly, unlike Lake Huron whose water level was not affected during the 1984 jam. As will be seen below, an even greater drop in the water level in Lake St. Clair would lead to extensive scouring during and after a jam release.

A scenario was tested where the water level drop in Lake St. Clair was 1 meter

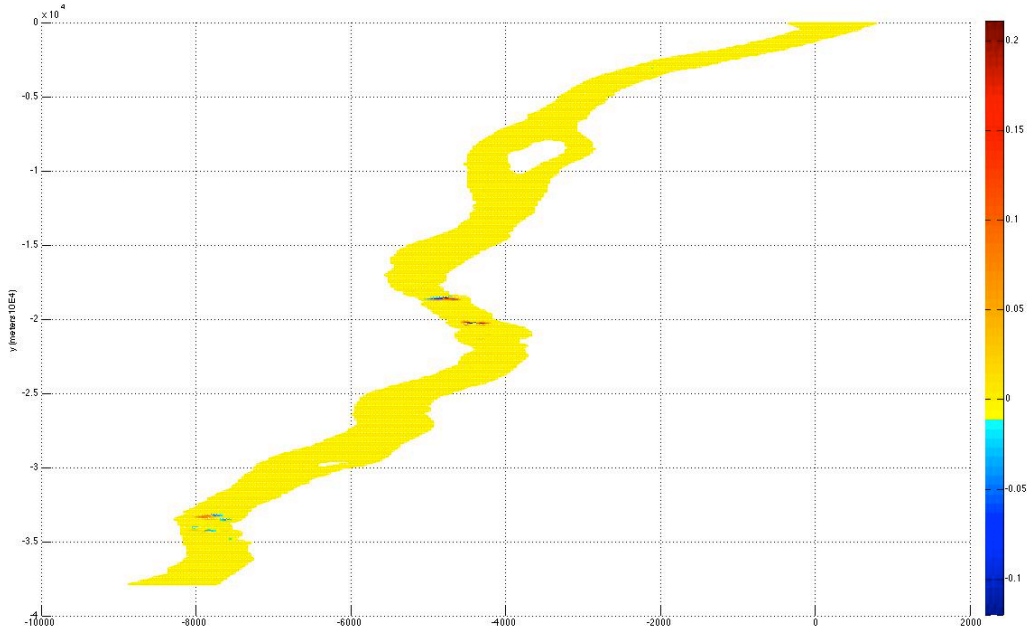

Figure 5.12: Scouring happening after the initial phase of the jam release; blue regions indicate scouring more than 1 centimeter in depth

instead of 0.6 meters. That could happen if a jam persisted longer than 24 days which was the duration of the 1984 ice jam. The boundary conditions were set so that the water level at the entrance was 2.4 meters higher than that at the exit, and flow was simulated until steady state was achieved. The size and shape of the jam were left unaltered. Then the jam was released. Flow was simulated for 12,500 seconds after the release, a shorter duration than in the previous run. The duration was kept shorter because it is assumed that the very high flow velocities will cause the water level in Lake St. Clair to rise very rapidly, invalidating the boundary conditions set in the onset of the simulation. Figure 5.13 shows the evolution of the stresses on the river bed with time, in a similar fashion as in figure 5.9. Most notably, the stresses at the locations of high-stress concentration under normal flow conditions are significantly higher and the high values persist with time. This, again, is because irrespective of the initial surge the flows remain high due to the big water level difference between the two lakes. The high flows lead to scouring after the initial surge.

Figure 5.14 shows the depth changes that have taken place 12,500 seconds after

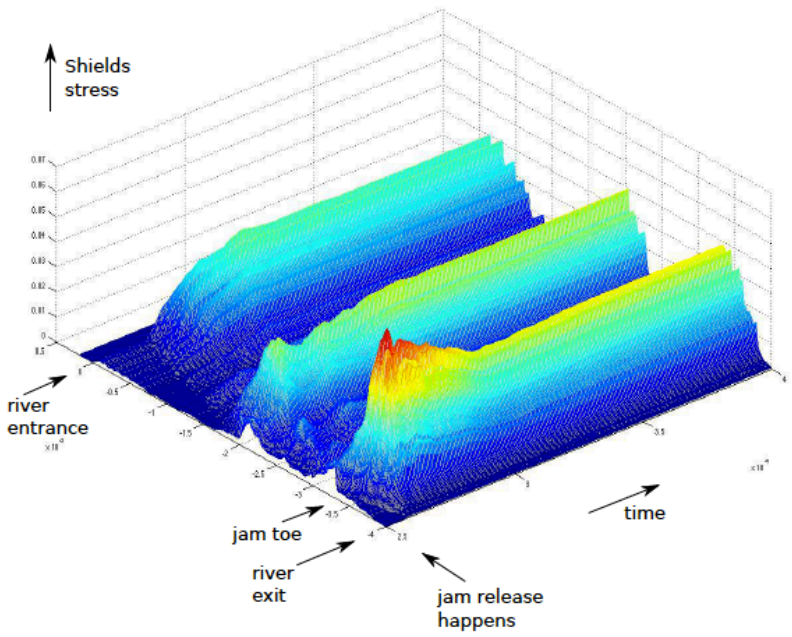

Figure 5.13: Evolution of bed stresses with time during jam release; this time the difference in water level between the two lakes is even greater

the jam release. The blue and green regions show scouring more than 1 centimeter in depth. Again, there is a small region of scouring in the upper portion of the river, while there are several small regions where scouring has taken place in the central part of the river. Extensive scouring has taken place in the lower part of the river near the exit, right below the jam toe. The scouring stretches for approximately 3 kilometers along the river, and covers large areas of the central portion along the width.

Figure 5.15 shows scouring that has taken place starting 5000 seconds after the release, after the surge has passed. Blue regions indicate scouring more than 1 centimeter in depth. While lesser scouring takes place after the initial surge has passed, it is still significant and at locations can exceed 10 centimeters in depth (not seen in the figure). It is worth noting that this is scouring that takes place during 7500 seconds of flow (2.1 hours). Considering the fact that it would take days for the water level in Lake St. Clair to rise to levels where there is no more scouring taking place in the St. Clair River, the degree of scouring that takes place during the entire process,

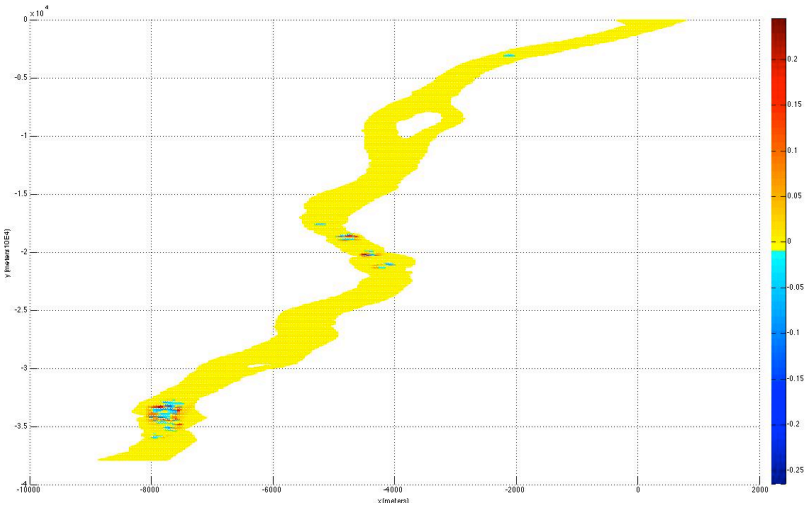

Figure 5.14: Difference in initial and final depth after jam release in St. Clair River. Blue and green regions show scouring more than 1 centimeter in depth. This time the water level difference between the two lakes was 2.4 meters

which can be several tenths of a meter in depth, can have a significant impact on the hydrodynamics of the system. This applies to a lesser extent to the 1984 ice jam, although the lower initial water level differences between the two lakes would mitigate the phenomenon.

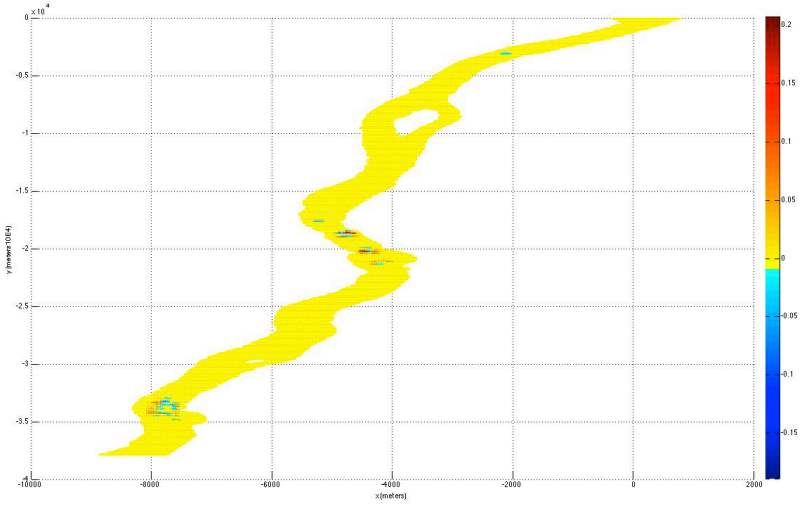

Figure 5.15: Scouring happening after the initial phase of the jam release; blue regions indicate scouring more than 1 centimeter in depth. This time the water level difference between the two lakes was 2.4 meters

5.0.5 Conclusions

Flow in the St. Clair River was simulated both for normal open water conditions and for conditions when an ice jam, similar to the 1984 ice jam in size and in the effect that it had on the flow, is present. Normal flow simulations revealed three regions of elevated stresses on the bed, one near the entrance, one in the central portion of the river and one near the exit. During the release of an ice jam stresses in those parts are even more elevated and exceed critical values. This finding is based purely on the hydrodynamic model, and indicates that scouring will take place irrespective of the accuracy of the movable bed model. Application of the movable bed model indicates that significant scouring would have taken place during the 1984 ice jam, especially near the exit of the river right below the toe of the jam. This scouring amounts to several thousands cubic meters of sediment displaced from the central portions along the width of the river towards the banks. Significant amounts of scouring would have occurred after the initial phase of the release, once the surge had passed. This is because of the high water level difference between the two lakes that existed right before the release of the jam. A test scenario was run where the water level in Lake St. Clair drops by an additional 0.4 meters. Referring to figure 5.1 showing water level fluctuations in the lake, this scenario is possible and could happen if a jam like the 1984 ice jam stayed in place for more than 24 days. Significant scouring happens in a short period of time after the release and continues thereafter until the water level in Lake St. Clair rises to pre-jam levels. Under these conditions the total amount of scouring could have very pronounced effects on the hydrodynamics of the system. It has to be stressed, however, that while the model gives strong indications that scouring will happen in an event like the one in 1984, since the movable bed model has not been validated, it is still uncertain how exactly the bed morphology will change. Furthermore, the sensitivity of the system to localized changes in bed morphology has yet to be ascertained. A 10 cm drop in the water level of Lake

Huron over the last 25 years amounts to an average increase in river conveyance by approximately 1.5 m^3/s. Compared to the average volume flow rate through the river of approximately 4800 m^3/s, this is a very slight increase. A highly non-liner system like the Huron Erie Corridor could be sensitive to even minute, localized changes in bed morphology when it comes to very small increments in conveyance.

5.0.6 Future Work

While attempts to validate the movable bed (bedload transport) model were unsuccessful, this is due to weaknesses of the hydrodynamic model and related computational difficulties as was shown. Because the hydrodynamic model is unsuitable for small-scale simulations, the best approach to validate the movable bed model would be to incorporate it in a different hydrodynamic model, unless validation cases arise involving larger scale phenomena. A continuous sediment size distribution was used in this study, but more detailed information on the sediment composition of the bed could be incorporated. A more accurate model for scouring would involve variation of sediment composition with depth, as well as accounting for sediment size changes brought about by movement of bedload of a certain size to locations whose sediment size profiles are different. Analytical formulas accounting for changing sediment composition because of sediment transport have been developed [81], [75], [76] and involve an evolving grain size distribution at each location, as well as accounting for relative mobilities between different grain sizes. It would be a simple matter to incorporate these changes in the bedload transport model. More difficult would be to obtain detailed information on the river bed. The entire Huron Erie Corridor (HEC) system should be incorporated in one model and simulations should be run involving scouring and potential changes in the amount of water drained from Lakes Huron-Michigan. While in this study it is shown that scouring will happen in a 1984 ice jam scenario, any longterm impacts on the water level of Lake Huron cannot be

studied unless flow simulations are run that treat the HEC in its entirety. Provided that the scouring model is validated and gives accurate results, the sensitivity of the entire system to even minute changes in the river bed morphology can be investigated. Considering the non-linearity of the system, as well as the only very slight increase in river conveyance needed to bring about the recorded change in the water level of Lake Huron over time, it is an intriguing question whether a localized change in bed morphology can bring about such a change. If such a phenomenon can occur, it will be the equivalent of the 'butterfly' effect for the Huron Erie Corridor. Finally, more extreme worst case scenarios should be tested. Referring to figure 5.1 it is plausible that under unusual conditions the water level difference between Lakes Huron and St. Clair can reach 3 meters. The impact of such extreme events should and could be investigated. All of the above tasks are within reach using Suntans, provided the movable bed model is modified to account for changing surface sediment composition and is validated.

APPENDICES

APPENDIX A

Nomenclature

Symbol	Description
ω_s	fall velocity
κ	Von Karman's constant
u_*	friction velocity
R	submerged specific gravity
g	acceleration of gravity
D	diameter of sediment particle
ν	kinematic viscosity of water
ν_V	vertical turbulent viscosity
$C_{d,B}$	bed drag coefficient
τ_w	wall stress
ρ	density of water
y^+	wall unit
H	water depth
k_s	Nikuradse roughness coefficient
d_{85}	85th percentile sediment grain diameter
d_{50}	50th percentile sediment grain diameter

s	specific gravity of sediment particle
β	angle of inclination of bed
η	bed elevation
n	sediment porosity (note that in the literature review n stands for Manning's n; in this work however it is used for porosity)
$\vec{q}$	bedload flux vector
q_i	bedload flux vector component
τ_i	component of stress on the bed vector
$\vec{\tau}$	stress on the bed vector
q_o	bedload flux vector for horizontal bed

BIBLIOGRAPHY

BIBLIOGRAPHY

[1] T.R. Yuzyk, E.Z. Stakhiv et al. "Impacts on Upper Great Lakes Water Levels," *International Upper Great Lakes Study, International Joint Commission*, 2009.

[2] J.A. Derecki and F.H. Quinn "Record St. Clair River Ice Jam of 1984" *Journal of Hydraulic Engineering*, vol. 112, no. 12, pp. 1182-1194, 1986.

[3] S. Beltaos, "River Ice Jams," Water Resources Publications, Highlands Ranch, CO, 1995.

[4] E. Ettema and R.W. Kempera, "River-Ice Effects on Gravel Bed Channels," *7th Gravel-Bed Rivers Conference*, Tadoussac, Quebec, 2010.

[5] L.J. Zabilansky, R. Ettama, J. Wuebben, and N.E. Yankelium, "A Survey of River-Ice Influences on Channel Bathymetry along the Fort Peck Reach of the Missouri River, Winter 1998-1999," Contract Report, U.S. Army Corps of Engineers, Cold Regions Research and Engineering Laboratory, Hanover, NH, 2002.

[6] M. Jasek, "Ice-Jam Release and Break-Up Front Propagation," *Proceedings of the 12th Workshop on the Hydraulics of Ice Covered Rivers, CGU HS Committee on River Ice Processes and the Environment*, Edmonton, AB, pp. 348-368, 2003.

[7] S.A. Schumm and H.R. Khan, "Experimental Study of Channel Patterns," *Geological Society of America Bulletin* vol. 83, pp. 1755-1770, 1972.

[8] F.M. Henderson and R. Gerard, "Flood Waves Caused by Ice Jam Formation and Failure," *Proceedings of the International Association for Hydraulic Research Symposium on Ice*, Quebec City, Quebec, pp. 277-297, 1981.

[9] S. Beltaos and B.G. Krishnappan, "Surges Form Ice Jams: A Case Study," *Canadian Journal of Civil Engineering*, vol. 9, no. 2, pp. 276-284, 1982.

[10] I. Joliffe and R. Gerard, "Surges Released by Ice Jams," *Proceedings of the Workshop on Hydraulics of Ice-Covered Rivers*, Edmonton, Alta. Compiled by D. D. Andres and R. Gerard. National Research Council of Canada, Ottawa, Ont., pp. 253-259, 1982.

[11] F.M. Henderson "Open Channel Flow", McMillan, New York, 1966.

[12] P.F. Doyle and D.D. Andres "1979 Spring Breakup and Ice Jamming on the Athabasca River Near Fort Mc-Murray" *Report SWE-79-05*, Alberta Research Council, Edmonton, Alta., 1979.

[13] A.G. Mercer and R.H. Cooper "River Bed Scour Related to the Growth of a Major Ice Jam," *Proc. 3rd Canadian Hydrotechnical Conference*, Canadian Society of Civil Engineering, Quebec City, Canada, pp. 291-308, 1977.

[14] E. Pariset, R. Hausser and A. Gagnon "Formation of Ice Covers and Ice Jams in Rivers" *ASCE, Hydraulics Division Journal*, vol. 92, no. 6, 1966.

[15] B. Michel "Winter Regime of Rivers and Lakes" *U.S. Army Corps of Engineers*, Cold Regions Research and Engineering Laboratory, Hanover, New Hampshire, 1971.

[16] B. R. Colby "Relationship of Sediment Discharge to Streamflow" *U.S. Department of the Interior, Geological Survey, Water Resources Division*, 1956.

[17] J. Wong, S. Beltaos and B.G. Krishnappan "Laboratory Tests on Surges Created by Ice Jam Releases" *Canadian Journal of Civil Engineering*, vol. 12, no. 4, pp. 930-933, 1985.

[18] F. Hicks, K. McKay and Shabayek "Modeling an Ice Jam Release Surge on the Saint John River, New Brunswick" *Proceedings of the 1997 Workshop on River Ice*, Committee on River Ice Processes and the Environment, Hydrology Section, Fredericton, N.B. Canadian Geophysical Union, Sidney, B.C. pp. 174-184, 1997.

[19] J. L. Wuebben, D. S. Deck and J. E. Zufelt "Ice Jam Flood Assessment for the St. John River Basin, Aroostook County, Maine" *Special Report 95-15, U.S. Army Corps of Engineers*, Cold Regions Research and Engineering Laboratory, Hanover, New Hampshire, 1995.

[20] F.E. Hicks and P.M. Steffler "Characteristic Dissipative Galerkin Scheme for Open Channel Flow" *Journal of Hydraulic Engineering*, American Society of Civil Engineers, vol. 118, no. 2, pp. 337-352, 1992.

[21] F. H. Quinn and E.B. Wylie "Transient Analysis of the Detroit River by the Implicit Method" *Water Resources Research*, vol. 8, no. 6, pp. 1461-1469, 1972.

[22] F. H. Quinn and J.C. Hagman "Detroit River and St. Clair River Transient Models" *NOAA Technical Memo*, ERL GLERL-14, GLERL, Ann Arbor, Michigan, 1977.

[23] F.H. Quinn "Wind Stress Effects on Detroit River Discharges" *Journal of Great Lakes research*, vol. 6, no. 2, 172-175, 1980.

[24] J.A. Derecki and R.N. Kelley "Improved St. Clair River Dynamics Flow Models and Comparison Analysis" *NOAA Technical Memo*, ERL GLERL-34, GLERL, Ann Arbor, Michigan, 1981.

[25] D.J. Schwab, J.R. Bennett and A.T. Jessup "A Two-dimensional Lake Circulation Modeling System" *NOAA Technical Memo*, ERL GLERL-38, GLERL, Ann Arbor, Michigan, 1981.

[26] D.J. Schwab, A.H. Clites, C.R. Murthy, L.A. Meadows and G.A. Meadows "The Effect of Wind on Transport and Circulation in Lake St. Clair" *Journal of Geophysical Research*, vol. 94, no. 4, pp. 4947-4958, 1989.

[27] I.K. Tsanis, H. Shen and S. Venkatesh "Water Currents in the St. Clair and Detroit Rivers" *Journal of Great Lakes Research*, vol. 22, no. 2, pp. 213-223, 1996.

[28] K.A. Ibrahim and J.A. McCorgquodale "Finite Element Circulation Model for Lake St. Clair" *Journal of Great Lakes Research*, vol. 11, no. 3, pp. 208-222, 1985.

[29] T.J. Simons and W.M. Schertzer "Modeling Wind-induced Water Setup in Lake St. Clair" *Journal of Great Lakes Research*, vol. 15, no. 3, pp. 452-464, 1989.

[30] D.J. Holtschlag and J.A. Koschik "A Two-dimensional Hydrodynamic Model of the St. Clair-Detroit River Waterway in the Great Lakes Basin" *Water-Resources Investigations Report No. 01-4236*, USGS, Lansing, Michigan, 2002.

[31] C. Chen, H. Liu and R.C. Beardsley "An Unstructured Grid, Finite-Volume, Three-Dimensional, Primitive Equations Ocean Model: Application to Coastal Ocean and Estuaries" *Journal of Atmospheric and Oceanic Technology*, vol. 20, no. 1, pp. 159-186, 2003.

[32] E.J. Anderson, D.J. Schwab and G.A. Lang "Real-Time Hydraulic and Hydrodynamic Model of the St. Clair River, Lake St. Clair, Detroit River System" *Journal of Hydraulic Engineering*, vol. 136, no. 8, pp. 507-518, 2010.

[33] J. Blackburn and F. Hicks "Suitability of Dynamic Modeling for Flood Forecasting During Ice Jam Release Surge Events" *Journal of Cold Regions Engineering*, vol. 17, no. 1, pp. 18-36, 2003.

[34] L.W. Liu and H.T. Shen "Dynamics of Ice Jam Release Surges" *Proceeding of the 17th International Symposium on Ice*, St. Petersburg, Russia, 2004.

[35] H.T. Shen, J. Su and L.W. Liu "SPH Simulation of River Ice Dynamics" *Journal of Computational Physics*, vol. 165, no. 2, pp. 752-770, 2000.

[36] M. Jasek "Ice jam release and break-up front propagation" *12th Workshop on the Hydraulics of Ice Covered Rivers*, Edmonton, AB, June 2003.

[37] Y. She and F. Hicks "Incorporating Ice Effects in Ice Jam Release Surge Models" *13th Workshop on the Hydraulics of Ice Covered Rivers*, Hanover, NH, 2005.

[38] T. Kolerski and H.T. Shen "DynaRICE Modeling to Assess the Effect of the 1984 Ice Jam on Possible Bed Changes in the St. Clair River" *Report Submitted to the International Upper Great Lakes Study, International Joint Commission*, 2009.

[39] S. Beltaos "Potential Ice Impacts on the Conveyance of the St. Clair River" *Report prepared for Dr. S. Moin*, 2009.

[40] O. B. Fringer, M. Gerritsen, and R. L. Street "An Unstructured-Grid, Finite-Volume, Nonhydrostatic, Parallel Coastal Ocean Simulator" *Ocean Modelling*, vol. 14, no. 3-4, 139-173, 2006.

[41] V. Casulli and P. Zanolli "Semi-Implicit Numerical Modeling of Non-Hydrostatic Free-Surface Flows for Environmental Problems" *Mathematical and Computer Modeling*, vol. 36, pp. 1131-1149, 2002.

[42] W. Wu, W. Rodi and T. Wenka "3D Numerical Modeling of Flow and Sediment Transport in Open Channels" *Journal of Hydraulic Engineering*, vol. 126, no. 4, 2000.

[43] A. J. Odgaard and M. A. Bergs "Flow Processes in a Curved Alluvial Channel" *Water Resources Research*, vol. 24, no. 1, pages 45-56, 1988.

[44] H. Chanson "The hydraulics of open channel flow: An introduction" 2nd edn. Elsevier, Oxford, 2004.

[45] K. Whipple "Essentials of Sediment Transport" *Surface Processes and Landscape Evolution: Course Notes. MIT OpenCourseWare*, 2004.

[46] R. I. Ferguson and M. Church "A Simple Universal Equation for Grain Settling Velocity" *Journal of Sedimentary Geology*, vol. 74, pp. 933-937, 2004.

[47] A. Roulund, B. M. Sumer, J. Fredsoe and J. Michelsen "Numerical and experimental investigation of flow and scour around a circular pile" *Journal of Fluid Mechanics*, vol. 534, pp. 351- 401, 2005.

[48] J. Fredsoe and R. Deigaard "Mechanics of Coastal Sediment Transport" *Advanced Series on Ocean Engineering 3*, World Scientific, Singapore, 1992.

[49] T. W. Lambe and R. V. Whitman "Soil Mechanics" Wiley, 1969.

[50] N. Nagata, T. Hosoda, T. Nakato and Y. Muramoto "Three-Dimensional Numerical Model for Flow and Bed Deformation around River Hydraulic Structures" *Journal of Hydraulic Engineering*, vol. 131, no. 12, 2005

[51] M. Michiue and O. Hinokidani "Calculation of 2-Dimensional Bed Evolution Around Spur-Dike" *Annual Journal of Hydraulic Engineering*, vol. 36, pp. 61-66, 1992.

[52] B. W. Melville "Local Scour at Bridge Site" *Rep. No. 117*, School of Engineering, The Univ. of Auckland, New Zealand, 1975.

[53] B. W. Melville and A. J. Raudkivi "Flow Characteristics in Local Scour at Bridge Piers" *Journal of Hydraulic Research*, vol. 15, no. 4, pp. 373-380, 1977.

[54] www.risoe.dk/veaaed/numwind/flowsolver.htm

[55] F. Engelund and J. Fredsoe "A Sediment Transport Model for Straight Alluvial Channels" *Nordic Hydrology*, vol. 7, pp. 293-306, 1976.

[56] A. J. Raudviki "Loose Boundary Hydraulics" Taylor and Francis, 1st edition, 1998.

[57] B. B. Haws "Ability of ADV Measurements to Detect Turbulence Differences Between Angular and Rounded Gravel Beds of Intermediate - Roughness Scale" Brigham Young University, Department of Civil and Environmental Engineering, 2008.

[58] A. Khosronejad, C. D. Rennie, S. A. A. Salehi Neyshabouri and R. D. Townsend "3D Numerical Modeling of Flow and Sediment Transport in Laboratory Channel Bends" *Journal of Hydraulic Engineering*, vol. 133, no. 10, pp. 1123-1134, 2007.

[59] T. Matsura and R. Townsend "Stream-Barb Installation for Narrow Channel Bends - a Laboratory Study" *Canadian Journal of Civil Engineering*, vol. 31, pp. 478-486, 2004.

[60] L. C. Van Rijn "Sediment Transport. Part I: Bed Load Transport" *Journal of Hydraulic Engineering*, vol. 110, no. 10, pp. 1431-1456, 1984.

[61] J. G. Duan, S. S. Y. Wang and Y. Jia "The Applications of the Enhanced CCHE2D Model to Study the Alluvial Channel Migration Processes" *Journal of Hydraulic Engineering*, vol. 39, no. 5, pp. 1-12, 2001.

[62] J. G. Duan and P. Y. Julien "Numerical Simulation of the Inception of Channel Meandering" *Earth Surface Processes and Landforms*, vol. 30, no. 9, pp. 1093-1110, 2005.

[63] A. Sana and E. B. Shuy "Two-Equation Turbulence Models for Smooth Oscillatory Boundary Layers" *Journal of Waterway, Port, Coastal and Ocean Engineering*, vol. 128, no. 1, pp. 38-45, 2002.

[64] S. Kang, A. Lightbody, C. Hill and F. Sotiropoulos "High-Resolution Numerical Simulation of Turbulence in Natural Waterways" *Advances in Water Resources*, vol. 34, pp. 98-113, 2011.

[65] X. Liu and H. M. Garcia "Three-Dimensional Numerical Model with Free Water Surface and Mesh Deformation for Local Sediment Scour" *Journal of Waterway, Port, Coastal and Ocean Engineering*, vol. 134, no. 4, pp. 203-217, 2008.

[66] S. S. Chatterjee, S. N. Ghosh and M. Chatterjee "Local Scour Due to Submerged Horizontal Jet" *Journal Hydraulic Engineering*, vol. 120, pp. 973-992, 1994.

[67] B. Brors "Numerical Modeling of Flow and Scour at Pipelines" *Journal of Hydraulic Engineering*, vol. 125, no. 5, pp. 511-523, 1999.

[68] D. D. Apsley and P. Stansby "Bed-Load Sediment Transport on Large Slopes: Model Formulation and Implementation within a RANS Solver" *Journal of Hydraulic Engineering*, vol. 134, pp. 1440-1451, 2008.

[69] S. Kawai and P. Julien "Point bar deposit in narrow sharp bends" *Journal of Hydraulic Research*, vol. 34, no. 2, pp. 205-218, 1996.

[70] A. Khosronejad, K. Seokkoo, I. Borazjani and F. Sotiropoulos "Curvilinear Immersed Boundary Method for Simulating Coupled Flow and Bed Morphodynamic Interactions Due to Sediment Transport Phenomena" *Advances in Water Resources*, vol. 34, pp. 829-843, 2011.

[71] M. R. Pirestani "Experimental Study of Flow Pattern in U-Shape Bend Channel" *The 9th International Symposium on River Sedimentation*, Yichang, China, 2003.

[72] L. C. Van Rijn "Principles of Sediment Transport in Rivers, Estuaries and Coastal Seas" Aqua Publications, 1993.

[73] E. Meyer-Peter and R. Muller "Formulation for Bed Load Transport" *2nd Congress, International Association of Hydraulic Research*, Stockholm, 1948.

[74] P. R. Wilcock, S. T. Kenworthy and J. C. Crowe "Experimental Study of the Transport of Mixed Sand and Gravel" *Water Resources Research*, vol. 37, no. 12, pp. 3349-3358, December 2001.

[75] G. Parker "Surface-Based Bedload Transport Relation for Gravel Rivers" *Journal of Hydraulic Research*, vol. 28, no. 4, pp. 417-436, 1990.

[76] J. G. Duan and S. Scott "Selective Bed Load Transport in Las Vegas Wash, a Gravel-Bed Stream" *Journal of Hydrology*, vol. 342, pp. 320-330, 2007.

[77] H. A. Einstein "The Bed Load Function for Sediment Transportation in Open Channel Flows" *Technical Bulletin of U.S. Department of Agriculture*, 1950.

[78] B. G. Krishnappan "Sediment Transport Regime of St. Clair River" *Report for International Upper Great Lakes Study, International Joint Commission*, 2009.

[79] www.glerl.noaa.gov

[80] S. Attar and S. S. Li "Momentum, Energy and Drag Coefficients for Ice-Covered Rivers" *River Research and Applications*, 2012.

[81] S. M. Hsu and F. M. Holly "Conceptual Bed-Load Transport Model and Verification for Sediment Mixtures" *Journal of Hydraulic Engineering*, vol. 118, pp. 1135-1152, 1992.